

ION MOBILITY SPECTROMETRY: OPTIMIZATION OF PARAMETERS IN  
COLLISION CROSS SECTIONS AND TRACE DETECTION OF EXPLOSIVES

A Thesis

Submitted to the Faculty

of

Purdue University

by

Tianyang Wu

In Partial Fulfillment of the

Requirements for the Degree

of

Master of Science in Mechanical Engineering

December 2018

Purdue University

Indianapolis, Indiana

**THE PURDUE UNIVERSITY GRADUATE SCHOOL**  
**STATEMENT OF COMMITTEE APPROVAL**

Dr. Carlos Larriba Andaluz, Chair

Department of Mechanical Engineering

Dr. Andres Tovar

Department of Mechanical Engineering

Dr. Likun Zhu

Department of Mechanical Engineering

**Approved by:**

Dr. Sohel Anwar

Chair of the Graduate Program

To my Father, my Mother, and my Motherland.

## ACKNOWLEDGMENTS

At the beginning, I would like to express my sincere gratitude towards my thesis advisor, Dr. Carlos Larriba Andaluz. First of all, for his indispensable tutoring about the knowledge related to not only this topic but also other scientific problem, from which I have learnt a great deal, become a student can conduct scientific research from an ignorant young fellow. Secondly, for his great patience to a student who have no outcomes for a long time and have not abandoned me. Moreover, for his friendliness, which bring all his students a colorful life. Then, I really appreciate all the colleagues I have worked with in the lab. I feel extraordinarily grateful for MD Minal Nahin, for showing me his life experience as an elder student, which make me relax every time when I feel depressed. I really want to show my gratitude to Vaibhav R. Shrivastav too, for his patient teaching in the experiment and the knowledge about the apparatus. Great thanks to Joseph Michael Derrick as well, for his unselfish help in not only the devices maintain, coding, and many other stuff. Thank Tim Poe for his assistance for the experiment as well as his design of the new charging chamber. Finally I want to thank Xi Chen, for his help in many aspects, especially for his experience of writing papers. And last but not least, I am really lucky to have a good personal relationship with all the colleagues I mentioned, and many other good fellows. I really appreciate that.

## TABLE OF CONTENTS

	Page
LIST OF FIGURES . . . . .	vii
SYMBOLS . . . . .	xi
ABBREVIATIONS . . . . .	xii
NOMENCLATURE . . . . .	xiii
ABSTRACT . . . . .	xiv
1. INTRODUCTION . . . . .	1
1.1 Ion Mobility Spectrometry . . . . .	1
1.2 Different IMS Apparatus . . . . .	2
1.3 Mass Spectrometry . . . . .	2
1.4 Collision Cross Section . . . . .	4
1.4.1 Different Methods in the Determination of CCS . . . . .	4
1.5 Detection of Explosives . . . . .	10
2. FUNDAMENTAL THEORY . . . . .	12
2.1 The CCS Calculation . . . . .	12
2.2 Modification of the Determination of CCS . . . . .	14
2.3 Simulation With Orientational Effects . . . . .	17
2.4 Using DMA-MS System to Detect TNT . . . . .	22
3. EXPERIMENTAL PREPARATION OF THE DMA-MS . . . . .	23
3.1 DMA-MS System . . . . .	23
3.1.1 Differential Mobility Analyzer . . . . .	23
3.1.2 Quadrupole . . . . .	26
3.1.3 Time of Flight . . . . .	28
3.1.4 Nebulizer . . . . .	29
3.2 TNT Detection of Vaporized TNT Solution . . . . .	29
3.3 TNT Detection from Enclosed Environment . . . . .	34
4. NUMERICAL PROCESS OF THE OPTIMIZATION . . . . .	39
5. RESULTS OF THE OPTIMIZATION . . . . .	44
5.1 The Optimization Using the First Group of Chemicals . . . . .	44
5.1.1 Optimization Starting With Carbon . . . . .	44
5.1.2 Optimization Starting With Hydrogen . . . . .	61
5.2 Variable Velocity Simulation . . . . .	68

	Page
5.3 Discussion . . . . .	70
6. RESULTS OF THE TNT DETECTION . . . . .	73
6.1 Selection of Concentration of Charging Solution . . . . .	73
6.2 TNT in Vaporized Solution . . . . .	73
6.3 TNT from Enclosed Environment . . . . .	82
7. FUTURE WORK . . . . .	105
7.1 For Optimization . . . . .	105
7.1.1 Use Various Buffer Gas . . . . .	105
7.1.2 Further Optimization Using CCS of Amino Acids . . . . .	106
7.2 For TNT Detection . . . . .	108
7.2.1 More Efficient Way to Charge Particle . . . . .	108
7.2.2 More Accurate Temperature Control . . . . .	110
7.2.3 Universal Filter . . . . .	110
7.2.4 Cleaning of Explosives . . . . .	110
8. SUMMARY . . . . .	111
REFERENCES . . . . .	117

## LIST OF FIGURES

Figure	Page
1.1 Depiction of the Projected Area Method . . . . .	5
1.2 The condition considering the collision be elastic, suitable when using mono-atomic molecule as buffer gas like helium . . . . .	7
1.3 Left: A particle with complicated structure; Middle: multiple times of collisions happen before the re-emission; Right: larger gas molecule will deform the structure of target ion . . . . .	9
1.4 Left: specular re-emission; Right: diffused re-emission . . . . .	9
2.1 Optimization results for certain molecules, those molecules are highly asymmetric and the error is not acceptable . . . . .	18
2.2 Selected molecules from the 16 optimized chemical compounds: (a) Choline, (b) Dexamethasone, (c) TMA, (d) C60 . . . . .	19
2.3 Molecules have a large error in CCS: (a) 4-ethylaniline, (b) 4-propylaniline, (c) 4-butyraniline and (d) 4-pentyraniline, while all of the molecules possess a planar structure . . . . .	21
2.4 Simulation of the movement of the molecule in the neutral gas considering the rotational motion, the left show the whole process, the right show each single collision . . . . .	22
3.1 DMA-MS system used in the experiment . . . . .	24
3.2 Conceptual Sketch of DMA-MS system . . . . .	25
3.3 Mechanism of Differential Mobility Analyzer . . . . .	27
3.4 Quadroples Used in the DMA-MS System . . . . .	28
3.5 Image of the heated nebulizer . . . . .	30
3.6 The high voltage will ionize the aromatic molecule directly which can not take charge using acidic solution . . . . .	31
3.7 Detection of TNT from vaporized solutino . . . . .	33
3.8 Ionization of TNT . . . . .	33
3.9 Detection of TNT from enclosed environment . . . . .	35

Figure	Page
3.10 Sensitivity of the Test of different concentration of TNT . . . . .	36
3.11 Absorb and Release TNT molecules . . . . .	37
3.12 Solubility of TNT in different solvent . . . . .	38
3.13 Collection Chamber used in the experiment, wrapped with aluminum foil .	38
4.1 Numerical Process of the Optimization of Parameters . . . . .	39
4.2 A wide surface mapping of $F$ for the Carbon atom extended in the region of interest. . . . .	40
5.1 The mapped optimization surface of carbon in the first iteration. It can be easily figured out that the minimum is a curve instead of a single point	45
5.2 Possible mechanism of the global minimum line: two different routine of the reemission might generate the identical effect . . . . .	46
5.3 Mapped Surface of Hydrogen of the first iteration . . . . .	50
5.4 Mapped Surface of Oxygen of the first iteration . . . . .	51
5.5 Mapped Surface of Nitrogen of the first iteration . . . . .	52
5.6 Mapped Surface of Fluorine of the first iteration . . . . .	53
5.7 Mapped Surface of Carbon of the second iteration in the interest region . .	54
5.8 Mapped Surface of Carbon of the first iteration in the interest region . . .	55
5.9 Mapped Surface of Hydrogen of the second iteration in the interest region	56
5.10 Mapped Surface of Hydrogen of the first iteration in the interest region . .	57
5.11 Mapped Surface of Oxygen of the second iteration in the interest region . .	58
5.12 Mapped Surface of Nitrogen of the second iteration in the interest region .	59
5.13 Mapped Surface of Fluorine of the second iteration in the interest region .	60
5.14 Mapped Surface of Carbon of the third iteration in the interest region . . .	62
5.15 Mapped Surface of Hydrogen of the third iteration in the interest region .	63
5.16 Mapped Surface of Carbon of the third iteration in the interest region (Starting with Hydrogen) . . . . .	64
5.17 Mapped Surface of Hydrogen of the third iteration in the interest region (Starting with Hydrogen) . . . . .	65
5.18 Results comparison between two routine, Opt1 is the routine starting with carbon . . . . .	66

Figure	Page
5.19 The comparison of the result after the primary optimization . . . . .	67
5.20 The structure of the molecule selected for the simulation: triphenylene, it can be easily noticed that the rotation of the molecule will have a great influence on the dipole moment . . . . .	68
5.21 Velocity for the molecule corresponding to time, no preferred orientation .	69
5.22 Rotating angle for the molecule corresponding to time, without preferred orientation . . . . .	69
5.23 To generate single preferred orientation, a fake dipole moment was added to the triphenylene (red arrow) . . . . .	70
5.24 Velocity for the molecule corresponding to time, with preferred orientation	71
5.25 Rotating angle for the molecule corresponding to time, with preferred orientation . . . . .	71
6.1 Spectrum of TNT using 30 mM ammonium acetate . . . . .	74
6.2 Spectrum of TNT using 23 mM ammonium acetate . . . . .	75
6.3 Spectrum of TNT using 15 mM ammonium acetate . . . . .	76
6.4 Spectrum of TNT using 8 mM ammonium acetate . . . . .	77
6.5 Spectrum of TNT using 64 $\mu\text{g}/\text{ml}$ of TNT . . . . .	78
6.6 Spectrum of TNT using 48 $\mu\text{g}/\text{ml}$ of TNT . . . . .	79
6.7 Spectrum of TNT using 32 $\mu\text{g}/\text{ml}$ of TNT . . . . .	80
6.8 Spectrum of TNT using 16 $\mu\text{g}/\text{ml}$ of TNT . . . . .	81
6.9 Spectrum of TNT using 160 ng/ml of TNT . . . . .	82
6.10 Spectrum of TNT using 400 pg/ml of TNT at 120 C . . . . .	83
6.11 Spectrum of TNT using 20 pg/ml of TNT at 120 C . . . . .	84
6.12 Spectrum of TNT using 1 pg/ml of TNT at 120 C . . . . .	85
6.13 Spectrum of TNT using 40 fg/ml of TNT at 120 C . . . . .	86
6.14 Spectrum of TNT using 2 fg/ml of TNT at 120 C . . . . .	87
6.15 Spectrum of TNT using 100 ag/ml of TNT at 120 C . . . . .	88
6.16 Spectrum of TNT using 400 pg/ml of TNT at 150 C . . . . .	89
6.17 Spectrum of TNT using 20 pg/ml of TNT at 150 C . . . . .	90
6.18 Spectrum of TNT using 1 pg/ml of TNT at 150 C . . . . .	91

Figure	Page
6.19 Spectrum of TNT using 40 fg/ml of TNT at 150 C . . . . .	92
6.20 Spectrum of TNT using 2 fg/ml of TNT at 150 C . . . . .	93
6.21 Spectrum of TNT using 100 ag/ml of TNT at 150 C . . . . .	94
6.22 Spectrum of TNT using 400 pg/ml of TNT at 180 C . . . . .	95
6.23 Spectrum of TNT using 20 pg/ml of TNT at 180 C . . . . .	96
6.24 Spectrum of TNT using 1 pg/ml of TNT at 180 C . . . . .	97
6.25 Spectrum of TNT using 40 fg/ml of TNT at 180 C . . . . .	98
6.26 Spectrum of TNT using 2 fg/ml of TNT at 180 C . . . . .	99
6.27 Spectrum of TNT using 100 ag/ml of TNT at 180 C . . . . .	100
6.28 Total counts for selected peaks for different temperature . . . . .	100
6.29 Log (concentration) - count relation at 120 C . . . . .	101
6.30 Log (concentration) - count relation at 150 C . . . . .	102
6.31 Log (concentration) - count relation at 180 C . . . . .	103
6.32 Sensitivity achieved in the tests . . . . .	104
7.1 Leucine and isoleucine . . . . .	105
7.2 Several 3D images of the DFT structure of amino acid molecules . . . . .	107
7.3 Different Perspectives of New Chamber . . . . .	108
7.4 Mechanism of New Chamber . . . . .	109

## SYMBOLS

$m_{ion}$	molecular mass of the ion
$m_{gas}$	mass of the gas molecule
$z$	number of charge
$e$	unit charge
$T$	effective temperature
$\Omega_{avg}^{1,1}$	orientationally averaged collision integral
$K$	ion mobility
$k_b$	Boltzmann constant
$N$	gas number density
$\phi$	first orientation angle
$\theta$	second orientation angle
$\gamma$	third orientation angle
$F$	optimization equation
$\nabla F$	gradient of the optimization equation

## ABBREVIATIONS

CCS	Collision Cross Section
DMA	Differential Mobility Analyzer
DFT	Density Functional Theory
MS	Mass Spectrometry
IMS	Ion Mobility Spectrometry
TOF	Time of Flight
PA	Projected Area
EHSS	Elastic Hard Sphere Scattering
DHSS	Diffuse Hard Sphere Scattering
L-J	Lennard-Jones

## NOMENCLATURE

Alanine	2-Aminopropanoic acid
Arginine	2-Amino-5-guanidinopentanoic acid
Asparagine	2-Amino-3-carbamoylpropanoic acid
Aspartic acid	2-Aminobutanedioic acid
Cysteine	2-Amino-3-sulfhydrylpropanoic acid
Glutamic acid	2-Aminopentanedioic acid
Glutamine	2-Amino-4-carbamoylbutanoic acid
Glycine	2-Aminoethanoic acid
Histidine	2-Amino-3-(1H-imidazol-4-yl)propanoic acid
Isoleucine	(2S,3S)-2-amino-3-methylpentanoic acid
Leucine	2-Amino-4-methylpentanoic acid
Lysine	(2S)-2,6-Diaminohexanoic acid
Methionine	2-amino-4-(methylthio)butanoic acid
Phenylalanine	(S)-2-Amino-3-phenylpropanoic acid
Proline	Pyrrolidine-2-carboxylic acid
Serine	2-Amino-3-hydroxypropanoic acid
Threonine	2-Amino-3-hydroxybutanoic acid
Tryptophan	2-Amino-3-(1H-indol-3-yl)propanoic acid
Tyrosine	L-2-Amino-3-(4-hydroxyphenyl)propanoic acid
Valine	2-Amino-3-methylbutanoic acid

## ABSTRACT

Wu, Tianyang. M.S.M.E, Purdue University, December 2018. Ion Mobility Spectrometry: Optimization of Parameters in Collision Cross Sections and Trace Detection of Explosives. Major Professor: Carlos Larriba Andaluz.

Ion mobility spectrometry is a powerful technique for the study related to molecule. The work of tow major applications are introduced in this paper. The first application is the optimization of parameters in CCS. The accurate calculation of the collision cross section for multiple molecules is a long-time interested topic in the research for substances detection in micro scale. No reliable analytical approach to calculate the collision cross section has been established to date. Different approaches rely on different mechanism will provide different results in significant extent. This work introduce a method for the determination of parameters in the Lennard Jones potential. Experimental data combined with numerical computation was the fundamental strategy during the optimization of the parameters. In the experiment, electrospray is used as the ion source of IMS while a nebulizer was utilized to electrify the aromatic compounds. New parameters show no less accuracy and equal efficiency while can explain the physical meaning of the collision more clearly. The second application is the trace detection of explosives with very low concentration. The detection of explosives is an important topic in security, while the detection will be difficult due to the low vapor pressure of explosives. In this work, two types of devices are designed for the trace detection of explosives at an extremely low concentration. TNT is selected as the explosives in the experiment. The experiment succeed to reach a sensitivity of 1 part per quintillion, and even find out a linear relationship between the logarithm of TNT concentration and TNT vapor pressure.

## 1. INTRODUCTION

### 1.1 Ion Mobility Spectrometry

Ion mobility spectrometry (IMS) is an analytic technique to separate different molecular ions in gaseous phase depending on their different mobility under an electric field with neutral buffer gas. It was first developed primarily by Earl W. McDaniel of Georgia Institute of Technology in the 1950s and 1960s [1]. The IMS instrument has many advantages for substance detection, such as its high sensitivity. Besides, unlike the mass spectrometry, IMS instrument can be operated under an atmospheric pressure. Although IMS can run alone, researchers prefer to couple IMS with other analytic apparatus, such as mass spectrometry [2–7], gas chromatography [8–11] or high performance liquid chromatography [12–16] in order to achieve a multi-dimensional separation. Since the IMS is separating groups of particles based on their capability of motion under electrified environment with buffer gas, which is influenced by the microscopic properties of the target particles, the IMS experimental analysis can be appropriately utilized in the researches of the ion structure. The behaviors of substances in the microscopic world will be totally different compared to the macroscopic ones, and researchers do not have sufficiently reliable elucidation about the molecular behaviors to date. IMS analysis can provide the experimental reference for the theoretical study of molecules and ions.

Although the IMS is very powerful in the research, some shortcomings need to be overcome. IMS can only work for the charged particles, while many important substances to be analyzed are neutral. To solve this problem, researchers often add acids or ammonium salts to charge the target particles. Nevertheless, there still various substances are extremely hard to be ionized. For example, due to the stability of the structure, aromatic compounds are nearly impossible to be ionized by acidic

solution. This paper will explain one possible way to ionize aromatic compounds efficaciously.

## 1.2 Different IMS Apparatus

Depending on identical mechanism, various types of IMS instruments have been developed in the past decades. IMS instruments can be roughly subcategorized into two classes. [17] The first class of IMS provide a complete spectra in a single separation. This class includes dispersive drift tube ion mobility spectrometry (dispersive DTIMS), travel wave ion mobility spectrometry (TWIMS), and trapped ion mobility spectrometry (TIMS). The second class of IMS can both separate ions within selected mobility range and acquire the complete spectra. This class includes selective DTIMS, field asymmetric waveform ion mobility spectrometry (FAIMS), overtone mobility spectrometry (OMS), circular ion mobility spectrometry, transversal modulation ion mobility spectrometry (TMIMS) and Differential mobility analysis ion mobility spectrometry (DMA-IMS). Research showed here will use the technique of DMA-IMS.

## 1.3 Mass Spectrometry

Mass spectrometry (MS) is an analytic technique to sort the ions depending on their mass-to-charge rate. The MS test will generate the mass spectrum, which is the plot of ion signal as a function of mass-to-charge ratio. These spectra are often utilized to recognize the elemental or isotopic signature of the sample, and illustrate the chemical structure of various particles. An MS system will contain three major parts [18]:

- Ion Source
- Analyzer
- Detector System

The ion source provide the gaseous ions from the studied substances. Two frequent used techniques currently are electrospray ionization (ESI), invented by John Fenn [19], and the matrix-assisted laser desorption/ionization (MALDI), developed by K. Tanaka, M. Karas and F. Hillenkamp, et. al [20,21]. Based on the residual energy applied, ion source can be categorized as hard ionization and soft ionization. Hard ionization techniques will impart high quantities of residual energy in the subject molecule, providing large degrees of fragmentation. The representative is electron ionization (EI). Both ESI and MALDI are soft ionization. This technique impart little residual energy, and result in little fragmentation. Other examples of soft ionization include fast atom bombardment (FAB) [22], chemical ionization (CI) [23], and atmospheric-pressure chemical ionization (APCI) [24]. Other ionization techniques include secondary ion mass spectrometry (SIMS), spark ionization and thermal ionization (TIMS) [25]. Different ionization techniques are suitable for different situations.

The analyzer is the key part of MS instrument. It functions the selection of different groups of ions based on their mass-to-charge ratio. The governing factors are the electric and magnetic fields in vacuum inside the MS system. There are many types of mass spectrometer, and many of them will use two or more analyzers for tandem mass spectrometry (MS/MS). Typical types of analyzers include Sector mass spectrometer [26], Time-of-Flight (TOF) [27], quadrupole mass analyzer [28], three-dimensional quadrupole ion trap [29], cylindrical ion trap [30], linear quadrupole ion trap [31], orbitrap [32] and Fourier transform mass spectrometry [33].

The detector is the last part of the MS system. Whenever an ion hit the surface of the detector, the detector will record the current produced by the collision. The magnitude of the signal generated and at what mass-to-charge ratio the signal happens will form the mass spectra. In order to amplify the signal, typically some types of electron multipliers will be utilized in the detector. In modern research, the micro-channel plate (MCP) is the most commonly used detector. [34]

## 1.4 Collision Cross Section

One of the most typical derivative researches depended on the analysis of ion mobility is the collision cross section (CCS). For a straightforward understanding, collision cross section can be acknowledged roughly as "the size of molecule", the shallowest understanding of it can be "how big area the considered molecule will influence when the collisions with other molecules happen", which is also significantly influenced by the geometrical properties of the molecules. With the gradually comprehensive understanding of collision cross section, many properties of the chemical compounds can be learned. Since the complicated process of the molecular collision is not yet fully known, hypothesis needs to be made during the calculation. Different approaches based on altering hypotheses to simulating the process of molecular collision will trigger to entirely different results of CCS. Here some methods are introduced.

### 1.4.1 Different Methods in the Determination of CCS

#### The Projected Area Method

The projected area method is the simplest way to determine the collision cross section. After simplification, only the collisions contain two molecules at one moment are under consideration. Both molecules are considered as rigid body and the collision is exactly the contact of the two compact structures. No other factors involved. The value of CCS will only depend on the size and shape as well as the relative velocity of the two classes of molecules. As the molecules will rotate when they are moving, the effect of shape and size can be averaged as the radius of the approximated sphere. The equally possible directions of motion will average the effect of relative velocity. The gas molecules have a smaller size are considered to move randomly, while the detected molecules are assumed keep stationery. Under these assumptions the direct interpretation of the collision cross section will be the area the collision will happen when the gas molecules pass through. As Fig 1.1 shows, two classes of molecules

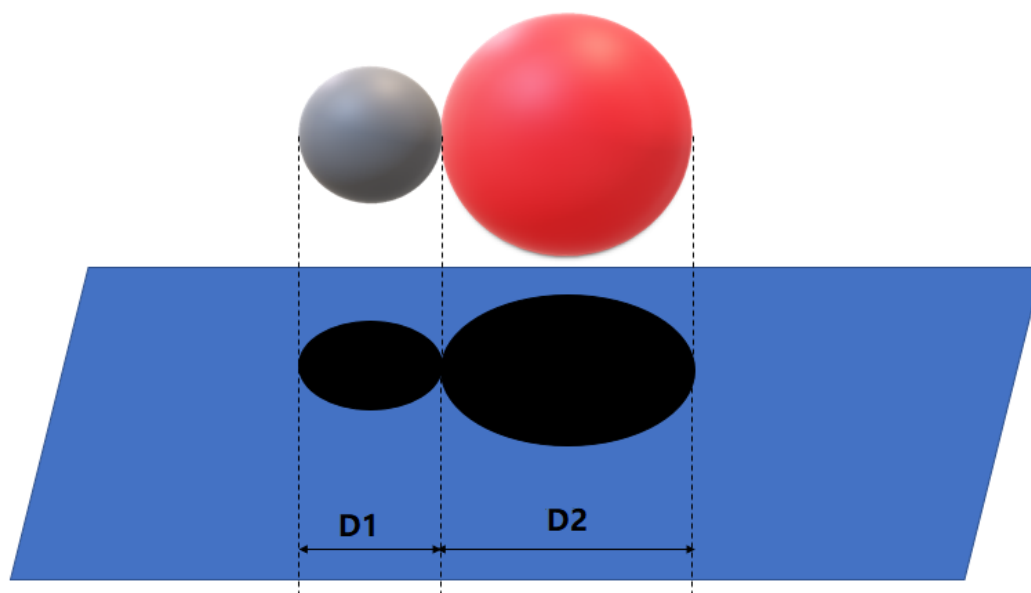


Figure 1.1. Depiction of the Projected Area Method

are approximated as different hard spheres, then project the spheres onto an fictional plane, and the CCS under this circumstance, interpreted into a circular area, will be calculated using the radii (Fig. 1.1):

$$CCS = \pi\left(\frac{D_1}{2} + \frac{D_2}{2}\right)^2$$

$D_1$  and  $D_2$  represent the diameters of the two hypothetical micro-balls. Undoubtedly this idealized method to calculate the CCS can only trigger to a poorly accurate solution, so only under very few conditions this method is suggested to be applied. The projected area method can be conducted only when the following conditions are fulfilled based on the research of Carlos Larriba et al. [35]:

- The surface of the molecular structure should be completely convex in order to avoid multiple scattering effects.
- The translational energy of the atoms should dominate the rotational and vibrational energy.
- Long range potentials are not under consideration.

Notice that since the molecules can have a larger range be affected by the intermolecular forces, when the strategy of ignoring all the influence the molecules can exert is conducted, the acquired CCS values will be certainly smaller than the exact ones. Therefore, the CCS value obtained by the projected area method can be considered as a very weak lower bound for the CCS calculation.

### **Elastic Hard Sphere Scattering Method**

Only considering the geometrical properties of the molecules in the CCS calculation will be completely insufficient while a high accuracy result is needed. Simulating the process involving the intermolecular force, researchers established the method named hard sphere scattering method. This method assumes infinite hard potential wall between the colliding bodies, generating scattering effect. The gas molecules will



re-emit instantly after the collisions happen. No penetration happen during the collision. This method is called hard sphere scattering method. There are two types of hard sphere scattering method are considered: elastic hard sphere scattering (EHSS) and diffused hard sphere scattering (DHSS). The EHSS will consider the process of collision is specular and elastic [36]. The momentum of the two bodies exchange, and the reflection angle will be the same as the incident angle. This model will work well when using monoatomic gas molecule like the helium or argon as the buffer gas [37]. (Shows in Fig. 1.2) When the target has a shape of a simple sphere, the CCS will be the same as PA method. If the target ion has a linear structure, this method will still be workable. Due to its simpleness, this method is widely utilized. However, the hypothesis of specular and elastic is actually not realistic when the polyatomic molecules are utilized in the study.

### **Diffused Hard Sphere Scattering Method**

The second types of hard sphere scattering method is DHSS. The structure of target ions can be much more complicated than a linear body. The figure in the left of Fig. 1.3 shows an example of complicated structure of particles. When gas molecules collide with such types of ions, instead of one time of collision, multiple times of collision can happen (middle of Fig. 1.3). Moreover, when a larger gas molecule is used, the structure of the target ion will be deformed (right of Fig. 1.3). With these consideration, the re-emission of molecules will have a diffusive nature, which means the reflection angle might not be the same as the incident one (right of Fig. 1.4). Moreover, this method shows the inelastic nature of the gas molecule-structure collision. When the polyatomic molecules, such as nitrogen, are utilized as the buffer gas, researchers usually use DHSS instead of EHSS in the CCS calculation.

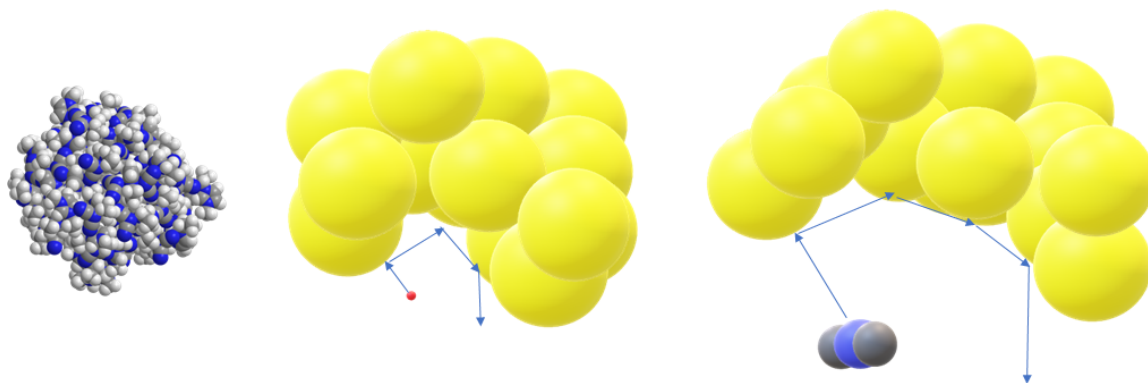


Figure 1.3. Left: A particle with complicated structure; Middle: multiple times of collisions happen before the re-emission; Right: larger gas molecule will deform the structure of target ion

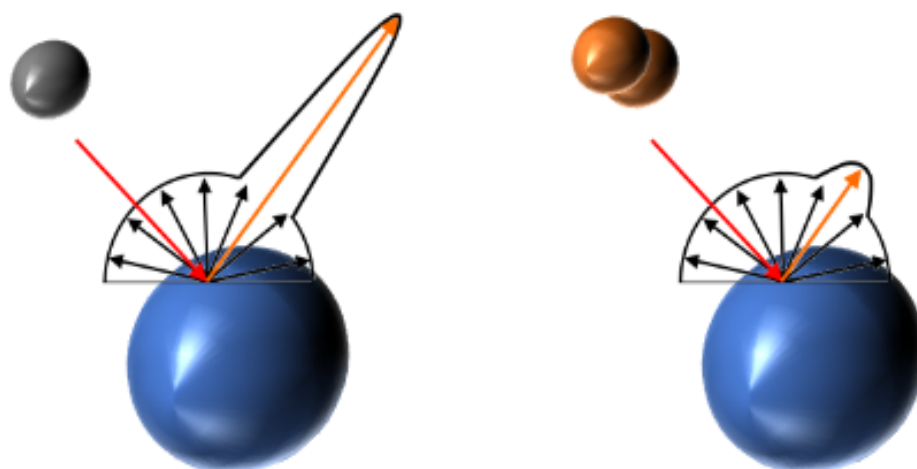


Figure 1.4. Left: specular re-emission; Right: diffused re-emission

## The Trajectory Method

The last method to calculate CCS to be mentioned here is the trajectory method. The trajectory method calculate the CCS by taking well-depth, interception and ion-induced dipole moment into account to obtain the desired deflection angle in the Mason-Schamp approximation. This method will provide a more accurate results compared to the two kinds of hard sphere scattering method when the situation contains complicated surfaces. Moreover, if the molecules detected have heavier weight as well as larger polarizability, this method can be more reliable. Although there are numbers of advantages for the trajectory method, the utilization of this method is not easy. One reason is that the complex form of its mathematical equation will trigger a large computing expense. The second reason is that some parameters of the equation cannot be determined analytically to date, and the empirical results of those parameters will differ significantly using different hypotheses. In this work a novel strategy to determine the parameters with a respectively low computing expense without sacrificing the accuracy is thoroughly discussed.

### 1.5 Detection of Explosives

The effective and accurate detection of various explosives in different environments is continuously an important problem in research. One of the most severe problem is the contamination caused by the residual explosives in the soils. [38] Most common explosives trigger to this problem include Research Department explosive (RDX), high melting point explosive (HMX), trinitrotoluene (TNT) and other nitroaromatic and nitramine explosives. [39] These compounds are toxic, and very persistent in the environment. [40] Even the concentration of those explosives will exist at very low concentration in the environment, there is still a high possibility of causing health problem to human. [41] For instance, one of the most famous explosives, TNT, shows mutagenic properties, causing problems like liver damage or anaemia. [42]

The effective detection and analysis of explosives in the environment is extremely difficult due to the low vapor pressure of the explosives. [43, 44] Simultaneously, the environmental and biological processes exist in the environment will reduce the concentration of the analytes. [41] There are different methods reported for the explosives detection. Most of the methods utilized are spectrometric, [45, 46] or electrochemical. [47–49]. In the detection, techniques of separation, such as gas and liquid chromatography play important role in the study. [50, 51] In this work, with the proven reliable DMA-MS system, the detection of TNT in the environment coupled with technique of concentrating and releasing TNT is exerted. The novel idea might provide a feasible approach to solve the explosive detection problem.

## 2. FUNDAMENTAL THEORY

### 2.1 The CCS Calculation

Calculation of CCS contains a series of semi-empirical equations. The approach to calculate CCS via electrical mobility is widely utilized. The average drift velocity of an ion under an electric field in a neutral buffer gas can indicate the electrical mobility of this chemical compound. The properties will affect the electrical mobility include but not limit to pressure, temperature, mass of molecules, ion geometrical structure and interaction between ions and gas molecules, etc.. The average effective area of interaction between ions and gas molecules will indicate the value targeted, collision cross section,  $\Omega$ , and its calculation will be crucial for the accurate estimation of electrical mobility. The zero-field mobility equation, can only be applied under the circumstance that the electric field is weak compared to gas density, which means the value of E/N is small, is given by the Mason-Schamp approximation [52]:

$$K = \sqrt{\frac{1}{m_{ion}} + \frac{1}{m_{gas}}} \frac{3ze}{N} \sqrt{\frac{\pi}{2k_bT}} \frac{1}{\Omega_{avg}^{1.1}}$$

Where K is the electrical mobility of the ion,  $m_{ion}$  and  $m_{gas}$  represent the molecular mass of ion and the buffer gas, ze means the charge of the ion, T is the effective temperature, and  $\Omega_{avg}^{1.1}$  will be the orientationally averaged collision integral assuming the probability of collisions happen in every direction is identical. A simplified CCS expression can be calculated analytically using a momentum transfer method by taking all the collision geometries, velocities and impact parameters into consideration as the following [36, 53]:

$$\Omega_{avg}^{1.1} = \frac{1}{8\pi^2} \int_0^{2\pi} d\theta \int_0^\pi \sin\phi d\phi \int_0^{2\pi} d\gamma \frac{\pi}{8} \left(\frac{m_{red}}{k_bT}\right)^3 \int_0^\infty g^5 e^{-\frac{m_{red}g^2}{2k_bT}} dg \int_0^\infty 2b(1-\cos\chi) db$$

Where  $\theta$ ,  $\phi$ , and  $\gamma$  mean three orientations of the motion of molecules, g represents relative velocity, b is the impact parameter,  $m_{red}$  is the reduced mass corresponding to

detected ion and gas molecule, and  $\chi$  is the deflection angle after the collision, which is not an analytical value but a function depends on ion-gas interaction potentials, the relative velocity between ion and gas, the impact parameter and the orientation of the ion, it is expressed by [54]:

$$\chi(\theta, \phi, \gamma, g, b) = \pi - 2b \int_{r_m}^{\infty} \frac{dr}{r^2 \sqrt{1 - \frac{b^2}{r^2} - \frac{\phi(r)}{\frac{m_{red} g^2}{2}}}}$$

Here,  $r$  means the distance between ion and gas molecules,  $r_m$  is the closest distance among different calculation approaches, and  $\phi(r)$  is the ion-gas interaction potential. Although the ion-gas interaction potential  $\phi(r)$  is widely used, an efficacious analytical approach is available to date except for very limited cases. Consequently, a numerical method which is supposed to be reliable is needed for the calculation of deflection angle  $\chi$ .

In order to obtain the deflection angle easily, a dominating potential which will govern the equation of motion is selected. A 4-6-12 potential is the most commonly utilized potential in current research in trajectory method algorithms, which can be expressed as the following:

$$\phi(x, y, z) = 4\epsilon \sum_{i=1}^n \left[ \left( \frac{\sigma}{r_i} \right)^{12} - \left( \frac{\sigma}{r_i} \right)^6 \right] - \frac{\alpha}{2} \left( \frac{ze}{n} \right)^2 \left[ \left( \sum_{i=1}^n \frac{x_i}{r_i^8} \right)^2 + \left( \sum_{i=1}^n \frac{y_i}{r_i^8} \right)^2 + \left( \sum_{i=1}^n \frac{z_i}{r_i^8} \right)^2 \right]$$

In this equation,  $r_i = (x_i, y_i, z_i)$  is the distance between gas molecule and the atom in the group of  $n$ ,  $\alpha$  is the polarizability of the buffer gas dominating the ion-induced dipole term, and  $\epsilon$  and  $\sigma$  are the parameters in the Lennard-Jones (L-J), meaning well-depth and intercept (zero potential crossing), respectively. The effect of polarizability toward the deflection angle is well understood. Nevertheless, the Lennard-Jones parameters employed in the equation still exist ambiguity. This pair,  $\epsilon - \sigma$ , will always bring huge error if we employ the results of the pair from other calculation into the 4-6-12 potential. No sophisticated calculation approach can guarantee to provide an accurate L-J parameters pair in the CCS calculation. All the previously presented equations make different extension of simplifications, such as the conservation of energy and momentum in each collision, higher order potential interactions and the

atoms are fixed, etc.. When using helium as the buffer gas, which is small and has a rigid molecule, those effects can be neglected and still generate accurate results. However, if larger neutral molecule buffer gas is used, such nitrogen and carbon dioxide, those simplification will trigger to unacceptable error. [55, 56] Since we observe the difference between the either exact hard sphere scattering (EHSS) or Projection Approximation (PA) and the experimental results, we figure out the simplification must cause problem. Those simplifications are considered as the reason to explain why the number of the L-J parameters in other calculation can be hardly applied in CCS calculation. The ration between experimental data and the theoretical results will be between 1 and 1.3 in the EHSS calculation and a constant around 1.36 in PA calculation. [57, 58]

## 2.2 Modification of the Determination of CCS

The method must be modified when the nitrogen is employ as buffer gas. Among all the proposed numerical modification, two strategies are the most famous. The first one will introduce ion-quadrupole potential interaction combined with the existing L-J parameters optimization, the other one will consider the artificial diffuse hard sphere scattering which can indicate the vibration of the atoms as well as the energy and momentum exchange in the collisions.

The First modification will be the optimization of Lennard-Jones potentials by adding the ion-quadruple potential into the calculation. This method is conducted by adding extra charge to the nitrogen. 0.4825e of negative charge is placed on each nitrogen atom while 0.965e of positive charge is placed on the center of the molecule. The reaction between the positive charge and negative charge will generate the quadruple moment, which is described as [59, 60]:

$$\phi_{IQ}(x, y, z) = \sum_{j=1}^3 \sum_{i=1}^n \frac{q_i q_j e^2}{r_{ij}^3}$$

Where index j denotes the three charges assumed on the nitrogen molecule, be careful number 2 means the positive one located on the center. Index i denotes the charges of

the ion and atoms. Simultaneously, by introducing impact parameter, whose weight is determined very carefully, the orientation of the nitrogen molecules can be taken into consideration. Very accurate results can be computed after the addition of the factors. However, low efficiency will be caused after the addition and the L-J parameters still require modification due to other effects.

The second modification convert to hard sphere diffuse scattering instead of L-J parameters. For large ions, this method works well as the calculated CCS using sphere diffuse scattering are pretty close to the experimental data. When dealing with larger particles, many researchers will consider the diffuse reemission in the calculation. [61, 62] Since the results of diffuse scattering calculation will typically greater than those computed using specular sphere, those outcomes can be treated as the upper bound of CCS. The narrowed down range of CCS is helpful for the optimization. [63, 64]

The results for both modifications make agreement when the tested collisions have a CCS larger than  $2 \text{ nm}^2$ , which might be caused by the artificially modified L-J parameters. [65] Both increasing the well-depth and decreasing intercept of nearby atoms can enlarge their influence to the trajectory of gas molecules. Those effect consist of influences in different directions, and the general consequence will lead to a similar results from calculation using specular sphere although the exact model will be diffuse scattering (when there is only one atom taken into account the diffuse scattering will still perform entirely different from the specular sphere). Calculated CCS with 4 percent of discrepancy compared to the experimental data can be obtained by using the models generated by appropriate DFT calculation. [66–69] Without the concern of losing accuracy, many other factors, such as vibration of atoms, rotational effects, exchange of energy due to non-zero relative velocity effects, ion-quadrupole and higher order interactions, can be taken into consideration in the CCS. What is not so good, it that the efficiency of the computation will be sacrificed. For small organic molecules, this shortcoming will be exceptionally severe.

Now change the strategy, consider the optimization of Lennard-Jones parameters is undertaken after selecting an atom in a molecule. And another problem needed to be figure out, is that whether it will be feasible to run the optimization using molecules with determined elements. In other words, now the attempt is about trying to avoid the participation of trial and error approaches, which will prevent the calculation be generalized. Those experiments mentioned in the previous cannot remove the influence of trials and error approaches. Moreover, for those methods, the ratio between two L-J parameters,  $\epsilon/\sigma$ , will be fixed in every trial, no matter what kind of molecules are optimized. This strategy is not reasoned. And a different approach will be chosen, where the ratio of parameters will change as the optimization processing.

A series of experiments were conducted to obtain experimental CCS for multiple types of compounds, while DFT calculation was also employed in order to determine the initial geometry of the tested compounds. Several rounds of numerical calculation will be conducted during the optimization, which can trigger to dynamic values of the well-depth and intercept for different elements. The goal of the work is to absorb the ion-quadruple into the L-J parameters, increasing the computational accuracy without sacrificing the efficiency. At the beginning of the optimization, molecules with fewer kinds of elements were selected to simplify the computation, as L-J parameters of fewer elements are being calculated in these processes. For each round of optimization, one element was researching in the process, eventually get the final value. After the L-J parameters for the element initiates the optimization have been determined, keep the optimized values of the parameters and then molecules with more various elements will be put into the calculation. The new parameters of all elements will be collected and make a comparison with the traditional values. For carbon, hydrogen, oxygen, nitrogen, fluorine, new values for the L-J parameters were acquired after the optimization, giving the smallest error.

### 2.3 Simulation With Orientational Effects

Although most of the parameters obtained from the optimization can be used in the calculation of CCS and provide numerical results with very small error, problem happens when the calculation comes to some highly asymmetric compounds. All the already employed strategies did not consider about the symmetry. One key point of the optimization is that many effects, such as vibration of atoms, rotational effects, exchange of energy due to non-zero relative velocity effects, ion-quadrupole and higher order interactions can be embedded into the optimized L-J parameters while the accuracy of the results of CCS will still be guaranteed simultaneously. If those effects are not taken into account, the computing expense will be decreased greatly. However, unlike other small molecules, these assumption seems not working when certain structures are taken into the optimization with the identical process.

When observe and compare those structures with the previous molecules carefully, the possible reason for this error is assumed. The previous molecules optimized possess a respectively regular structure. Taking the rotation of the molecules into account, the of collision can be roughly treated as two spherical bodies collide with each other. Under this circumstance, the ion-induce dipole moment of the molecules perform like a constant, which make the calculation of the optimization simpler. When optimizing molecules which will not generate large dipole moment change, this method works well. The calculated CCS using the optimized parameters for most of the molecules run previously will have an error of less than 2 percent.

However, when the parameters obtained from the calculation are employed in other molecules, severe inaccuracy happens. Those molecules CCS have error over 4 percent were particularly interested. Compounds like 4-ethylaniline, 4-propylaniline, 4-butylianiline and 4-pentylianiline will even have error for over 10 percent, which are showed in the table. All of those molecules have a benzene ring, which is a typical planar structure. The two dimensional plane is highly anisotropic, the properties can be entirely different between horizontal and vertical direction. In this case, the most

	<u><math>\Omega</math>-N2</u>	<u>SD</u>	<u>CCS-IMoS-N2</u>	<u>SD</u>	<u>Error</u>	<u>Dipole Moment</u>
Leucine	140.3	0.9	124.7	1.3	-12.6	<b>6.45</b>
Isoleucine	137.2	1.0	123.7	1.1	-10.9	<b>6</b>
N-ethylaniline	131.3	1.5	122.8	0.5	-6.9	<b>4.92</b>
N-propylaniline	136.8	1.5	127.9	1.0	-7.0	<b>2.68</b>
N-butylaniline	141.9	1.0	134.7	1.4	-5.3	<b>2.14</b>
N-pentylaniline	147.1	0.8	140.9	2.3	-4.4	<b>3.78</b>
4-ethylaniline	141.1	0.7	124.0	0.9	-13.8	<b>10.45</b>
4-propylaniline	148.7	0.8	131.0	0.6	-13.6	<b>11.76</b>
4-butylaniline	154.3	1.1	138.1	1.5	-11.7	<b>13.33</b>
4-pentylaniline	164.3	0.7	145.3	1.5	-13.1	<b>16.37</b>

Figure 2.1. Optimization results for certain molecules, those molecules are highly asymmetric and the error is not acceptable

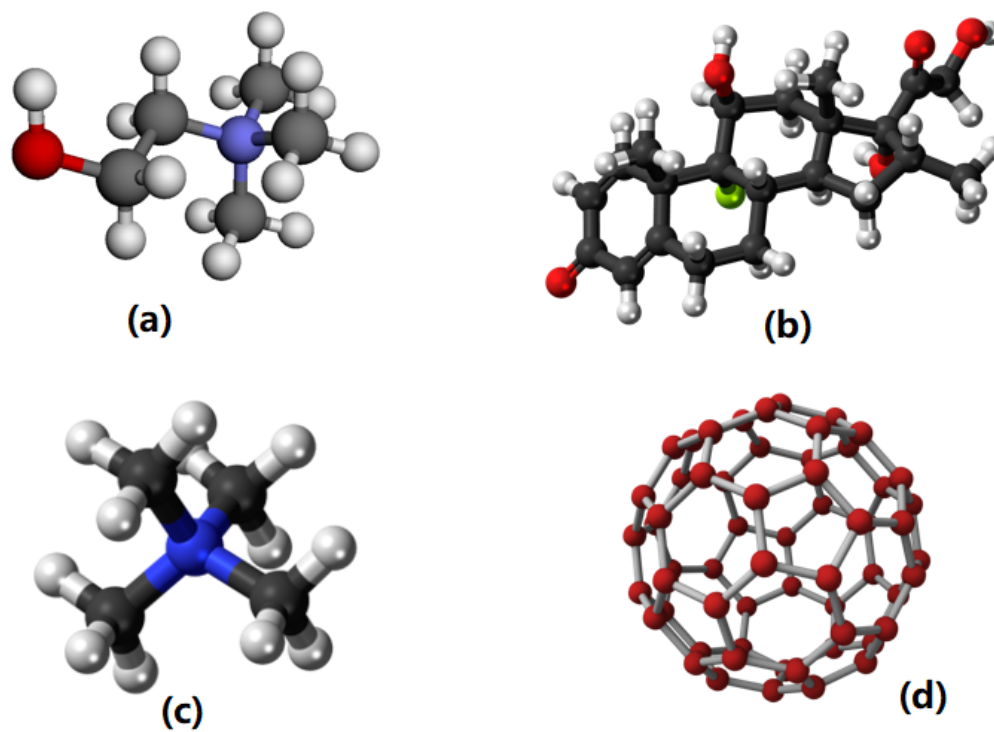


Figure 2.2. Selected molecules from the 16 optimized chemical compounds: (a) Choline, (b) Dexamethasone, (c) TMA, (d) C60

obvious influence will be the dipole. The fundamental assumption in the optimization indicate that the dipole moment of the molecule will remain constant during the whole process. While in the realistic, all the molecules will have rotations continuously, always have different orientation of movement, so the dipole moment will keep on changing. For those structures which are more symmetric, their dipole moments are smaller, thus the change of orientation of motion will not affect the optimized results a lot, since the effects can be more or less averaged. But for a planar structure, the change of direction of dipole moment will be more apparent, which will lead to a greater inaccuracy.

Theoretically speaking, without changing the basic idea, some modifications can be utilized to fix this problem. The most straightforward solution is to divide the optimization into smaller steps, within each step the dipole moment of the molecule will have a certain value. After collecting the values among the whole process, average the data and then the final results will be acquired. This strategy can solve the problem simply, but every trial running the sample will contain billions of collisions and can be divided into an even larger amount of steps. The computing expense will be unbelievable, therefore this strategy is not feasible. Obviously, the trajectory method will no longer be appropriate in this case.

Now use another way to think about the problem. In the previous study the drift velocity of the molecules incident to the buffer gas is consider to be the same as the velocity of the gas flow, and the gas molecules are assumed to have a velocity parallel to the DMA plate. The exact situation is totally another way, each gas molecule will have their only velocity, while the speed in the three components should be completely random. Therefore it is nearly impossible to calculate the real drift velocity of the tested molecules analytically. Therefore, the way to determine the drift velocity using numerical simulation was selected. Based on the measurable properties such as the temperature, gas molecules with random velocities were generated depending on Maxwell-Boltzmann distribution in a controlled volume. Then, the tested compounds, showing their 3-D structure were introduced to the volume. The 3-D model of the

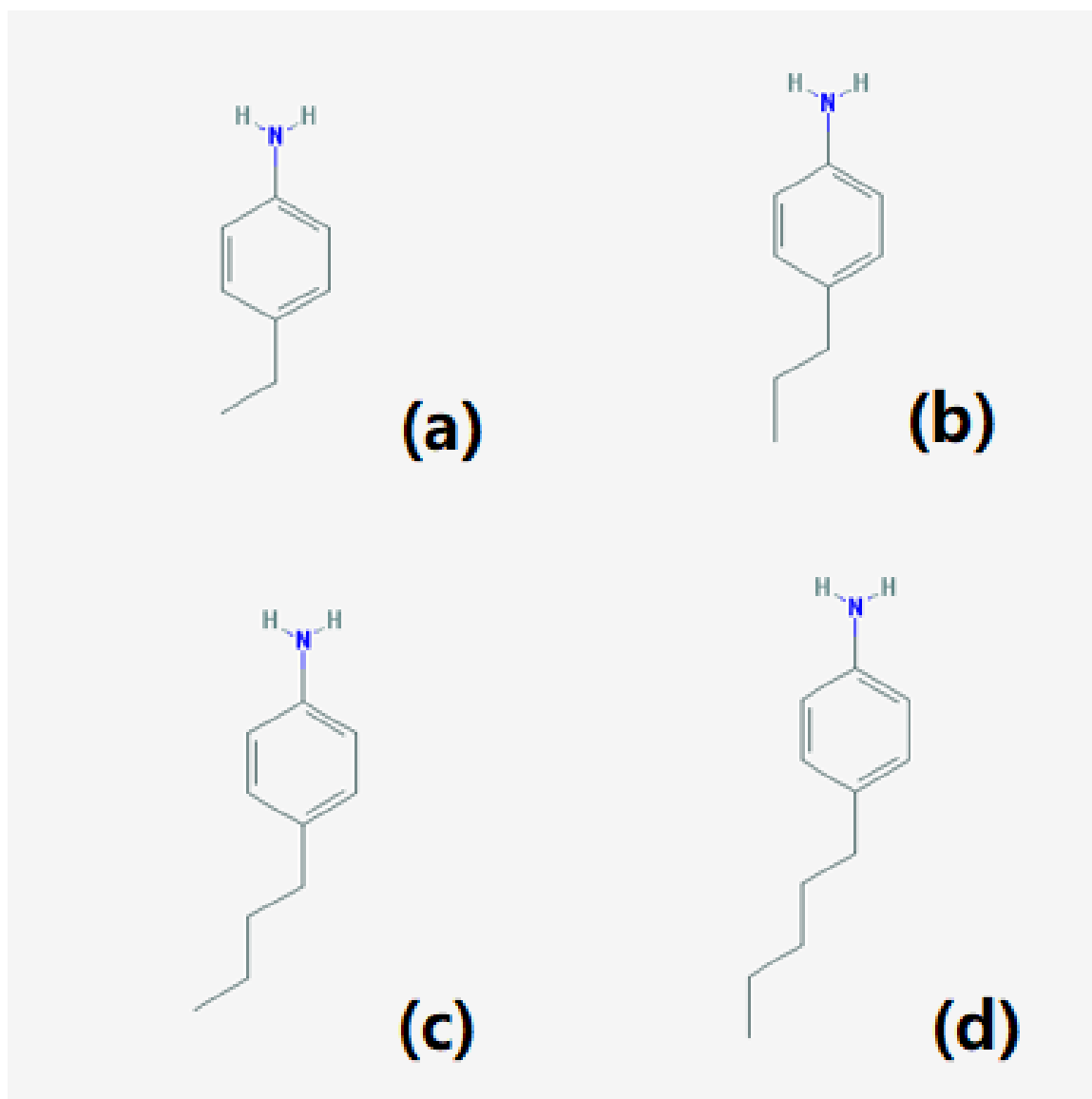


Figure 2.3. Molecules have a large error in CCS: (a) 4-ethylaniline, (b) 4-propylaniline, (c) 4-butylaniline and (d) 4-pentylaniline, while all of the molecules possess a planar structure

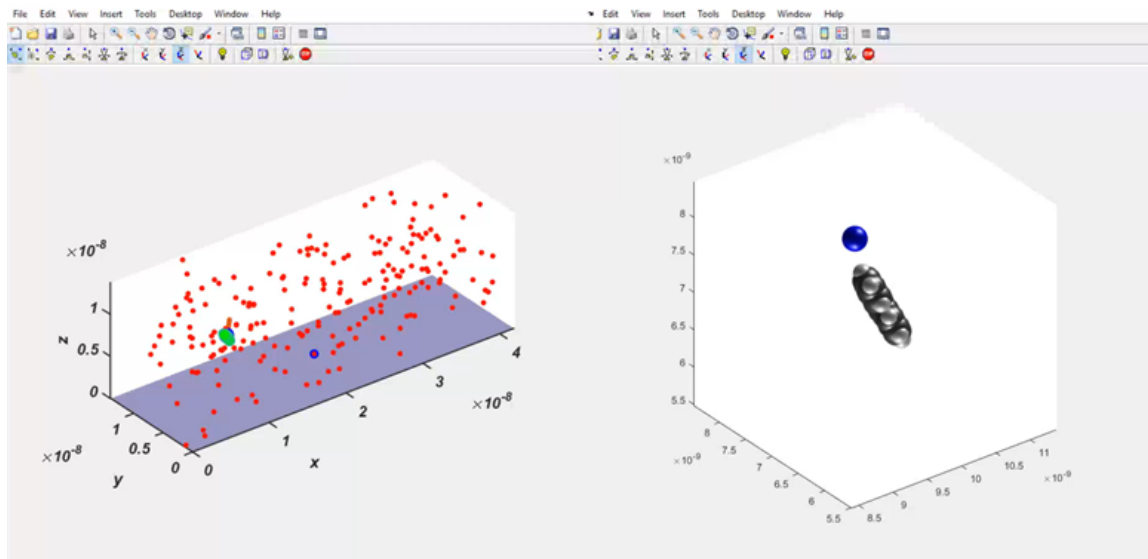


Figure 2.4. Simulation of the movement of the molecule in the neutral gas considering the rotational motion, the left show the whole process, the right show each single collision

molecules can perform the rotational motion while they are moving, when can be interpreted into the dipole moment change in the collision.

With a long period of simulation, the movement of the molecule become stable gradually, the numerical result for their drift velocity can be collected.

## 2.4 Using DMA-MS System to Detect TNT

The key problem of the TNT detection using the DMA-MS system is the confirmation of the particles related to TNT. Previous studies showed TNT will transform to various particles when it is tested in MS system. The major peaks of TNT in its mass spectrum include 198, 211 and 227. [70] However, other types of particles can also be generated in the test, even become the peaks with strongest intensity. [71] Therefore, when the experiment of TNT detection is perform, the performance of the TNT molecules in the apparatus utilized should be analyzed first.

### 3. EXPERIMENTAL PREPARATION OF THE DMA-MS

#### 3.1 DMA-MS System

The DMA-MS system can be divided as three parts: ion source, DMA and MS. The method of electrospray is selected in this experiment to generate the studied ion. Solution in a vial is transferred into the DMA by a well-sharpen silicon capillary. At the tip of the capillary, by adjusting the gas pressure and voltage applied to the solution, a Taylor cone is supposed to be formed. There are two way to determine whether a stable Taylor cone is formed. The first way is to observe the Taylor cone directly using camera. Another way is to observe the current of within the solution. When a stable current is achieved, a stable cone is achieved. DMA system is attached to the MS system, connected with a blower to generate the buffer gas flow in the electric field. A mechanical pump is utilized to generate the vacuum needed within the MS system.

##### 3.1.1 Differential Mobility Analyzer

A parallel plate differential mobility analyzer (DMA) is utilized in the experiment, which help to select the ions based on their mobility under electric field and buffer gas. The DMA have a chamber with sheath flow perpendicular to the parallel plates. These two plates are given different potential, therefore a uniform electric field will be generated between the two plates. The sheath flow is generated by a blower and its mass flow rate can be changed by changing the spinning speed of the blower. A slit located in the front plate of the DMA acts as the entrance for the target ions moving toward the MS system. There is another slit on the back plate of DMA as the outlet of particles. The lateral distance between the slits is  $L$ . The distance between the

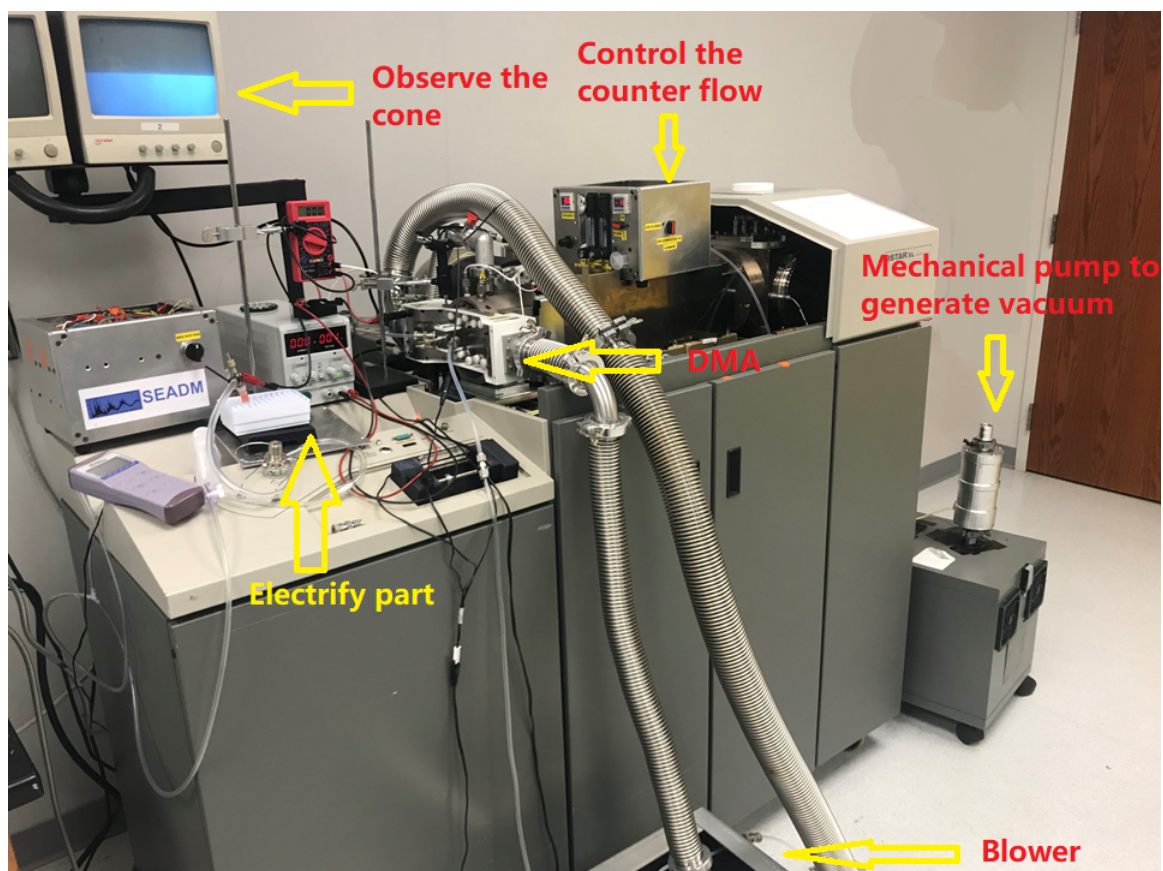


Figure 3.1. DMA-MS system used in the experiment

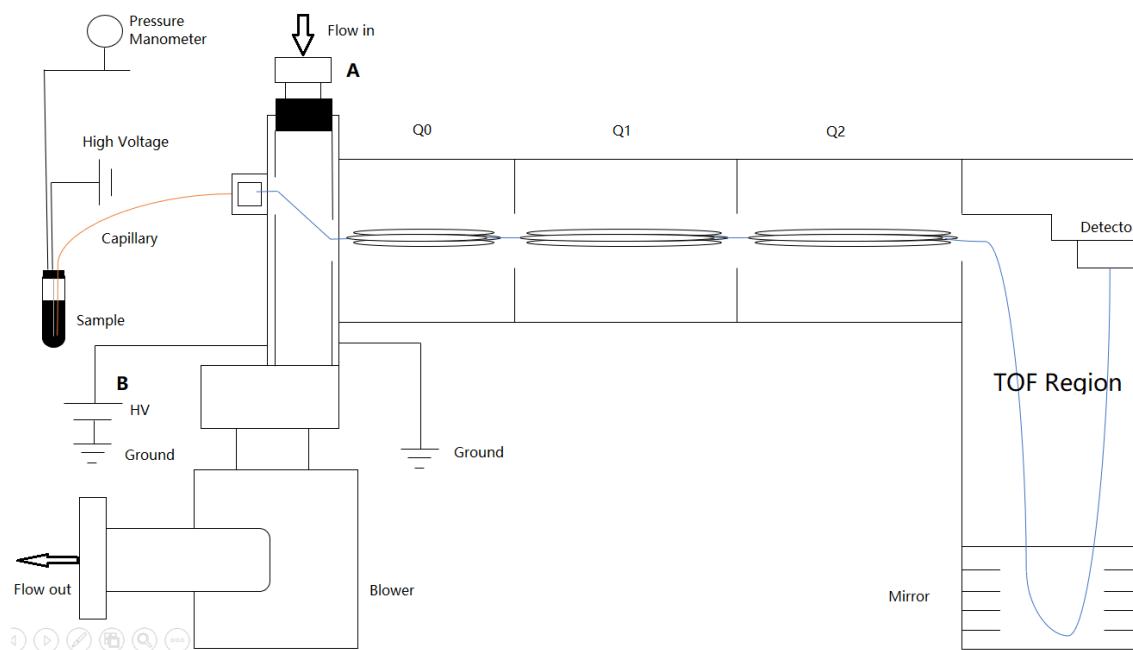


Figure 3.2. Conceptual Sketch of DMA-MS system

two parallel plates is  $\delta$ . (Shown in Fig 3.3) The mobility acquired by DMA can be calculated as the following:

$$T_H = \frac{L}{U}$$

$$T_V = \frac{\delta}{V_{drift}} = \frac{\delta}{ZE}$$

Here  $T_H$  is the time particle will travel in the horizontal direction,  $T_V$  is the time particle will travel in the vertical direction.  $U$  is the velocity of the particle in the horizontal direction. The electric field,  $E$ , will be  $\frac{V_{DMA}}{\delta}$ . If the particle can arrive the outlet successfully these two time must be identical. After calculation, the mobility,  $Z$ , can be obtained:

$$Z = \frac{U\delta^2}{LV_{DMA}}$$

In the general mode,  $V_{DMA}$  is changing, so a mobility spectrum can be generated according to  $V_{DMA}$  and signal intensity. Sometimes when a substance with known mobility, which means certain  $V_{DMA}$ , is studied, the potential can be set constant.

However, the horizontal velocity,  $U$ , is usually very hard to determine. To solve this problem, a reference solution whose mobility is confirmed is utilized. Here the tetraheptylammonium bromide (THABr) is selected as the reference solution. After running the test of the studied substance, the solution is replaced by THABr immediately and run the test again. In this way the mobility can be calculated as:

$$\frac{U\delta^2}{L} = ZV_{DMA} = Z_{THABr}V_{THABr}$$

$$Z = \frac{Z_{THABr}V_{THABr}}{V_{DMA}}$$

### 3.1.2 Quadrupole

This device consists of two pairs of parallel metal rod, functioning separate the ions according to the mass-to-charge ratio. The rods are applied oscillating potentials and each pair will have the same charge. The polarity keep oscillating, therefore the ions within the quadrupole will be selected since ions with different  $m/z$  ratio perform

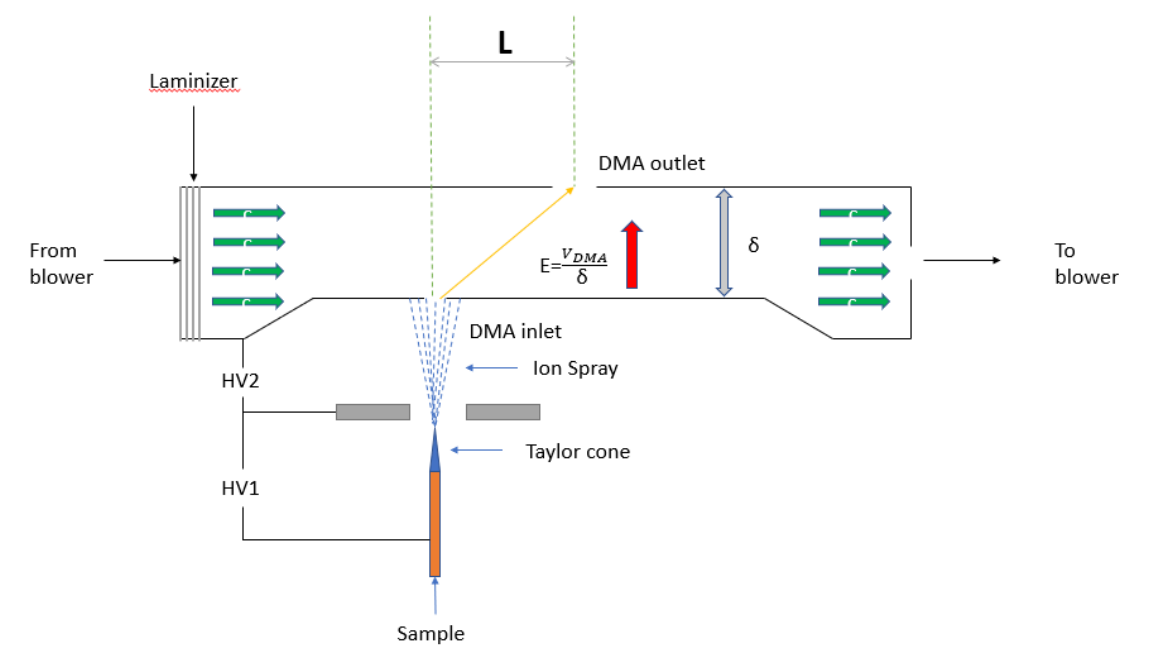


Figure 3.3. Mechanism of Differential Mobility Analyzer

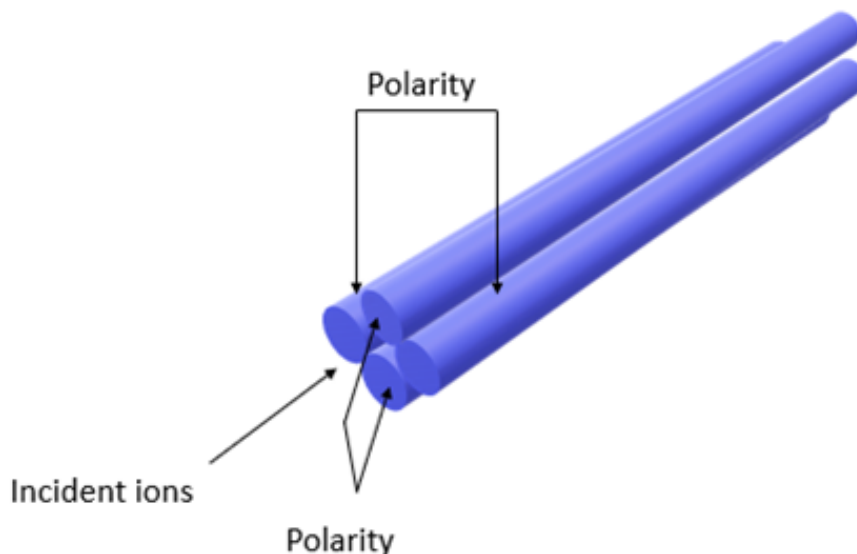


Figure 3.4. Quadrupoles Used in the DMA-MS System

different trajectories. Different windows can be set, only ions with  $m/z$  within certain range can pass through the quadrupole during certain window. The ions targeted can also be centered, leading to a stronger detected signal. For the transmission efficiency purpose, three quadrupole is applied in this DMA-MS system. The second quadrupole functions the further fragmentation of ions while the third quadrupole functions the selection.

### 3.1.3 Time of Flight

When the ions enter the time of flight region of the MS system, an electric field is added to accelerate the ions to the same kinetic energy. Here, the actual velocity of ions will depend on their mass-to-charge ratio. Hence, the time ions take to arrive

at the detector will differ. The separation of ions will be achieved, and the ratio will be calculated based on the travelling time.

#### **3.1.4 Nebulizer**

In the test of electrified materials, aromatic compounds have been a long time existing problem for the difficulty to ionize the molecules. The molecules of the aromatics compounds are extraordinarily stable which make it extremely difficult to ionize it using solution like acetic acid. Without charged solution no electrospray can be achieved, and the mass spectrometry will lack of ion source. To solve this problem, a unique approach was applied which contain a nebulizer (Fig.3.5) heating and electrifying the liquid spray directly. 8 types of aromatic components were tested in the experiment and highly reliable results were collected. By adjusting the heated temperature (200 300 C) and applied high voltage (4000 5000 V), a electrified spray of aromatic molecules in a wide range was generated and running stably.(Fig. 3.6) Since the consumption of solution of the solution will be much larger than use capillary to form a Taylor cone, a bottle of volume of 120 ml will be utilized. One thing need to be careful is that when using the nebulizer, the incident solution will contact the outer surface of the DMA plate. Because of its high consumption of the solution, vital amount of liquids will attach the plate. Therefore, after each trial finished, it is highly recommended to clean the surface of the plate.

### **3.2 TNT Detection of Vaporized TNT Solution**

TNT solution with high concentration is tested first in order to determine the ion mobility of TNT and its performance in the mass spectrum. Notice that the TNT solution must be charged before running the test. A negative mode of the DMA is utilized in the TNT test, and ammonium acetate is selected as the ionization substance to the TNT. To assure the TNT solution can form a cone, high solution of ammonium acetate is applied, in this experiment will be 75 mM. After the mobility

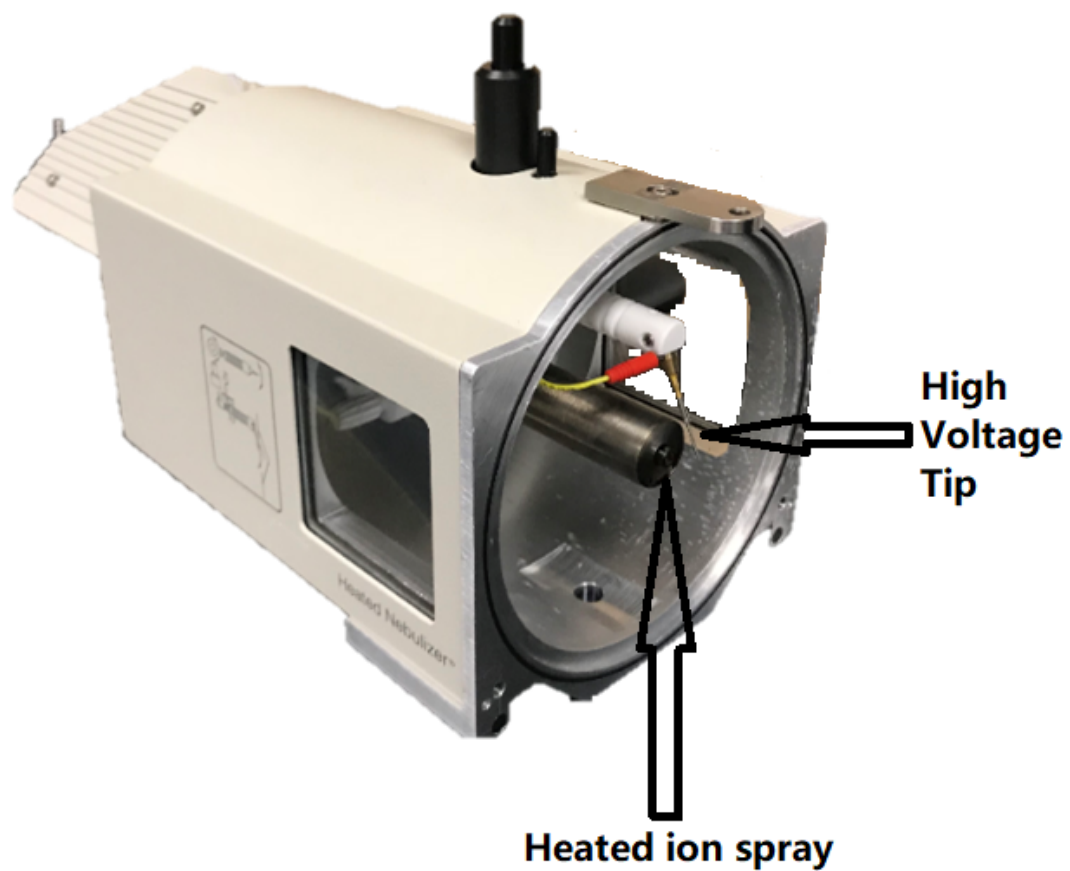


Figure 3.5. Image of the heated nebulizer

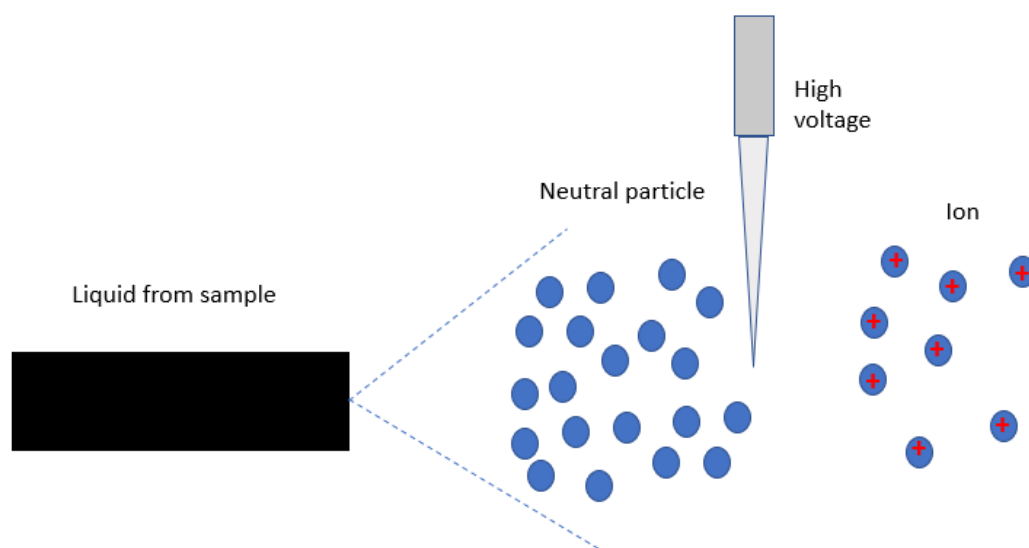


Figure 3.6. The high voltage will ionize the aromatic molecule directly which can not take charge using acidic solution

of TNT, or the DMA potential where the peak of TNT appears is acquired, this potential will be recorded. In the following test, the DMA potential will be set as constant using the recorded value.

Fig. 3.7 and Fig. 3.8 show the basic idea of detecting TNT from the vaporized solution. A T-shape collection chamber is utilized. Dry air flow enters the chamber from one side of the horizontal and exit the chamber from another side which is connected to the DMA-MS system. Before applying the flow, a droplet of TNT solution is added to the chamber from the vertical side, and then the vertical entry will be closed. Acetonitrile is selected as the solvent of TNT since it can evaporate quickly. Let the solution droplet evaporate for 5 minutes, and the whole chamber will be filled with TNT molecule, although at a low concentration. The next step is starting the dry air flow, the flow will bring the air in the chamber to the DMA together with the TNT molecules. Before the TNT molecules will pass through another chamber attached to the DMA before entering the system. Showed in Fig. 3.8, an electrospray of ammonium acetate is generated to ionize the TNT in the coming air flow. On the left side of the chamber, there is another entry to release the air pressure from the dry air carrying TNT and the counter flow in the DMA.

The concentration of charging solution used in the first step is high for the ionization of TNT which will trigger to an issue. Other substances are also likely to be charged when using such a high concentration of ammonium acetate. Thus, the next step is to determine the most appropriate concentration of charging solution. In this test, the concentration of TNT solution is  $320 \mu\text{g}/\text{ml}$ , which is very high to ensure the intensity of the signal. The potential of DMA is kept constant as the value obtained in the previous test. After starting the DMA test, an impulse of dry air is given to generate a signal peak in the constant potential mode. Record the relative intensity of different substance under the same potential. If the signal from TNT is still the strongest peak, it can be considered that the concentration is workable. A low concentration is favored since it can reduce the impurity in the spectrum, as long

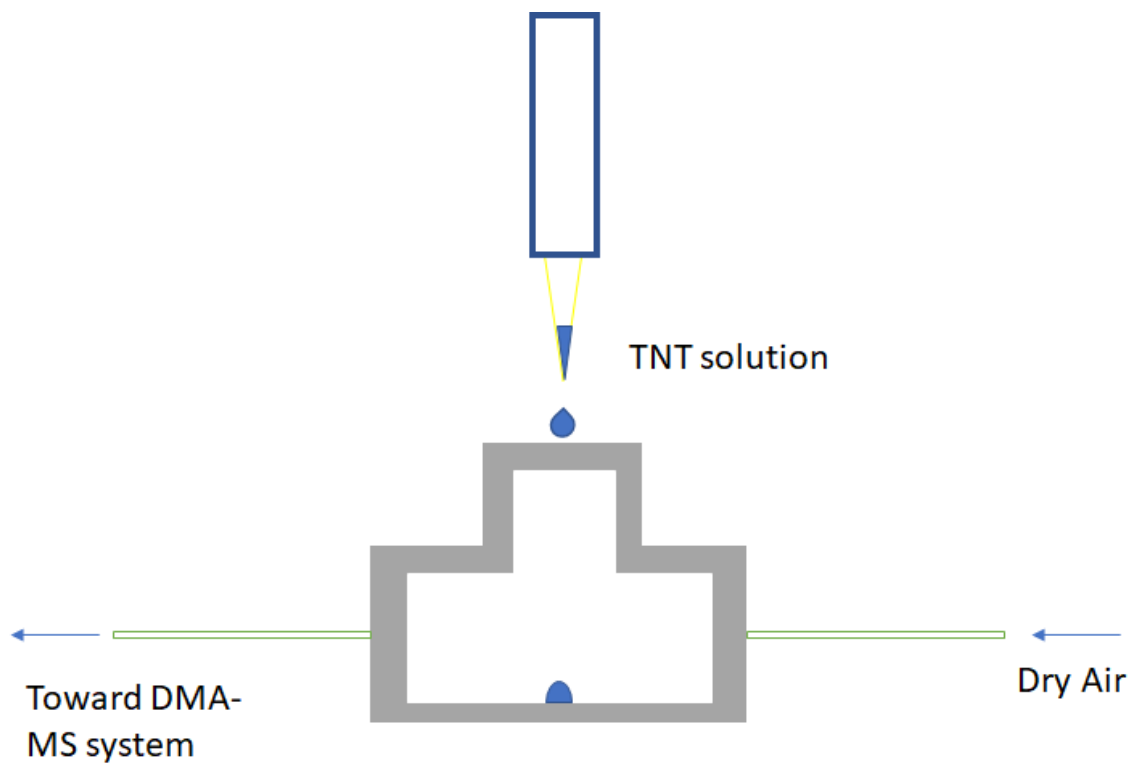


Figure 3.7. Detection of TNT from vaporized solution

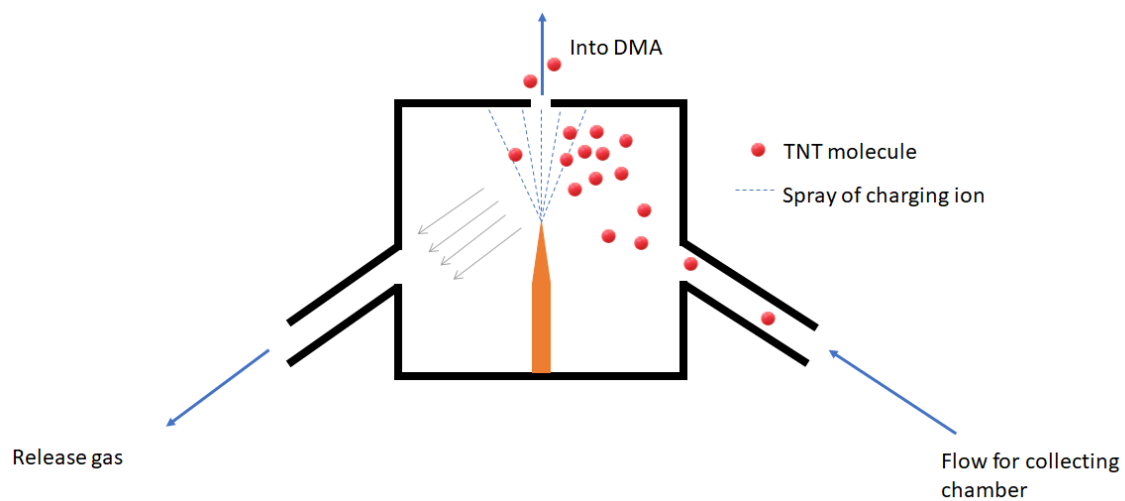


Figure 3.8. Ionization of TNT

as it is workable. 8mM, 15mM, 23mM and 30mM of ammonium acetate are tested in this group of experiment.

Finally when the concentration of ammonium acetate is determined, the test of low concentration of TNT solution will be unleashed. TNT solution of 64  $\mu\text{g/ml}$ , 48  $\mu\text{g/ml}$ , 32 $\mu\text{g/ml}$ , 16  $\mu\text{g/ml}$  and 160 ng/ml are tested. After each time of testing, the collection chamber will be cleaned carefully using acetone and methanol. The volume of the TNT solution droplet is kept 50  $\mu\text{l}$ .

### 3.3 TNT Detection from Enclosed Environment

The former experiment will reach its limit soon, and one obvious shortcoming of this test is that the TNT in the environment is not existing in the solution. To achieve a highly sensitive detection of TNT, a novel mechanism is tested here. Shown in Fig. 3.9, on the right side, the collection chamber is connected to dry air flow as previously as well as a vacuum pump. On the left side, the chamber is connected to the DMA-MS system as well as an enclosed reservoir. The reservoir (500ml) is built to simulate the environment with TNT vapor. Two 3-way clockstops is used to switch the "inhale mode" and "release mode". In the "inhale mode", the way to DMA-MS system and dry air is closed, therefore the chamber is connected with vacuum pump and reservoir. Put a droplet of TNT solution with low concentration in the reservoir. After the evaporation, turn on the vacuum pump and the air in the reservoir will be inhaled toward the chamber. On the right part of the chamber, a filter paper is attached, so when the air included TNT molecules passes through, some of the particles will be absorbed on the paper. Then switch to the "release mode". Switch the clockstops so that the chamber is connected with dry air source and the DMA/MS system. Heating the collection chamber so the TNT can be released from the filter paper. After 5 minutes, turn on the dry air flow, the air with TNT molecules inside the chamber will be carry to the DMA/MS system. Charged by the electrospray of ammonium acetate solution, the mass spectrum can be obtain. The concentration of

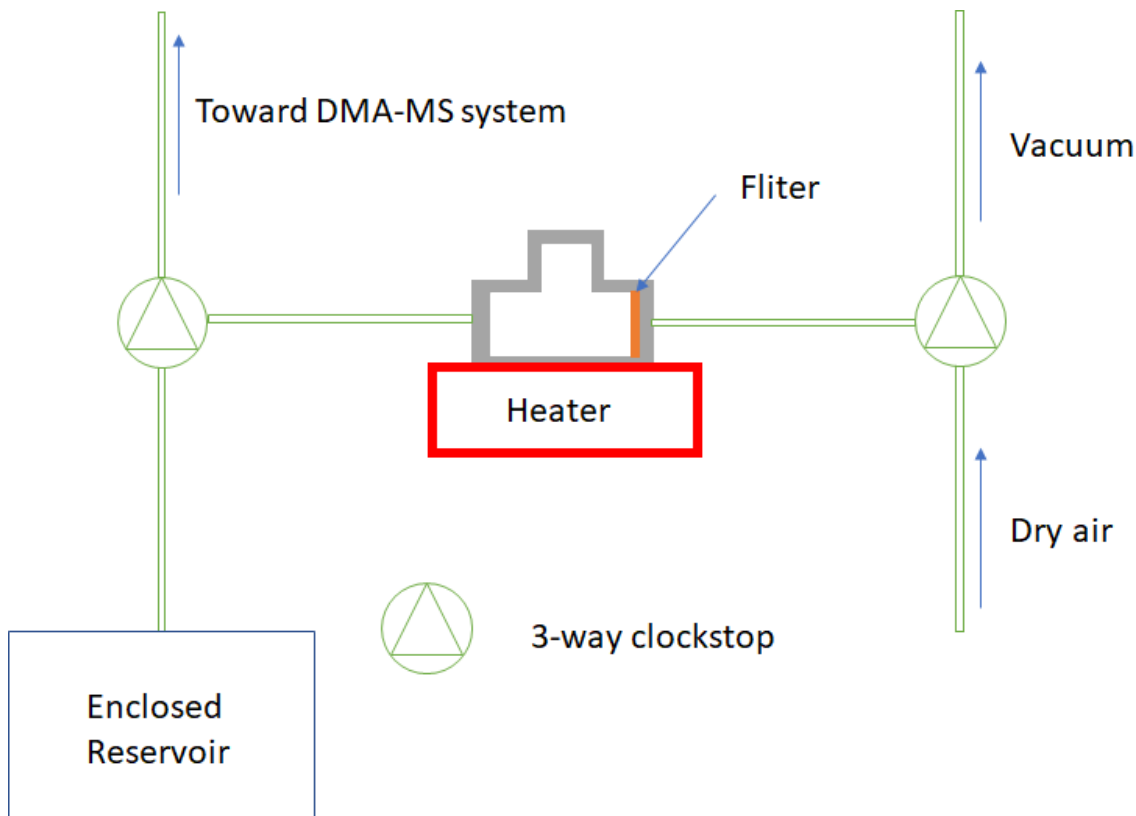


Figure 3.9. Detection of TNT from enclosed environment

TNT solution is selected as 400 pg/ml, 20 pg/ml, 1 pg/ml, 40 fg/ml, 2 fg/ml and 100 ag/ml, and the volume of the droplet is kept 50  $\mu$ l. The corresponding sensitivity is listed in Fig. 3.10. Considering the low concentration used, the MS system will be switch to accumulation mode, under which each count of signal will be accumulated and eventually come to a summation of total signal recieved. Be careful that after each trial the reservoir should be cleaned thoroughly by acetone and methonal to ameliorate the influence of residual TNT.

Fig. 3.11 shows the mechanism of the filter paper. In order to make it easier for the release of TNT molecule, we form a layer of acetone in front of the filter paper. When the TNT molecules in the reservoir are inhaled and pass through the filter paper, it will be absorbed by the acetone, in which TNT has a high solubility.(Fig. 3.12) When

<b>TNT Concentration (g/ml)</b>	<b>Sensitivity (parts per quadrillion)</b>
400 pico	4167
20 pico	208.3
1 pico	10.42
40 femto	0.4167
2 femto	0.02083
1 atto	0.001042

Figure 3.10. Sensitivity of the Test of different concentration of TNT

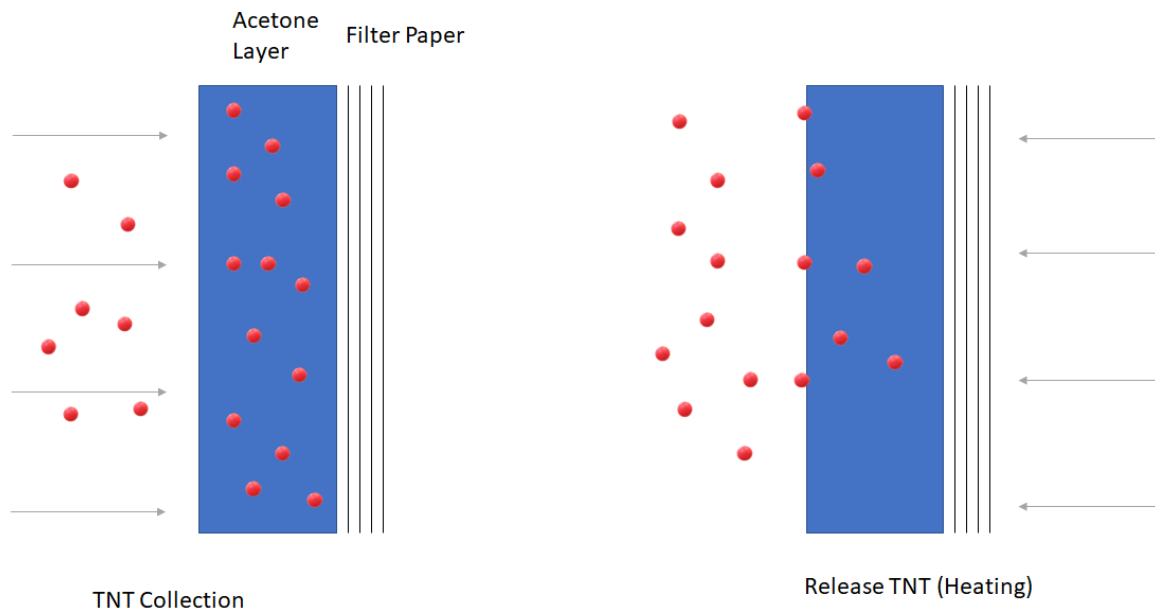


Figure 3.11. Absorb and Release TNT molecules

switching to the "release mode", higher temperature will accelerate the evaporation of acetone, then the TNT molecules will be released back to the chamber and pushed to the DMA. Temperature of 120 C, 150 C and 180 C for every concentration is tested. To enhance the heating performance, in this test the collection chamber is wrapped with aluminum foil.(Fig. 3.13)

Solvent	Solubility (g/100g)
Toluene	55
Methyl acetate	72.1
Acetone	109
Chlorobenzene	33.9
Benzene	67
1,2-Dichloroethane	18.7

Figure 3.12. Solubility of TNT in different solvent



Figure 3.13. Collection Chamber used in the experiment, wrapped with aluminum foil

#### 4. NUMERICAL PROCESS OF THE OPTIMIZATION

At the beginning of the optimization work, a quadric equation was established for the error calculation, which is expressed as:

$$F(\epsilon_1, \sigma_1, \epsilon_2, \sigma_2, \dots, \epsilon_k, \sigma_k) = \sum_{i=1}^n \left( 1 - \frac{\Omega_{iCalc}(\epsilon_1, \sigma_1, \epsilon_2, \sigma_2, \dots, \epsilon_k, \sigma_k)}{\Omega_{iExp}} \right)^2$$

Here  $\Omega_{iCalc}$  and  $\Omega_{iExp}$  represent the collision cross section value for calculated results and experimental results respectively. The index  $i$  denote the  $i^{th}$  molecule in the entire group of molecules with number  $n$ . In order to prevent mathematic indetermination, number  $n$  is required to be larger than  $2k$ . Now the target is to achieve the minimum value of  $F$  then the error between calculated and experimental values will be minimized. If the calculated CCS agree with their experimental counterparts, the

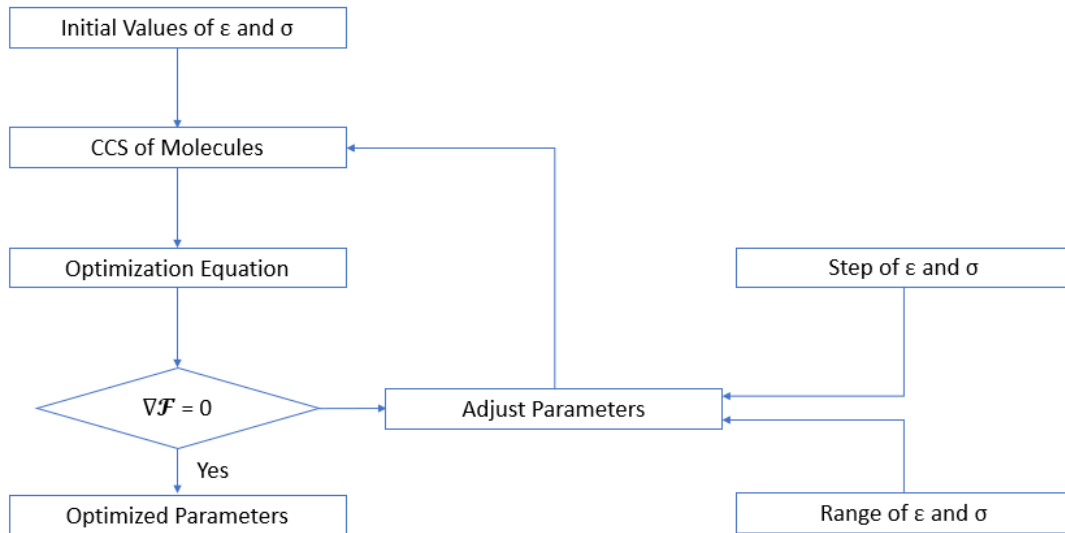


Figure 4.1. Numerical Process of the Optimization of Parameters

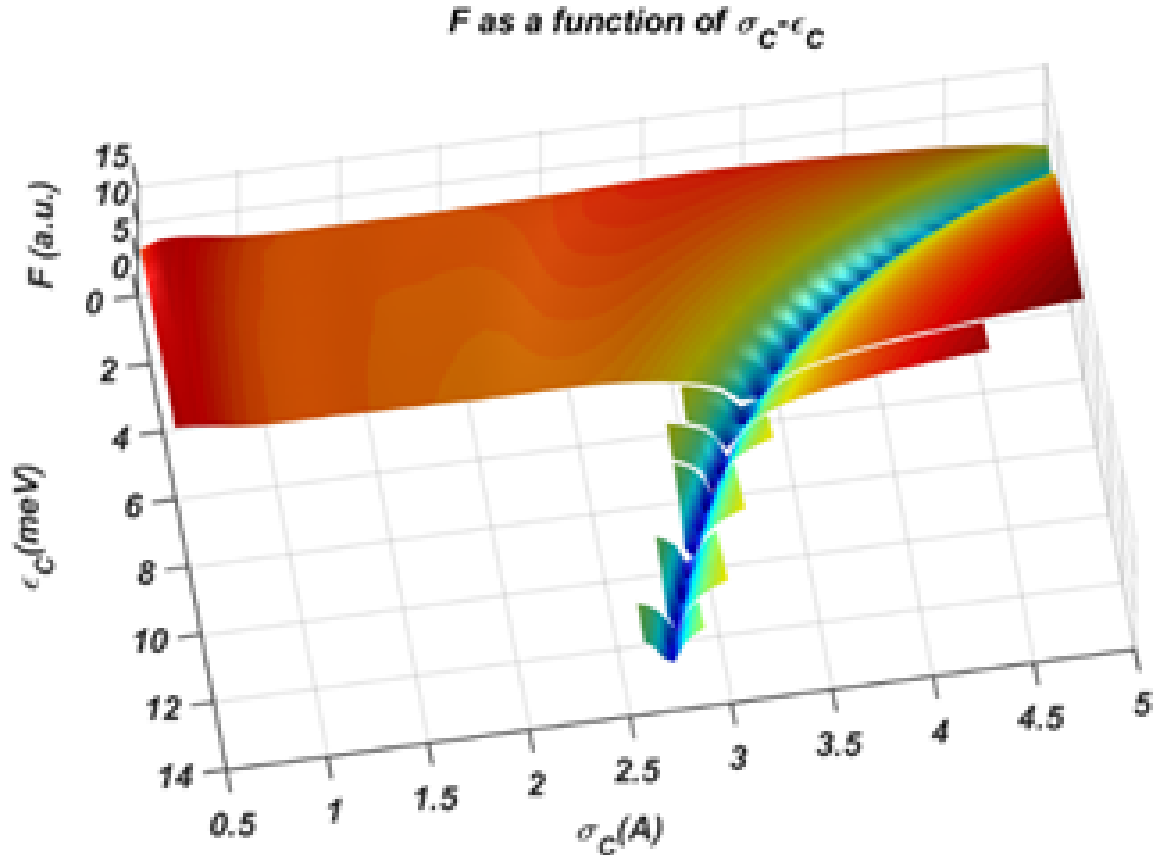


Figure 4.2. A wide surface mapping of  $F$  for the Carbon atom extended in the region of interest.

value of  $F$  will become zero. Then this goal in mathematics will be translated as a zero gradient:

$$\nabla F(\epsilon_1, \sigma_1, \epsilon_2, \sigma_2, \dots, \epsilon_k, \sigma_k) = \left( \frac{\partial F}{\partial \epsilon_1}, \frac{\partial F}{\partial \sigma_1}, \frac{\partial F}{\partial \epsilon_2}, \frac{\partial F}{\partial \sigma_2}, \dots, \frac{\partial F}{\partial \epsilon_k}, \frac{\partial F}{\partial \sigma_k} \right) = 0$$

With the simple and straightforward mathematical expression above, the physical interpretation for the process might be abstract. Function  $F$  established is only a quadric function with  $2k^{th}$  variables without taking the physical phenomenon into account, which might trigger to the function cannot provide a physical solution.

The chosen option for the optimization is to keep the rest L-J parameters for other elements be unchanged and optimizing only one element one moment through

a *ceteris – paribus* all-mapping technique. Although the process is mostly computationally based, some physical explanation of the results can be acquired too. The process is summarized as the following:

1. Select the initial element, for example carbon, for the optimization of  $F$
2. Optimize  $F(\epsilon_c, \sigma_c)$ , for the Lennard-Jones parameters,  $\epsilon_C$  and  $\sigma_C$ , of the initial element while the parameters for other elements will be kept constant in this round ( $\epsilon_N, \epsilon_N, \epsilon_H, \epsilon_H, \text{etc}$ ). Since there are still other elements are not optimized yet, the result of  $F$  after this round of optimization will probably not be zero. The region of interest will be mapped in order to present more straightforward information
3. Repeating the same action in step 1 and step 2 described towards other elements to complete the whole optimization
4. Go to the beginning, iterate from the initial element again, doing the calculation using the newly gained parameters for all elements, repeat step 1 to step 3
5. Continue the optimization by iterating all the previous steps under the results of optimized Lennard-Jones parameters follow a convergent criterion

The concept of surface mapping is presented in the following as a block diagram. Each figure depicts the algorithm layout for one element. Briefly speaking, before starting the optimization, an interval and a step size would be chosen for both the well-depth and intercept for the elected element. Under certain well-depth and intercept, the CCS will be calculated by IMoS. As all the parameters kept unchanged for the rest elements, the value of  $F(\epsilon_i, \sigma_i)$  would be calculated, where the subscript  $i$  represent the element being optimized. Several thousand of CCS values would be obtained during this process, those values will be parts of the surface mapped. The experimental CCS for these 16 molecules, which appear in Table I, were obtained directly from a careful analysis from Campuzano, which use the same strategy of Trajectory Method algorithm in the optimization of L-J parameters in the buffer gas of nitrogen. Those

results could be a good comparison for the experimental in our experiment, which do not combine the ion-quadruple potentials yet.

For the numerical calculation of the collision cross section, the initial positions of the atoms in the molecule, which means their geometric structures need to be determined by some reliable approach. The motions of atoms would be constant while the structures of molecules could suffer deformation after the collision. The optimal positions of the atoms in a molecule indicate the balance of the forces between each part of the molecule, can be well estimated by the hybrid functionals in differential functional theory (DFT). For now, the influence of pressure and temperature of the environment were not taken into consideration yet, therefore those structures cannot be considered as the average positions of the atoms. However, for the rigid and small size molecules, the DFT calculations can provide a well-defined geometry of the molecule which can be utilize in the Lennard-Jones parameters optimization as well as CCS calculation. Something need to be noticed is that the CCS obtained by DFT calculation should be used carefully as the geometric structures used by other methods will somewhat include the temperature and pressure factors.

Using Chem3D Pro v.12(Perkin Elmer) and MM2 calculations, the initial structures for the 16 molecules were generated and presented in the Table I. Calculations of frequency and geometry optimization were undertaken using different Becke-Lee-Yang-Parr and Becke-Perdew type functionals including cam-b3lyp, b3pw91, bpv86 and b3lyp. The Pople split-valence basis set used was the 6-31++G(d,p) with diffuse and polarization functions. By most the functionals applied the results are very similar that the difference exist can be neglected in the CCS calculation and resulting structures have been added to the supplemental information. Both Mulliken and Hirshfeld partial charges were calculated. Even though after using different functionals in the DFT and the geometric structures with significant difference in the locations of partial charge were obtained, in the CCS calculation they did not show crucial discrepancy. Here we did not employ QTAIM and NBO methods. For generalization

purposes, the choice of partial charges in the calculations shown are from the Mulliken approach.

With the foundation of the structures acquired from DFT modification, the CCS would be calculated numerically using Ion Mobility calculator IMoS. Using Trajectory Method with a 4-6-12 potential, the Lennard-Jones and ion-induced dipole, is chosen as the approach of calculation, while for now the ion-quadrupole interaction is excluded. Its polarizability was set to be  $1.7 \times 10^{-24} \text{cm}^3$ . For the running of the program, 8, 16 and 32 cores were conducted indistinctively. For the amount of the gas molecules,  $9 \times 10^5$  was fixed in every trial in these calculations. Each molecule will only take a few seconds to complete the calculation under most circumstances. The total time to accomplish the mapping of the surface of CCS with several thousand of corresponding results. For the calculation using gradient descent method, the number of gas molecules will increase to  $3 \times 10^7$ , in order to enhance the accuracy when the error in the program went too large for the appropriate definition of the gradient. Output of the IMoS code for a sample calculation has been added to the supplemental information.

## 5. RESULTS OF THE OPTIMIZATION

### 5.1 The Optimization Using the First Group of Chemicals

For the initial run of the optimization process using *ceteris paribus* approach, two elements were chosen to start up the calculation. Two routines were therefore determined, begin with hydrogen or begin with carbon. The reason why we have two starting elements is to ensure there are no significant bias for the initial calculation. No matter which routine the process is running, the original values for their first step Lennard-Jones parameters for each atom would not be needed. Meanwhile, the Lennard-Jones parameters from previous studies would be taken to make a comparison with. For those specific parameters, using the TM method with and without the ion-quadrupole potential, Table I also shows the numerical CCS and its error when compared to the experimental CCS. The average error is also provided at the bottom of the table.

#### 5.1.1 Optimization Starting With Carbon

**First round of iteration** Fig. 5.1 shows the mapped  $F$  surface as a function with two variables,  $\sigma_{C,1}$  and  $\epsilon_{C,1}$ , while keep the rest parameters unchanged. Notice that the index indicate these parameters are the results for the first round of iteration. The  $\sigma_{C,1}$  and  $\epsilon_{C,1}$  values will be given in Angstroms and meV respectively, altering by step of 0.1 in the calculation, and be input in the equation of  $F$  to compute its different compared to the experimental CCS. The value of  $F$  appearing in Fig. 5.1 (and in some surface mapping plots) has been modified and cut at a given height to accent the valley of the minimum for representation purposes. Before the process, ranges of interest for both parameters were selected based on the basic knowledge of this physical reaction. The initial domain for  $\epsilon_C$  is [2,9], and [2.5,4.5] is selected

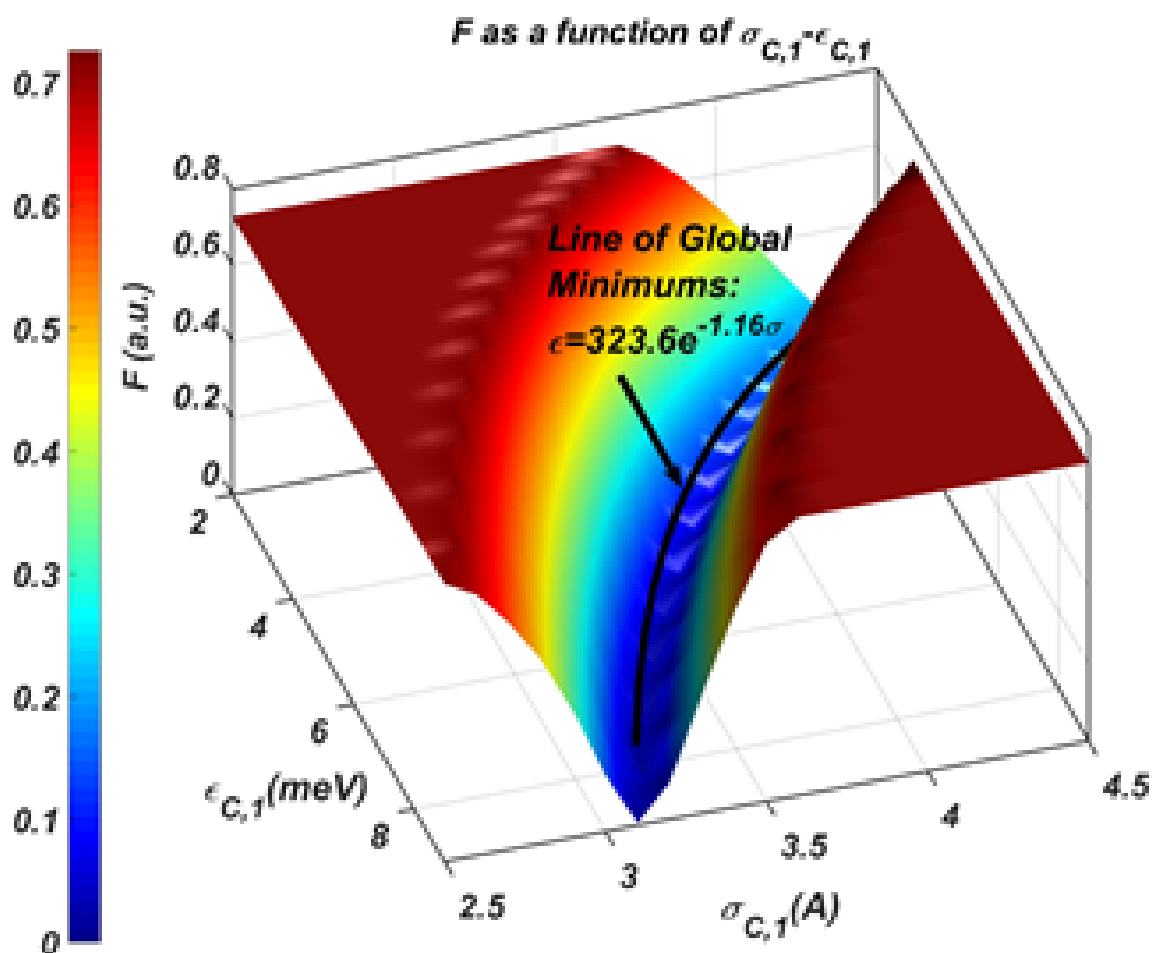


Figure 5.1. The mapped optimization surface of carbon in the first iteration. It can be easily figured out that the minimum is a curve instead of a single point

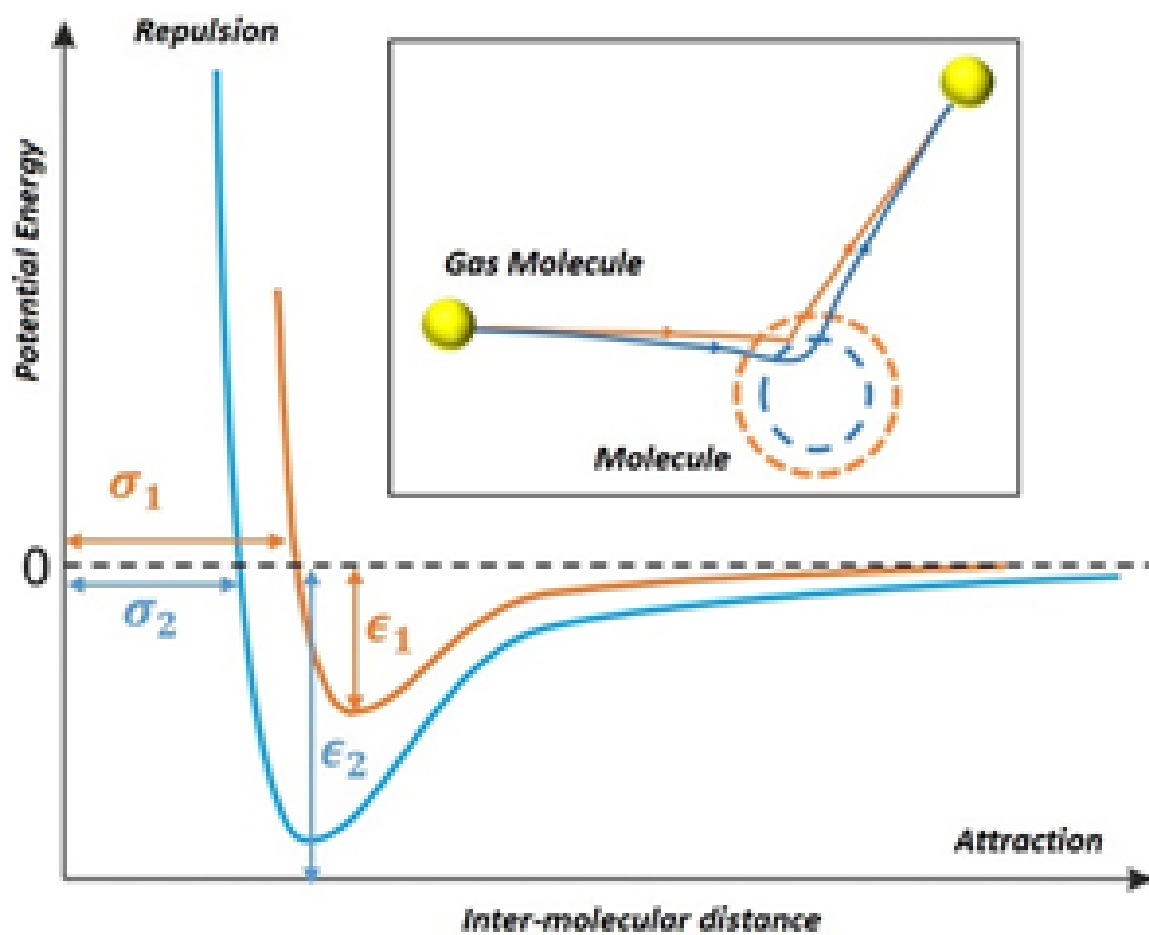


Figure 5.2. Possible mechanism of the global minimum line: two different routine of the reemission might generate the identical effect

for  $\sigma_C$ . We will anticipate the values provide the smallest error will lay within these ranges. Figure 5.1 shows a smooth decrease throughout most of the values until a minimum is reached at some  $\epsilon_C$  and  $\sigma_C$  pair. The mapping did not provide a unique value of L-J pair. Instead, a series of well-depth and intercept values were acquired providing the minimal error between experimental and calculated CCS. Therefore we can establish a concept of "line of global minimums", which represents a region where the values of  $\epsilon$  and  $\sigma$  will provide the optimal value of function  $F$ . The plot was extended in the region of interest, and no significant minimum can be found. The optimal point is therefore not singular and there is a relation between the well-depth and the intercept that corresponds to the line of global minimums. This relation can be graphed (see Fig. 5.1) and corresponds to an exponential relation between  $\epsilon_C$  and  $\sigma_C$ . The intercept value is playing a more important role in the exponential function than the well-depth, as the same size of step intercept will make a bigger influence than the well depth does. Although a simple exponential function has already been displayed here, i.e. a similar effect can be achieved by reducing the intercept and increasing the well-depth or vice versa, there is no particular physical reasoning, to our knowledge, other than there is not enough information in the given data to fully separate the parameter interaction. . Fig. 5.2 shows a depiction of two very different instances of  $\sigma$ - $\epsilon$  pairs that will yield very similar values of CCS and therefore similar values of  $F$ . The Consequences of this analysis could be very interesting, having the possibility of correctly defining optimized CCS the most important one. As is demonstrated in the supplemental information, two sets of L-J parameters for Carbon which are very different from each other can give very similar CCS.

Even the optimization provides a line of value can achieve minimal error, we must decide the value of well-depth and intercept pair before continuing the optimization for other elements. Here the intercept was selected to be 3.52 , which is the summation of the VdW radii of nitrogen (1.82 ) and carbon (1.7 ). On the line, the corresponding well-depth for this value is  $5.49\text{meV}$ . These first values for Carbon are in agreement with previous values used in CCS calculations in N2, albeit high for the well-depth.

After finishing the optimization of element carbon, the process will continue following the sequence of hydrogen, oxygen, nitrogen and fluorine. The results are all shown in Fig. 5.3 - Fig. 5.6. Hydrogen and Oxygen, in Fig. 5.3 and Fig. 5.4, present a similar pattern as the mapped surface of carbon as an exponential line. For hydrogen, the ploy is apparently asymmetric. The reason for this unbalance is understood from the effect of Hydrogen as the external-most atom in a molecule. For any constant value of the potential well-depth, and starting from the line of global minimums, increasing the intercept over the line of global minimums has a strong effect in the  $F$  function. In the CCS the increase of intercept means the enlargement of hydrogen atom. Respectively, starting from the line of global minimum, if we decrease the intercept under a constant well-depth will not perform a large change as the varied intercepts do. The overall effect might be softened because of that even the reduction of the effect of the repulsive potential in the hydrogen atoms exist, it will probably be confronted by the increased effect of the heavier atoms close to the Hydrogen atom. This result have a crucial meaning, since it imply that the effects of hydrogen atoms could be embedded while calculating the effect of larger elements, which can lead to the removal of hydrogen in the CCS calculation and increase the efficiency of computation significantly. The value of the Lennard-Jones parameters for hydrogen was  $\epsilon_{H1} = 2.33meV$  and  $\sigma_{H1} = 2.22$ . The option to use a smaller intercept than that of the sum of the VdW radii was made in this case, choosing H to be closer to its covalent radius (40pm) to observe if it would affect the optimization procedure. After obtaining the new value of L-J pair for carbon and hydrogen, oxygen will be put into the optimization. Compared to the elements optimized, the mapped surface will present a wider valley. This phenomenon might be explained as the percentage of oxygen in the tested molecules is respectively low compared to carbon and hydrogen. (The number of oxygen is about 3 percent of the total atom number) Unlike carbon and oxygen, the mapped surface of oxygen seems to have a well-localized global minimum laid in the line of global minimum. Nevertheless, something must be mentioned here is that all the CCS calculated using the parameter values from the line of global

minimum will not have a considerable discrepancy. For the selection of the value of parameters, to keep it reasonable physically, we made it  $\epsilon_{O1} = 4meV$  and  $\sigma_{O1} = 3.45$ .

Following the same procedure, Fig. 5.5 and Fig. 5.6 correspond to Nitrogen and Fluoride elements. The mapped surface of nitrogen is somewhat similar to the surface of oxygen, both of which have a plot of wide valley and there seems to have a line leads to the global minimum. Like the oxygen, nitrogen would have a small weight in all the atoms, the percentage of nitrogen is only around 1 percent. From the surface of nitrogen, the intercept  $\epsilon$  can hardly affect the results of function  $F$ , and the valley of minimums will decline as the well-depth increases. There is a possible explanation of this phenomenon: all the chemical compounds contain nitrogen atoms selected to be studied will center the nitrogen in the molecular structure, so its influence from well-depth will not be apparent, since other particles will rarely collide with the nitrogen atoms directly. The L-J parameters chosen for nitrogen would be  $\epsilon_{N1} = 5meV$  and  $\sigma_{N1} = 4.2$  for the first round of iteration. The last element to be optimized is fluorine. Fluoride only appears in 2 molecules (and only 2 atoms) of two very similar epimers: betamethasone and dexamethasone. The influence of fluorine will be also quite small toward the studied molecules and therefore, any value change of the L-J pairs will not modify the optimization function  $F$  substantially. In particular, for this first iteration, there is not a marked minimum anywhere for the Fluoride atom, in contrast with the rest of the atoms. A pair of values that  $\epsilon_{F1} = 0.75meV$  and  $\sigma_{F1} = 3.5$  were selected in order to continue the next round of iteration.

**Second round of iteration** Fig. 5.7 - Fig. 5.10 show the results for Carbon (Fig. 5.7, Fig. 5.8) and Hydrogen (Fig. 5.9, Fig. 5.10) for the second iteration when compared to the first iteration. In order to prevent excessive computational time, the calculated range of values has been narrowed to the region of interest. Compared to previous mapped surface, the surface of carbon and hydrogen for the second round of iteration have shifted slightly. Meanwhile, the minimum value of function  $F$  are closer to zero. In another word, the optimization process is running in a convergent

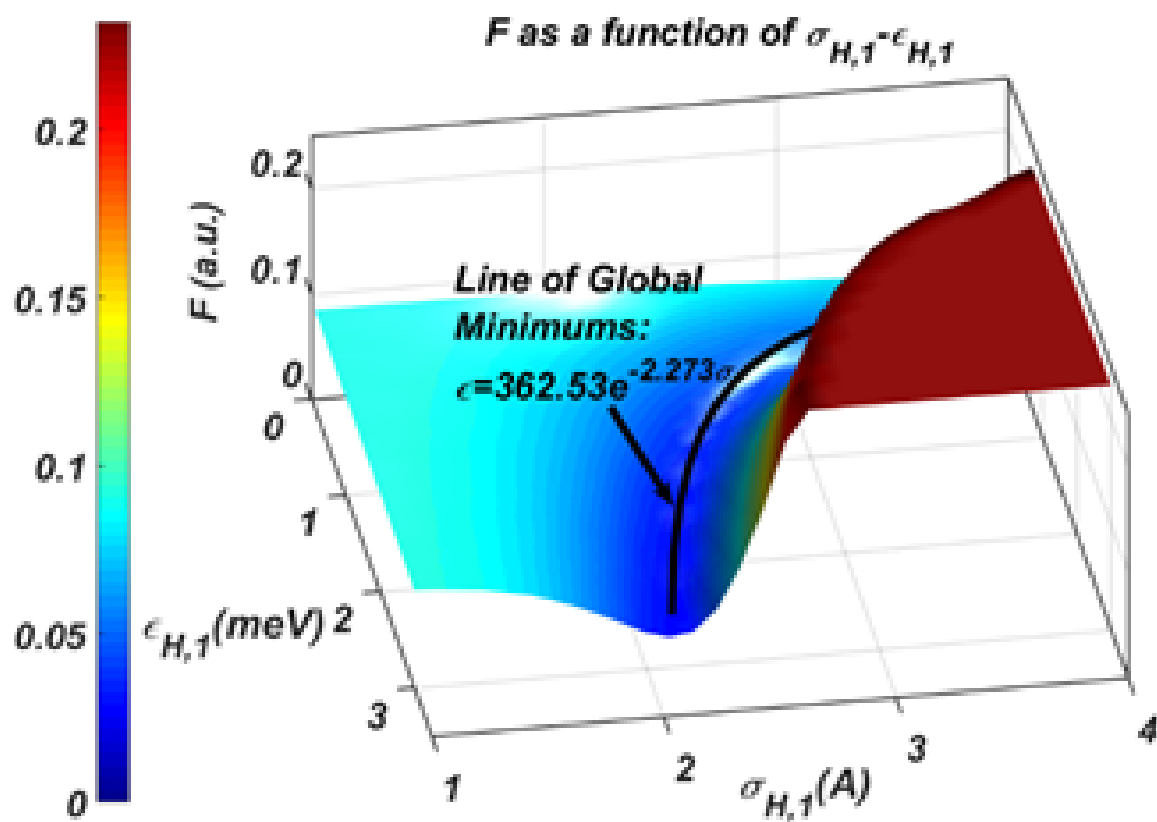


Figure 5.3. Mapped Surface of Hydrogen of the first iteration

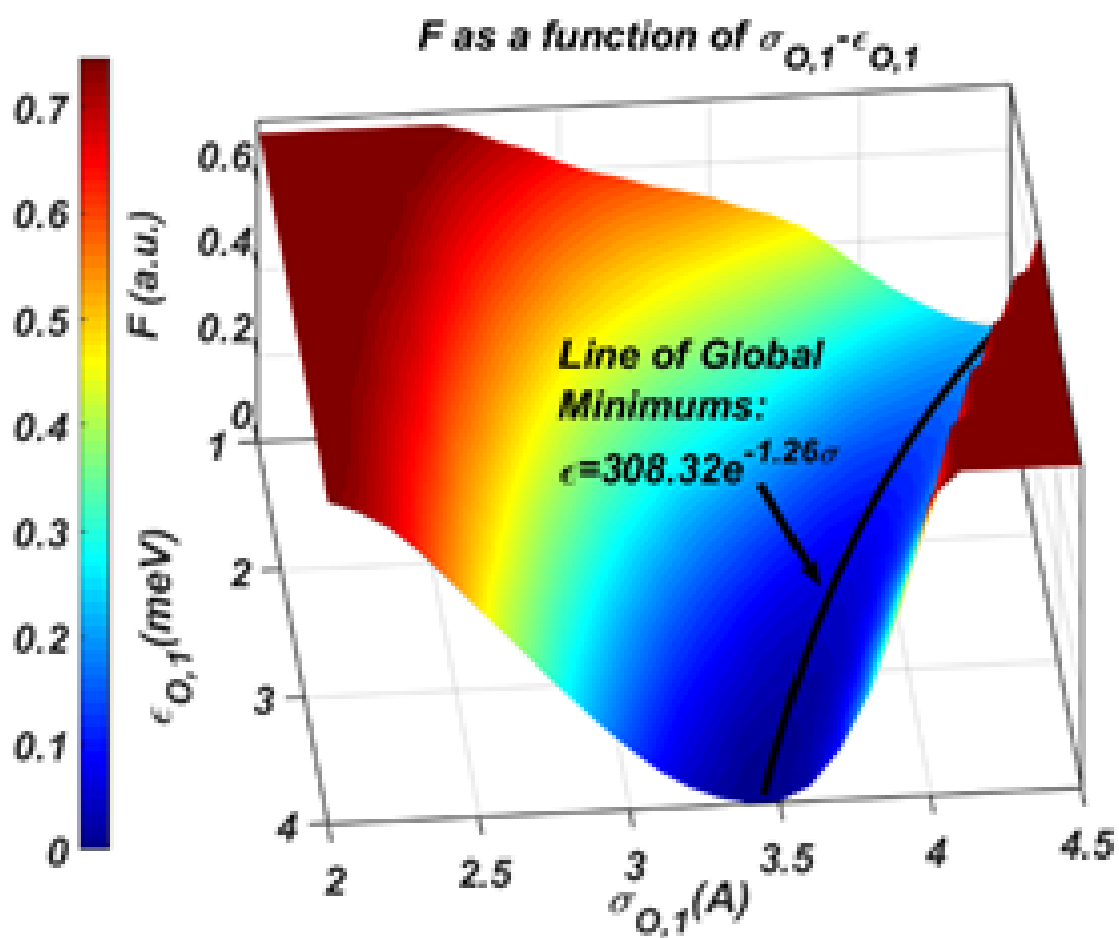


Figure 5.4. Mapped Surface of Oxygen of the first iteration

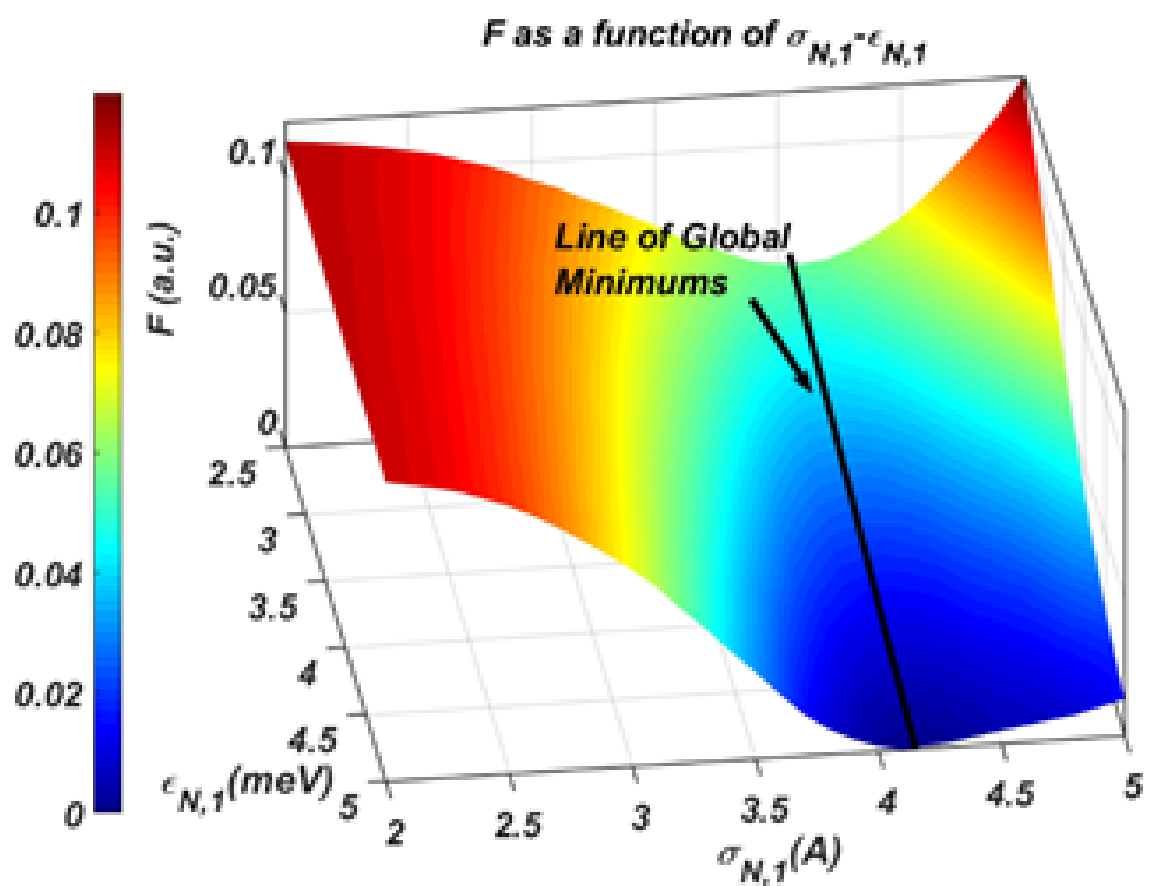


Figure 5.5. Mapped Surface of Nitrogen of the first iteration

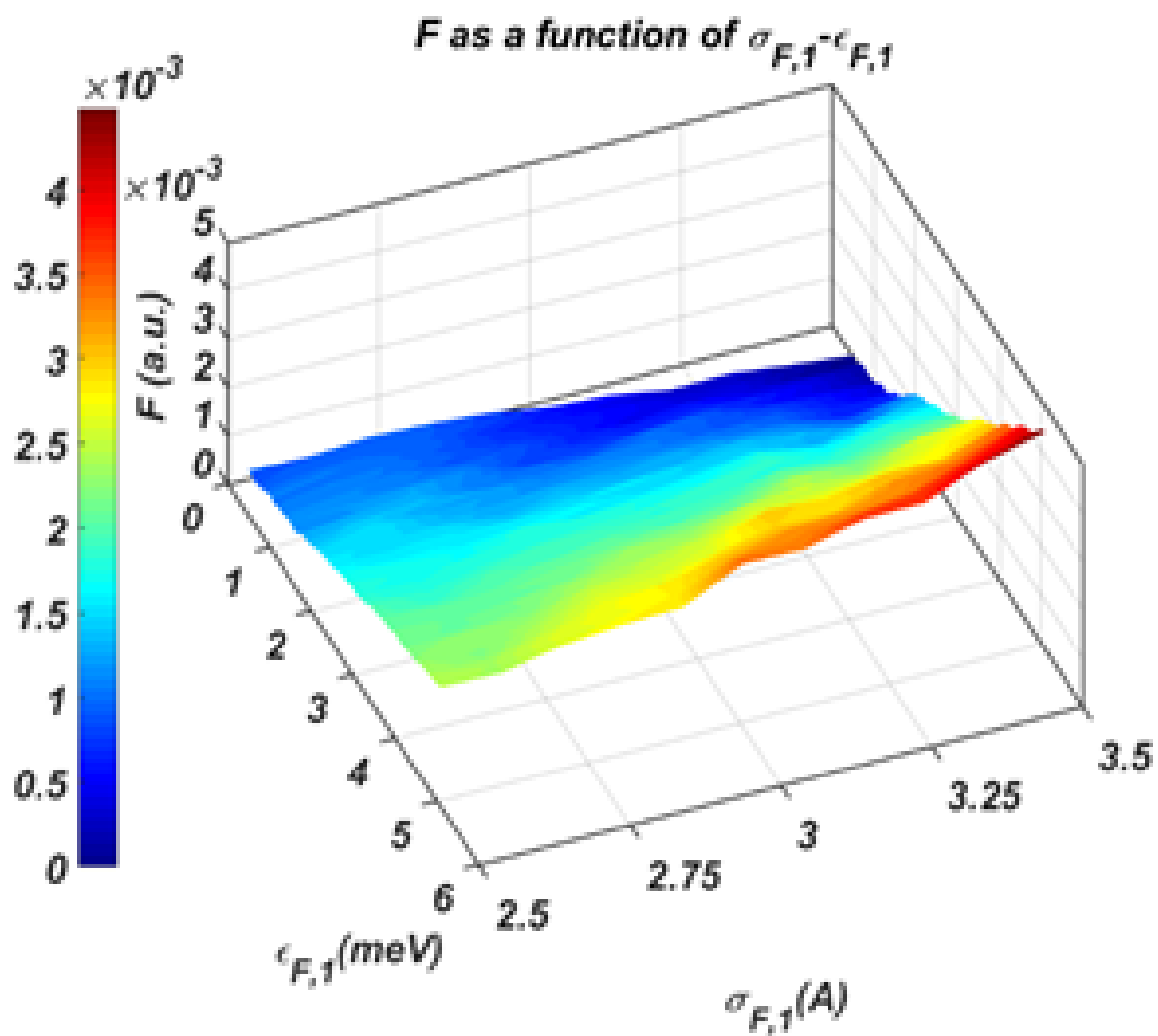


Figure 5.6. Mapped Surface of Fluorine of the first iteration

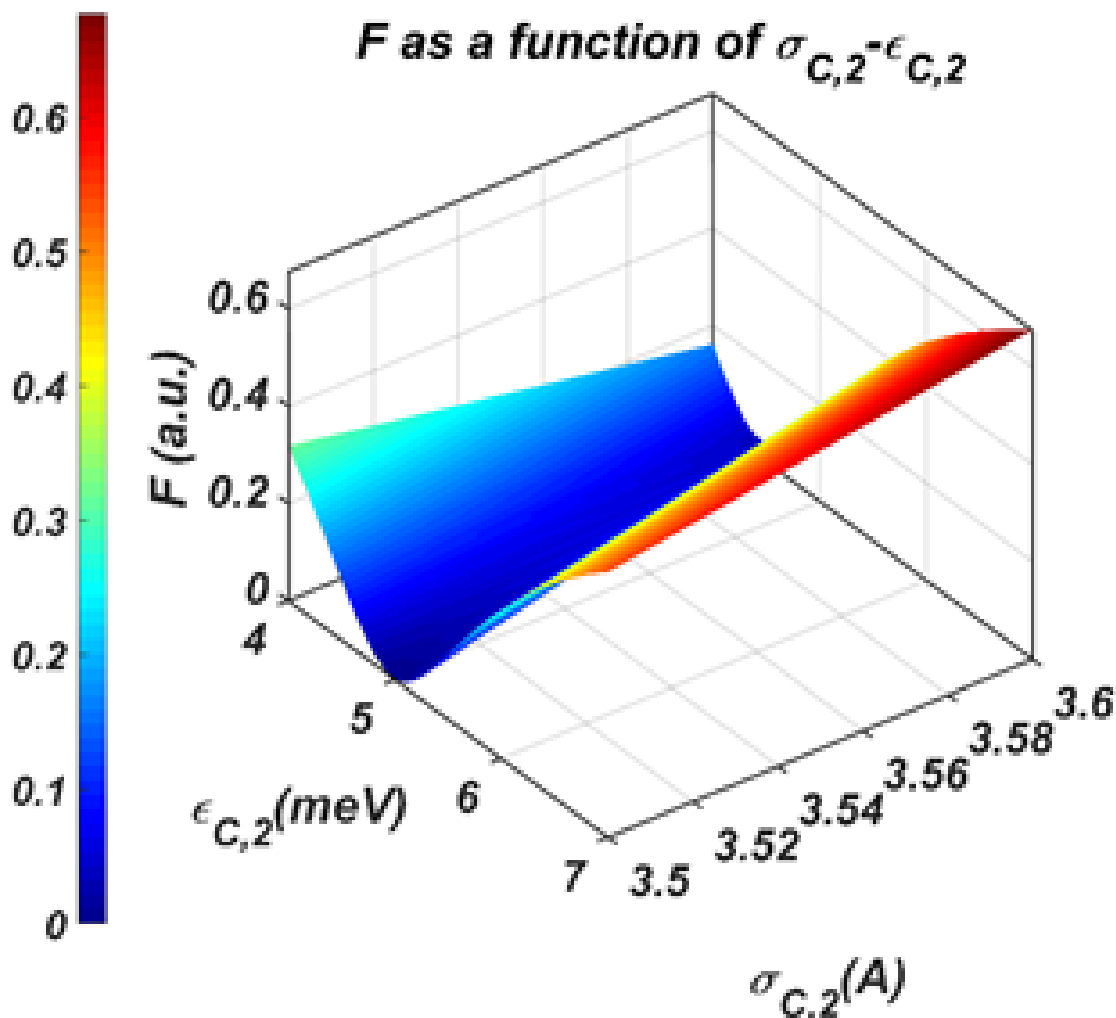


Figure 5.7. Mapped Surface of Carbon of the second iteration in the interest region

way. Overall, the parameters were selected as previously. For carbon,  $\epsilon_{C_2} = 5meV$  and  $\sigma_{C_2} = 3.52$ . For hydrogen,  $\epsilon_{H_2} = 3meV$  and  $\sigma_{H_2} = 2.2$ .

Fig. 5.11 -Fig. 5.13 shows the results for the second iteration for Oxygen, Nitrogen and Fluoride. The trends for Oxygen and Nitrogen are very similar with values shifting slightly from those of iteration 1. An emphasis must be made on the fact that the range of values of  $F$  varies very little in the scrutinized region so the error in

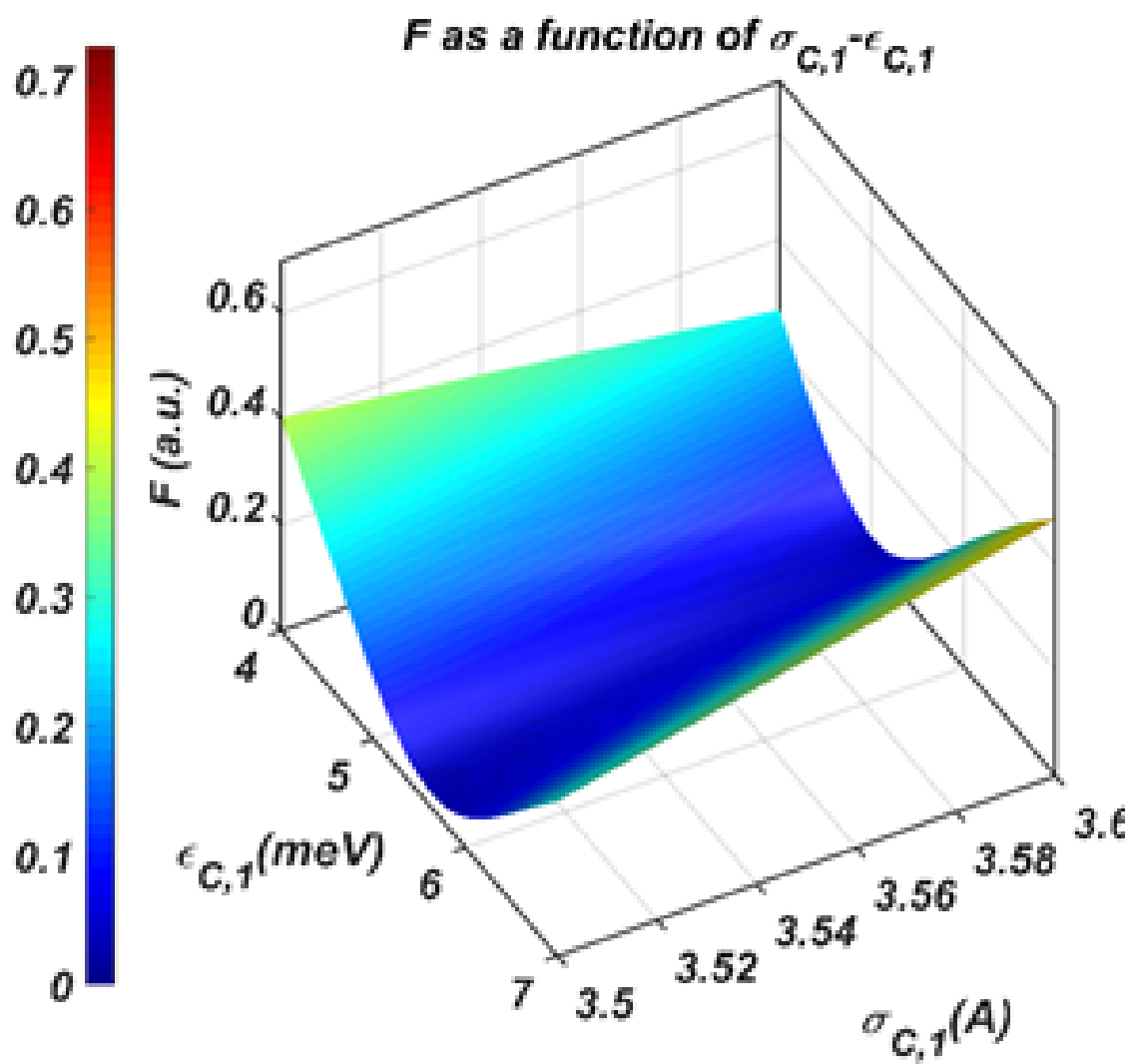


Figure 5.8. Mapped Surface of Carbon of the first iteration in the interest region

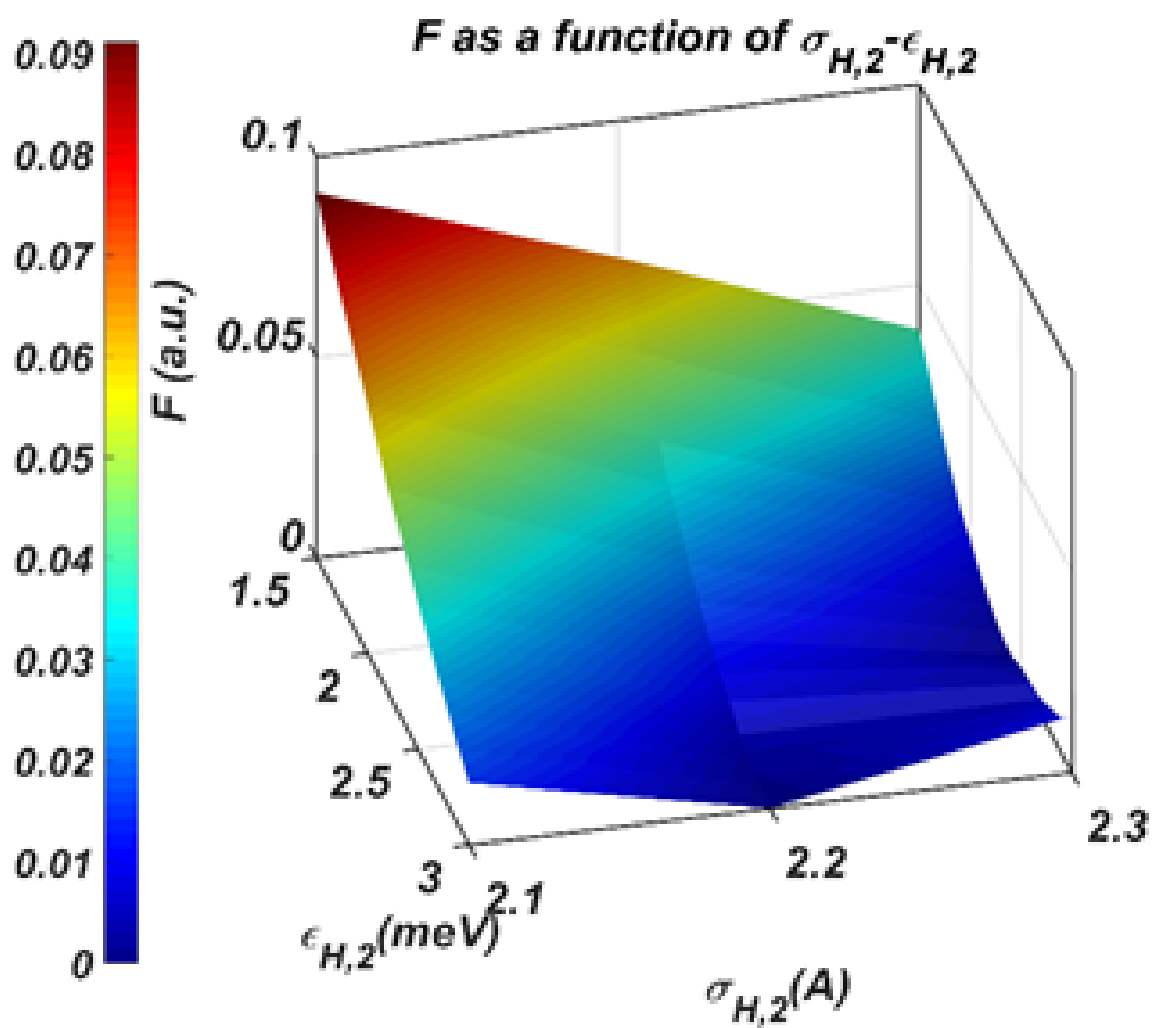


Figure 5.9. Mapped Surface of Hydrogen of the second iteration in the interest region

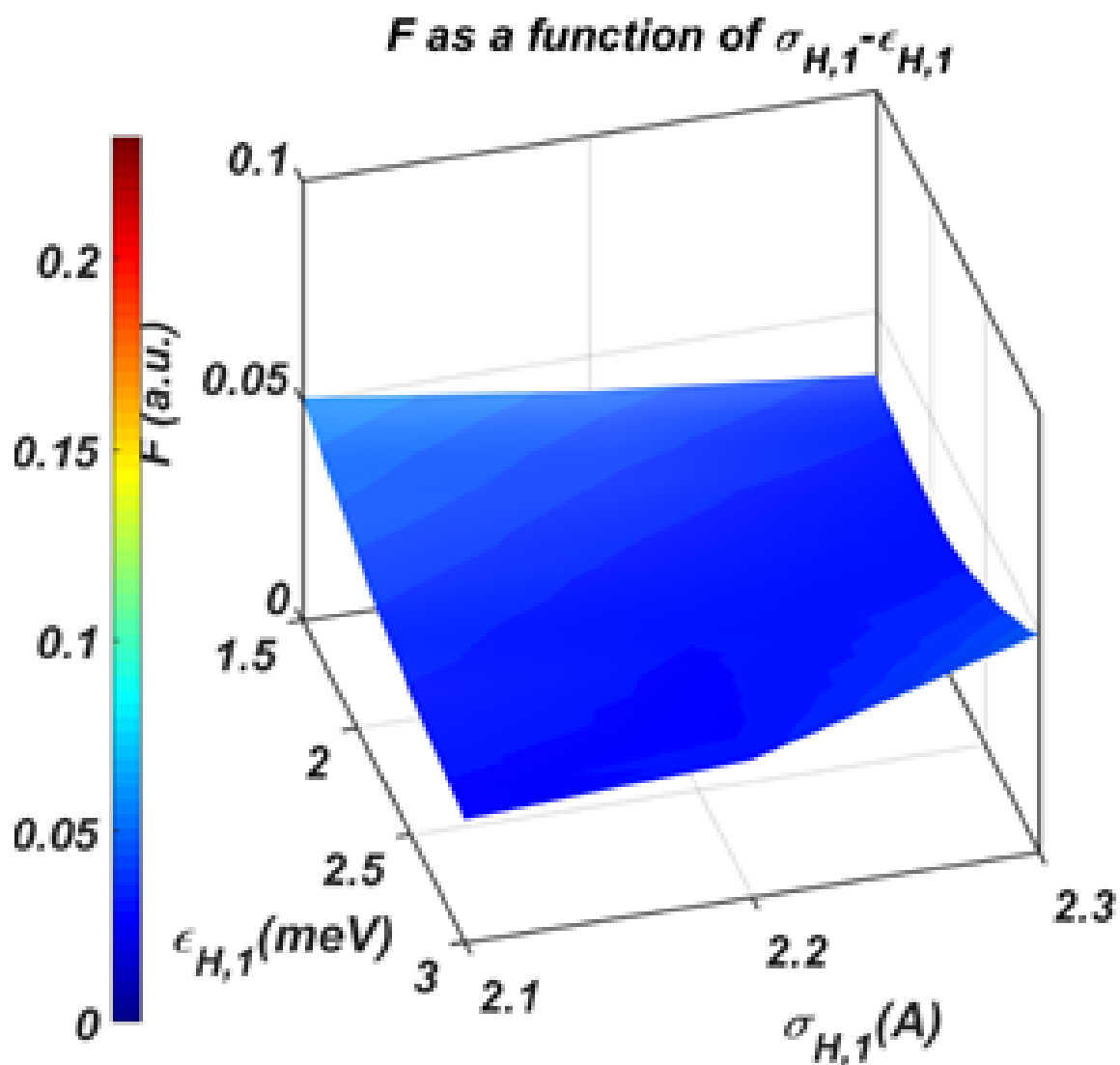


Figure 5.10. Mapped Surface of Hydrogen of the first iteration in the interest region

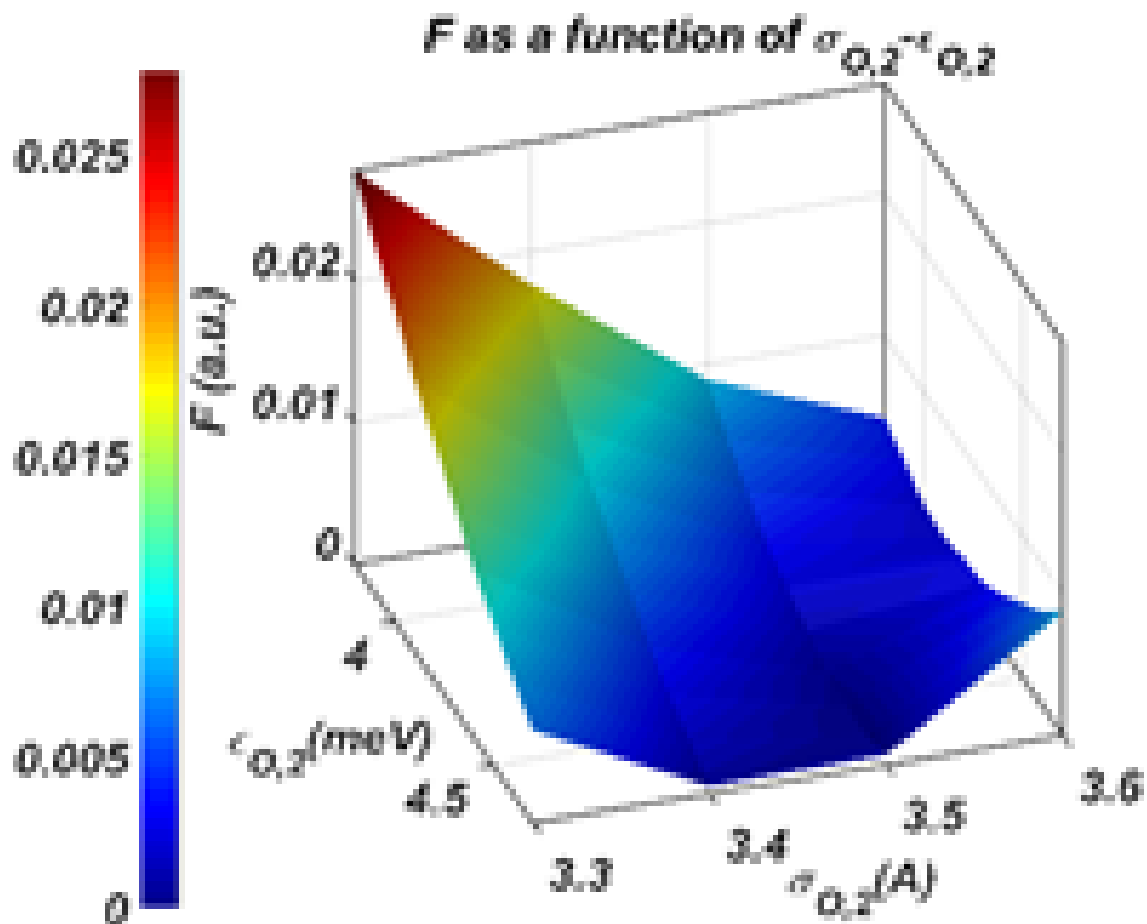


Figure 5.11. Mapped Surface of Oxygen of the second iteration in the interest region

the CCS from any of the values in the range selected is expected to be not more than 2 percent. The chosen parameters would be  $\epsilon_{O_2} = 4.3\text{meV}$  and  $\sigma_{O_2} = 3.5$  for oxygen and  $\epsilon_{N_2} = 5\text{meV}$  and  $\sigma_{N_2} = 4.1$  for nitrogen. For this round of iteration, the fluorine atom shows a global minimum in its mapped surface. Only very tiny changes can be observed in this round of optimization. Furthermore, the limitation of accuracy using  $9 \times 10^5$  as the number of gas molecules is becoming more apparent from the wavy pattern. Now the value of Lennard-Jones parameters for the fluorine after this round would be  $\epsilon_{F_2} = 1.2\text{meV}$  and  $\sigma_{F_2} = 3.4$ .

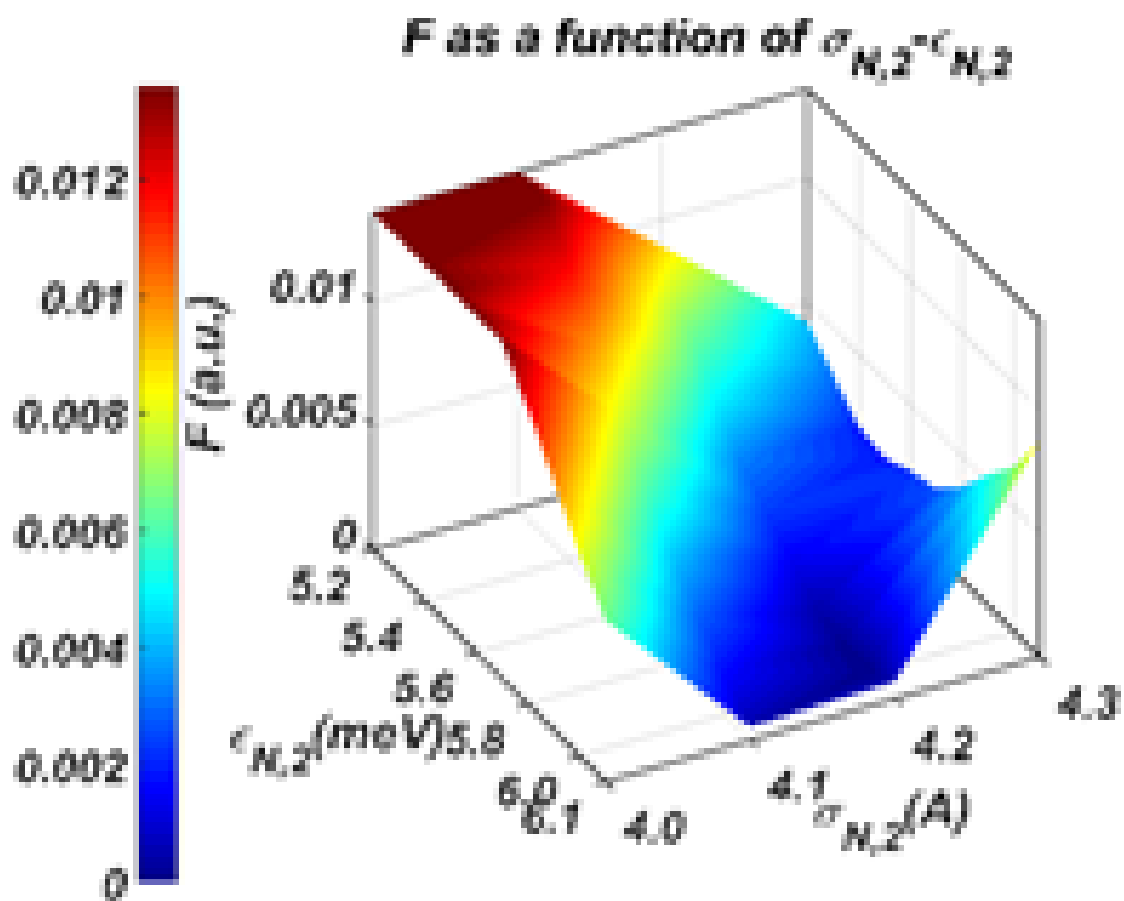


Figure 5.12. Mapped Surface of Nitrogen of the second iteration in the interest region

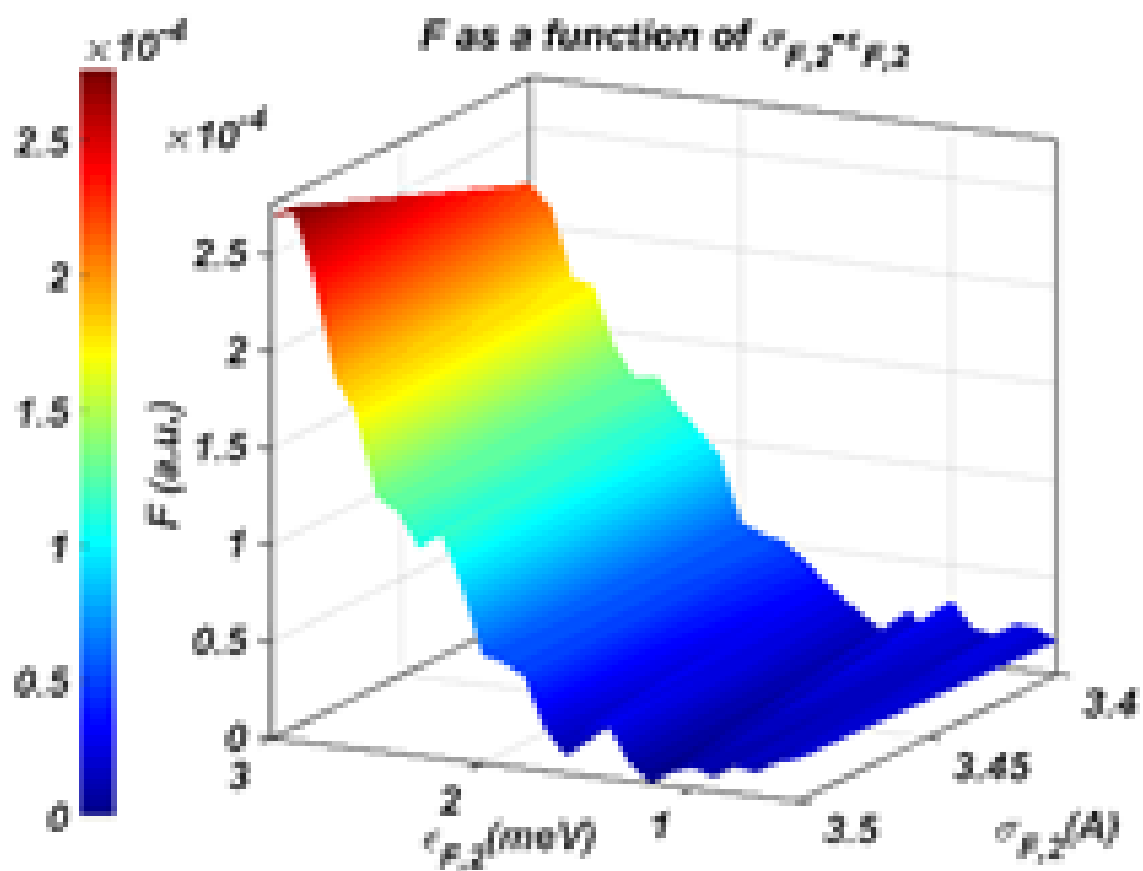


Figure 5.13. Mapped Surface of Fluorine of the second iteration in the interest region

**Third round of iteration** Since the elements oxygen, nitrogen and fluorine have very limited influence on the calculation of function  $F$ , here only the calculation of carbon and hydrogen were conducted as they still make considerable influence. Fig. 5.14 and Fig 5.15 shows the optimization function  $F$  as a function of the L-J parameters for Carbon and Hydrogen where a very small shift is again observed in the well-depth. The final parameters determined would be  $\epsilon_{C3} = 4.65meV$  and  $\sigma_{C3} = 3.5$  for carbon while  $\epsilon_{H3} = 3meV$  and  $\sigma_{H3} = 2.3$  for hydrogen. The final L-J parameters resulting from the optimization are portrayed in Table II in comparison to the initial parameters. Here what is interesting to notice is that except for hydrogen, none of the intercepts have been modified significantly. Nevertheless, the intercept for hydrogen atom used as the reference is obviously too small for  $N_2-H$  pair. Unlike the intercept, the values of well-depth for all elements had increased significantly. Although the change of well-depth might perform respectively small influence on the collision cross section, the great discrepancy indicate those values will play an important role on the optimization calculation. Besides, it might imply some of the effects of the ion-quadrupole potential have already been embedded into the potential wells. Table II also shows the expected Lennard Jones parameters using Lorentz-Berthelot [72, 73] rules of combination and regular Molecular Dynamics L-J pairs. The CCS optimized parameters are somewhat in agreement with those generally used in other fields.

### 5.1.2 Optimization Starting With Hydrogen

All the iteration conducted above use carbon as the starting element. The values obtained are the selection from a series of solutions, which indicate the parameters optimized are not unambiguously defined. There exists the possibility that optimizing the atoms L-J pairs in a different order could provide more weight to some atoms in detriment of others while not seeing substantial differences in the CCSs. Therefore, in order to get more reliable results, a new routine of optimization starting from hydrogen was designed. The order will be hydrogen followed by carbon, oxygen, nitrogen

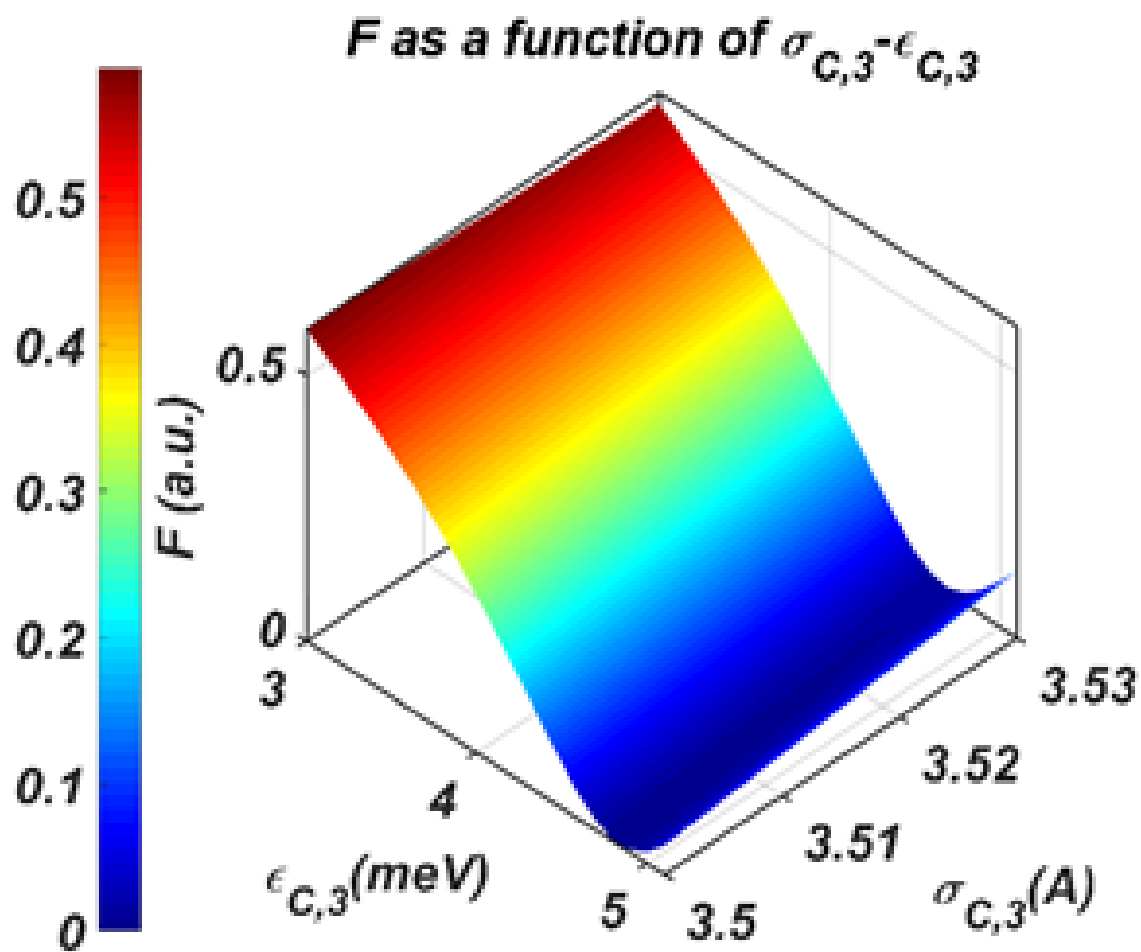


Figure 5.14. Mapped Surface of Carbon of the third iteration in the interest region

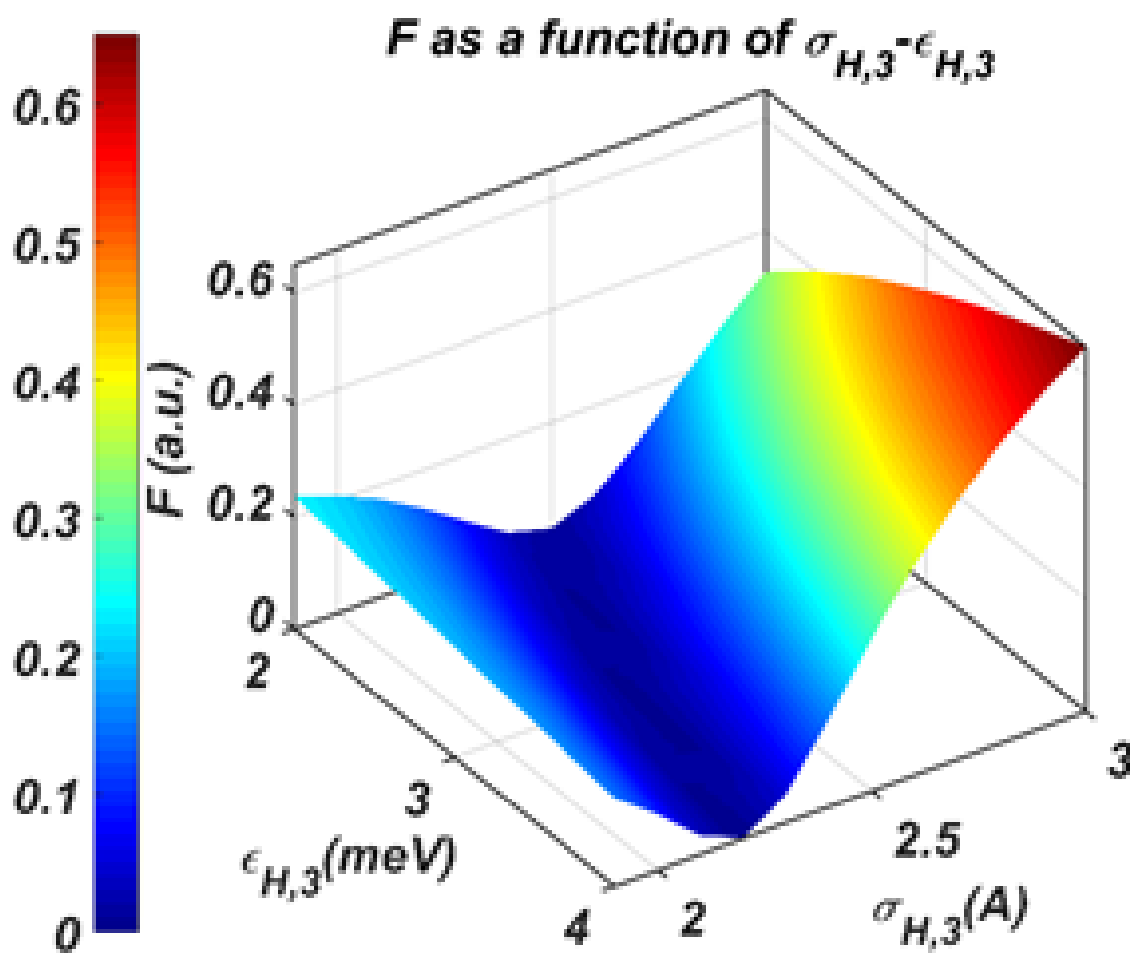


Figure 5.15. Mapped Surface of Hydrogen of the third iteration in the interest region

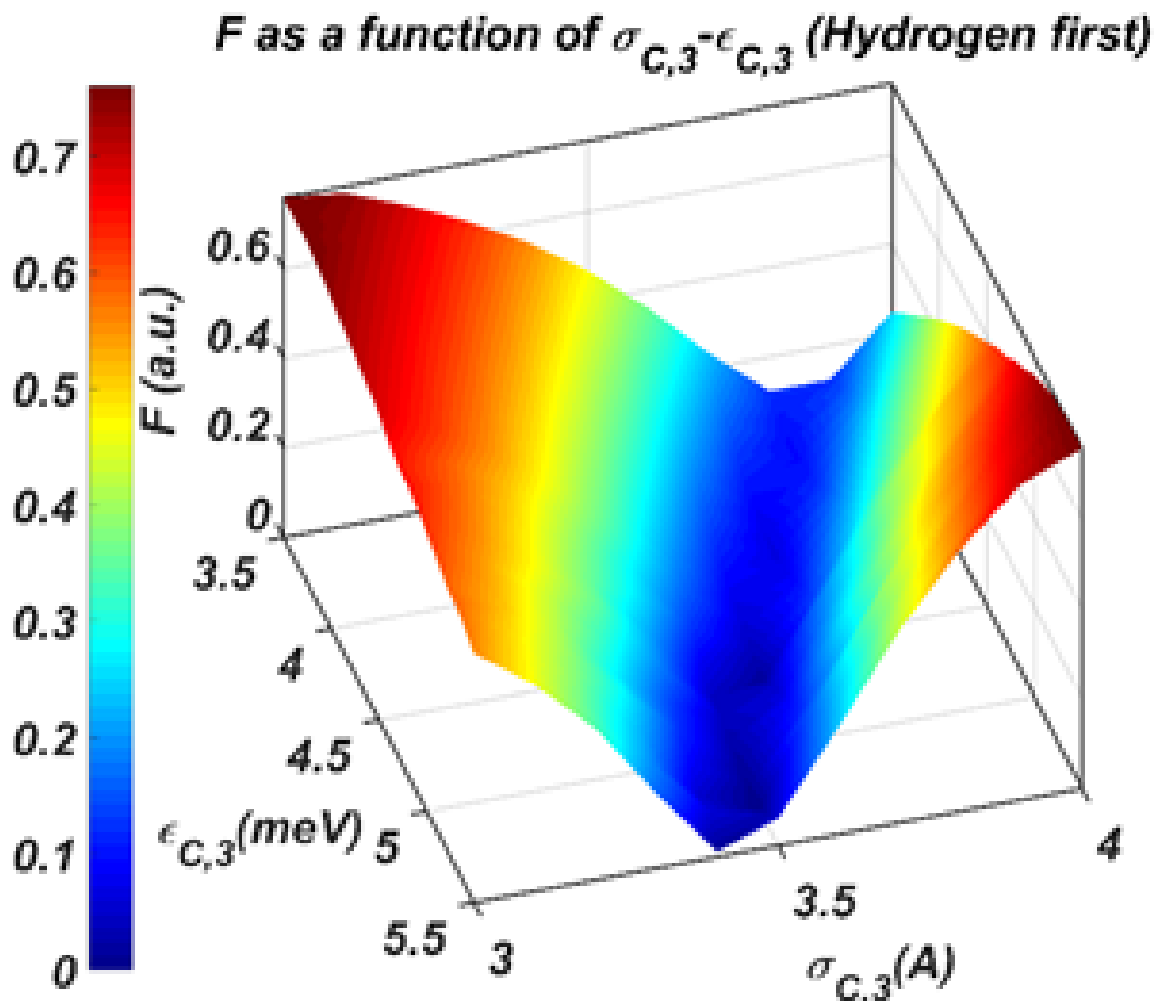


Figure 5.16. Mapped Surface of Carbon of the third iteration in the interest region (Starting with Hydrogen)

and fluorine. The results are shown in Fig. 5.16 and Fig. 5.17 for the elements with the largest weight, Carbon and Hydrogen, after 3 iterations. The Lennard-Jones parameters are slightly different from those previously obtained yielding  $\epsilon_{C3} = 4.1meV$  and  $\sigma_{C3} = 3.6$  for carbon and  $\epsilon_{H3} = 3.3meV$  and  $\sigma_{H3} = 2.2$  for hydrogen. While no significant change for the other elements. The results can be observed in the following table.

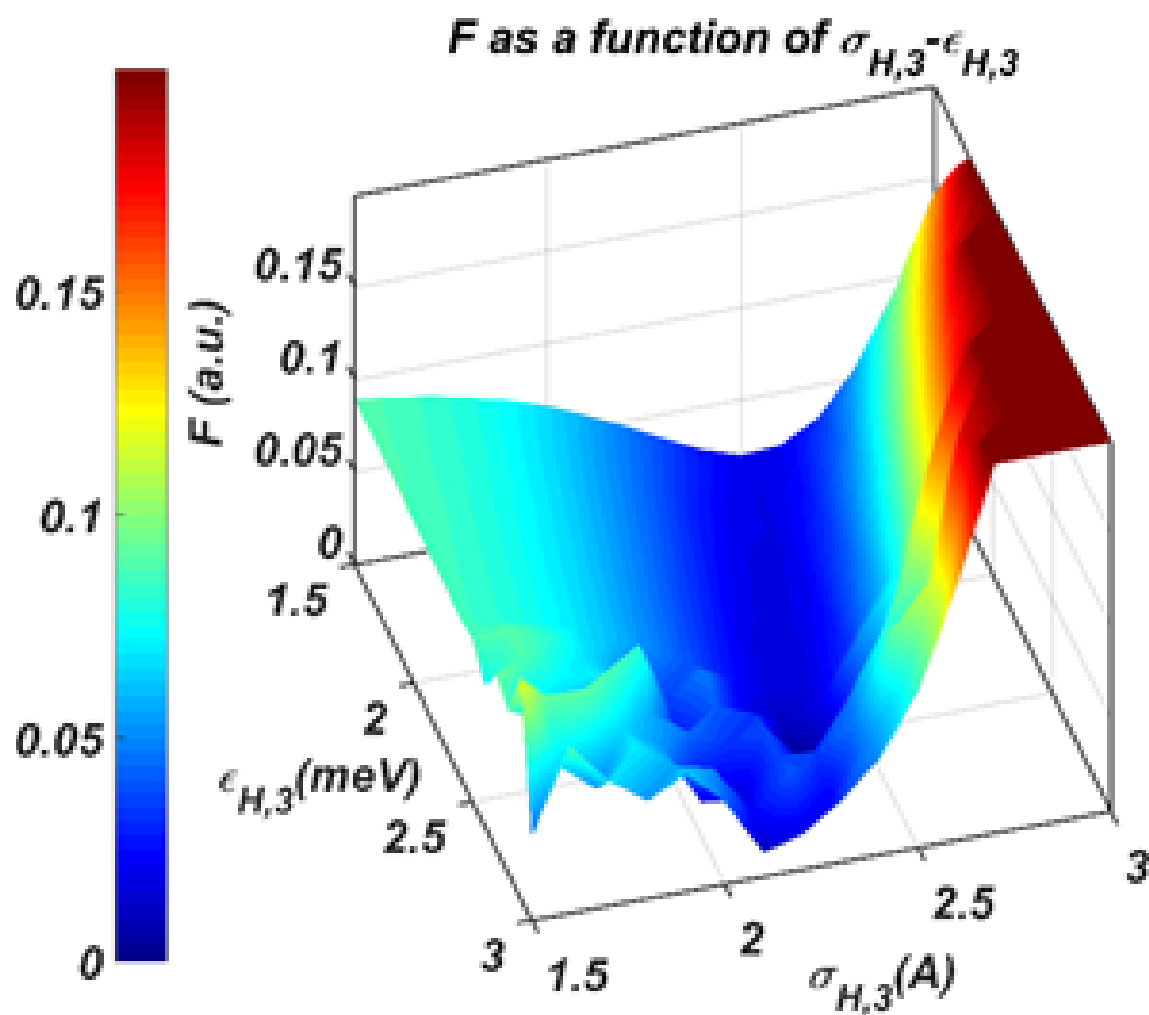


Figure 5.17. Mapped Surface of Hydrogen of the third iteration in the interest region (Starting with Hydrogen)

<b>L-J</b>	<b><i>Previous<sup>a</sup></i></b>		<b><i>Opt.<sup>1</sup></i></b>		<b><i>Opt.<sup>2</sup></i></b>	
<b><i>Element pairs</i></b>	<b><i><math>\epsilon</math> (meV)</i></b>	<b><i><math>\sigma</math> (Å)</i></b>	<b><i><math>\epsilon</math> (meV)</i></b>	<b><i><math>\sigma</math> (Å)</i></b>	<b><i><math>\epsilon</math> (meV)</i></b>	<b><i><math>\sigma</math> (Å)</i></b>
<b><i>C-N<sub>2</sub></i></b>	4.2319	3.5814	4.65	3.5	4.1	3.6
<b><i>H-N<sub>2</sub></i></b>	0.8204	1.2409	3	2.3	3.3	2.2
<b><i>O-N<sub>2</sub></i></b>	2.4195	3.255	4.3	3.5	4.3	3.5
<b><i>N-N<sub>2</sub></i></b>	3.5902	4.392	5.8	4.2	5.8	4.2

Figure 5.18. Results comparison between two routine, Opt1 is the routine starting with carbon

<b>Molecule</b>	<b>Exp. CCS (Å<sup>2</sup>)</b>	<b>CCS ion- quad(Å<sup>2</sup>)</b>	<b>Error (%)</b>	<b>CCS1 (Å<sup>2</sup>)</b>	<b>Error (%)</b>	<b>CCS2 (Å<sup>2</sup>)</b>	<b>Error (%)</b>
<i>Triphenylene</i>	143.30	149.20	4.12	145.87	1.79	144.61	0.92
<i>Nethylaniline</i>	124.50	124.50	0.00	120.42	3.28	119.42	4.08
<i>Dexamethasone</i>	190.70	190.40	0.16	190.28	0.22	188.75	1.02
<i>Acetaminophen</i>	131.10	136.20	3.89	129.84	0.96	128.99	1.61
<i>Betamethasone</i>	189.60	189.40	0.11	189.32	0.15	187.51	1.10
<i>Anthracene</i>	129.60	136.20	5.09	132.28	2.07	130.86	0.97
<i>Choline</i>	115.40	115.90	0.43	114.53	0.75	113.27	1.85
<i>Phenanthrene</i>	129.10	135.70	5.11	131.69	2.00	130.32	0.95
<i>Acetylcholine</i>	127.80	128.00	0.16	128.54	0.58	127.13	0.52
<i>c60</i>	213.10	212.90	0.09	213.61	0.24	214.35	0.59
<i>c70</i>	231.40	229.80	0.69	230.81	0.25	231.43	0.01
<i>Naphtalene</i>	115.80	121.10	4.58	116.28	0.42	114.97	0.72
<i>Paracetamol2</i>	131.10	136.20	3.89	130.63	0.36	130.09	0.77
<i>Pyrene</i>	135.00	139.90	3.63	136.88	1.39	135.77	0.57
<i>TEA</i>	122.20	122.20	0.00	122.75	0.45	120.75	1.18
<i>TMA</i>	107.40	107.20	0.19	104.06	3.11	102.79	4.30
<b>Error Avg(%)</b>			<b>2.01</b>		<b>1.13</b>		<b>1.32</b>

Figure 5.19. The comparison of the result after the primary optimization

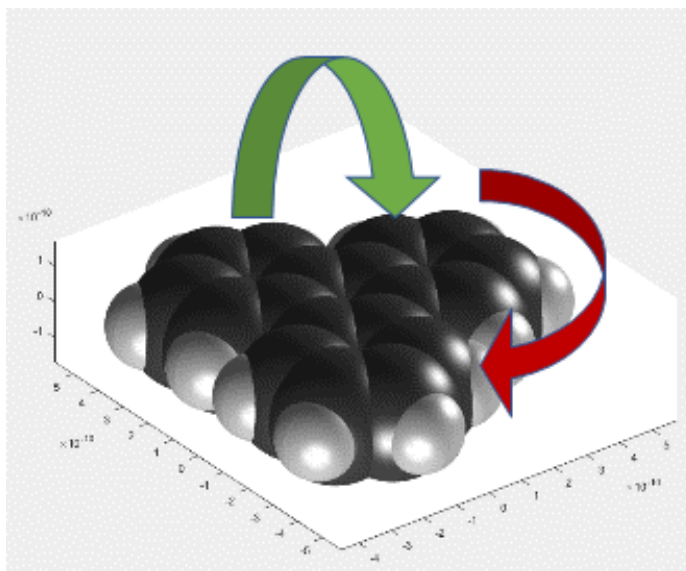


Figure 5.20. The structure of the molecule selected for the simulation: triphenylene, it can be easily noticed that the rotation of the molecule will have a great influence on the dipole moment

## 5.2 Variable Velocity Simulation

The velocity of the molecules in the drift flow were recorded corresponding to time. Fig. 5.21 shows the change of velocity in three directions of the target molecule without preferred orientation. It can be easily seen that the velocity in both Y direction and Z direction have an average value of approximate zero, meaning that even for some period the particle is moving laterally, the overall effect of the particle is still moving axially. Fig. 5.22 shows the rotating angle of the molecule without preferred orientation. All the rotating angles change rapidly, indicating the randomness of the motion of the particle.

Fig. 5.24 present the change of velocity of the target molecule with preferred orientation. The overall effect is still the same as previously. Fig. 5.25 shows the rotating angles in this situation. The rotation along Y and Z axis nearly disappear, while the rotation along X axis keep increasing. This shows when a preferred orientation is applied, the translational motion in other direction will be transferred to

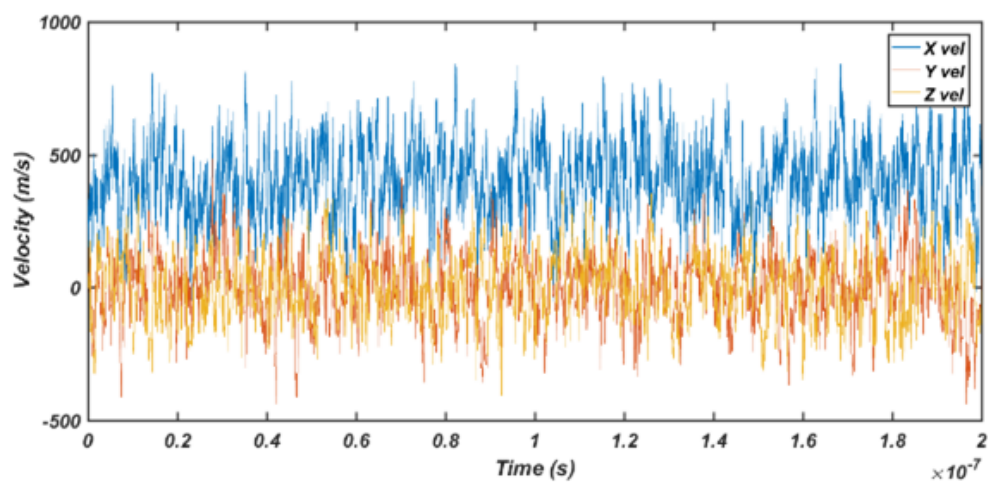


Figure 5.21. Velocity for the molecule corresponding to time, no preferred orientation

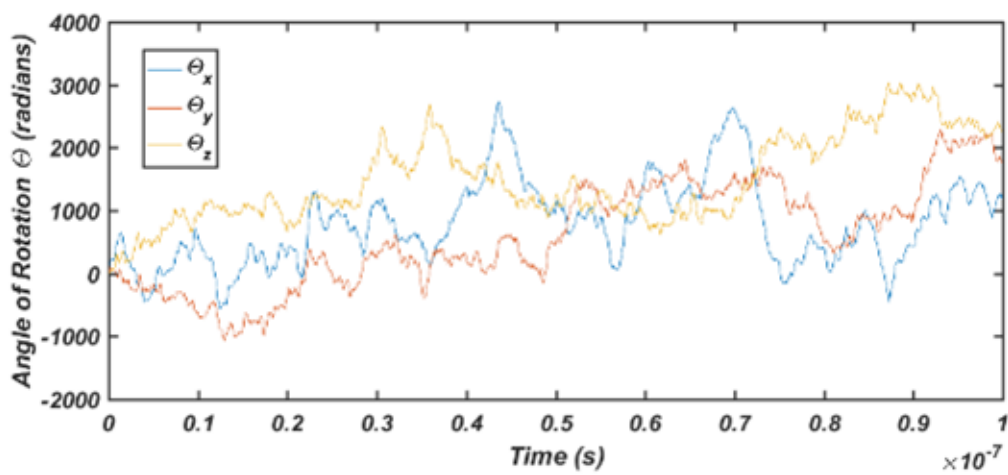


Figure 5.22. Rotating angle for the molecule corresponding to time, without preferred orientation

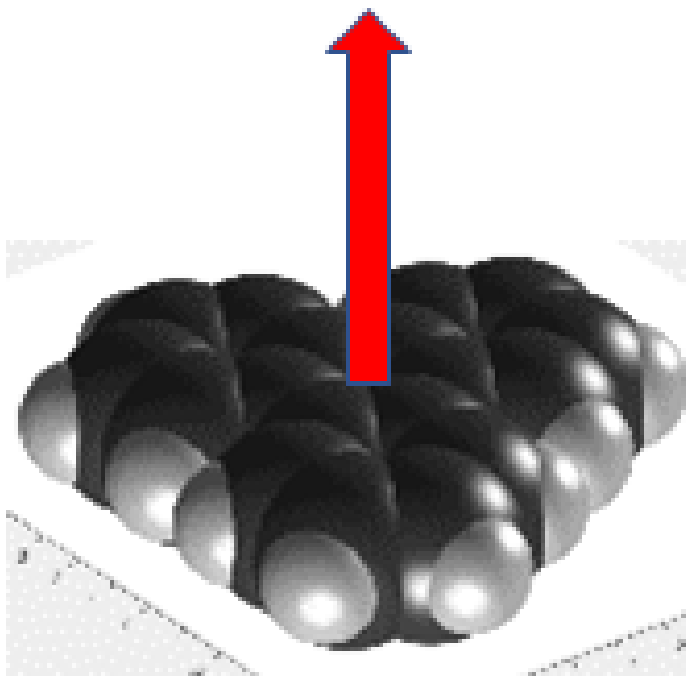


Figure 5.23. To generate single preferred orientation, a fake dipole moment was added to the triphenylene (red arrow)

the rotation along the preferred orientation. These simulation will be closely to the molecular motion in the real world.

### 5.3 Discussion

The following table shows the CCS calculations using the optimized L-J parameters for both cases studied. Using the new parameters group, the error between the calculated results and the experimental CCS will be less than 1 percent for most parts. The L-J parameters could have been further optimized (e.g. to 4-digit accuracy), yielding slightly improved results (see supplemental info for errors within 0.7percent for 5 molecules), but higher precision for this set of molecules is not guaranteed to yield better results for other molecules. If the Lennard-Jones parameters are properly optimized, the action of taking the ion-quadruple potential into the calculation explicitly to acquire approximate CCS value will not be nessary, since their

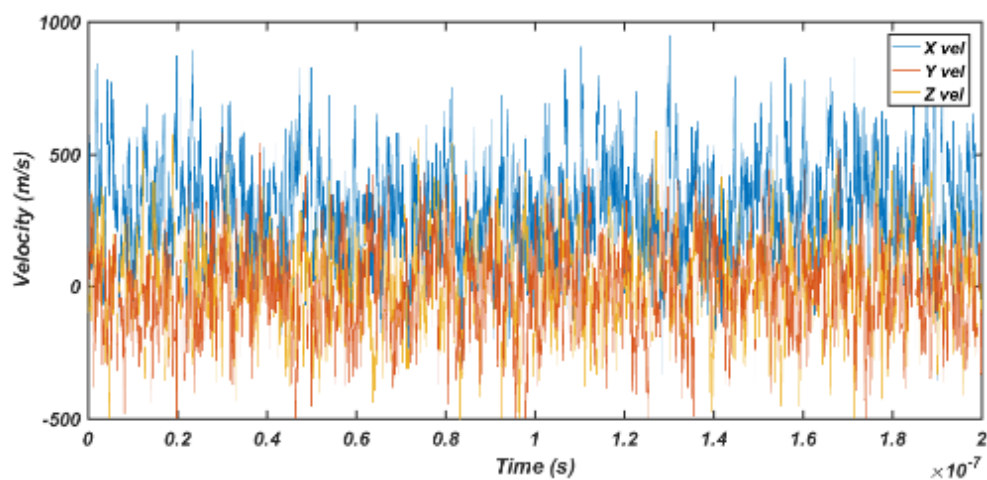


Figure 5.24. Velocity for the molecule corresponding to time, with preferred orientation

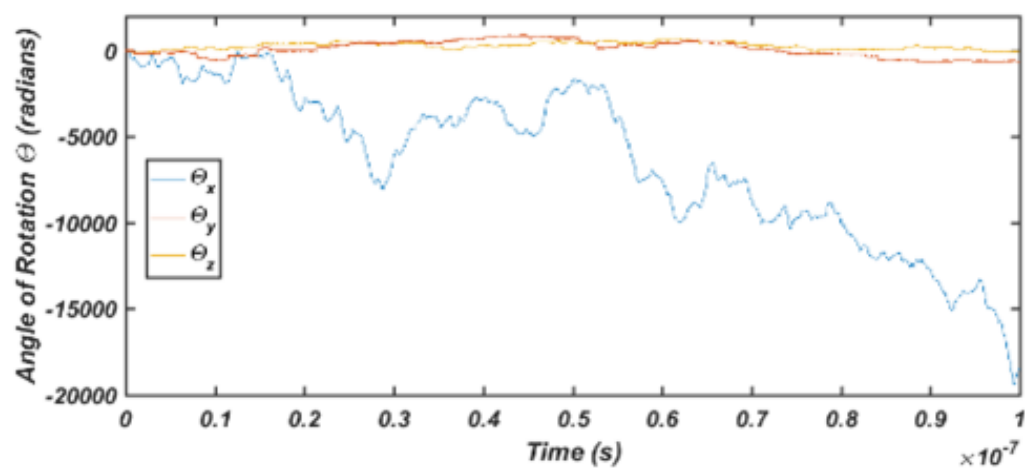


Figure 5.25. Rotating angle for the molecule corresponding to time, with preferred orientation

influences have already been concluded in the major two parameters. The addition of the ion-quadruple potential provides no gain in accuracy while greatly increasing computational time. Be careful that the effects of ion-quadruple potentials do exist. Just because other parameters will contain its influence on the CCS calculation. However, some of these effects can be embedded into L-J potentials without significant errors in the CCS calculations under most circumstances. Other effects such as the CCS differences arising from planar Polyaromatic Hydrocarbon structures encountered by Campuzano et al. [74] have disappeared when the L-J potentials are optimized in this way. Since there is not enough information of how the parameters were optimized in their work, it is difficult to fully assess the reason for such discrepancy. There is reason to believe that very planar molecules could have some preferred alignment, but this effect could not be characterized with the existing calculation methods which assume all orientations are equally probable.

## 6. RESULTS OF THE TNT DETECTION

### 6.1 Selection of Concentration of Charging Solution

In the beginning test the DMA potential is determined as -1060 volts, in the following test the potential of DMA will keep this value.

The results of the TNT test using charging solution with various concentration are exhibited. It is apparently 30 mM, 23 mM, 15 mM are all providing clear signal of TNT molecules. Even when the concentration of ammonium acetate lower down to 15 mM, the peak of TNT molecule (227) still has the strongest intensity. Therefore 30 mM, 23 mM and 15 mM of ammonium acetate are all workable for the test, showed in Fig. 6.1 - Fig. 6.3. When the concentration of ammonium acetate comes to 8 mM, no any signal is collected.(Fig. 6.4) Therefore, 15 mM of charging solution is selected for the next test.

### 6.2 TNT in Vaporized Solution

The following figures show the test results of the TNT from vaporized solutions of different concentration. Fig. 6.5 shows the result of  $\mu\text{g}/\text{ml}$ . The intensity of the TNT here is strong, only the value of  $m/z$  become around 226. The possible reason is that with the complicated collision happened in front of the DMA, the TNT molecule lost one hydrogen atom and become  $(\text{TNT} - \text{H})^-$ . This happened to 16  $\mu\text{g}/\text{ml}$  too.(Fig 6.8). For TNT solution of 48 $\mu\text{g}/\text{ml}$ , the peak of TNT return to 227 again, but the 211 peak become 210.(Fig. 6.6) For the 32 $\mu\text{g}/\text{ml}$ , peak of 227 and 210 exist, but both of them are relatively weak. The strongest peak is around 146, which can be an impurity.(Fig.6.7) However, since the peak of 146 appears in both spectra of 48 $\mu\text{g}/\text{ml}$  and 16 $\mu\text{g}/\text{ml}$  solution, and get a weaker pick in the latter one, it also has the possibility to be an unusual fragment of TNT.

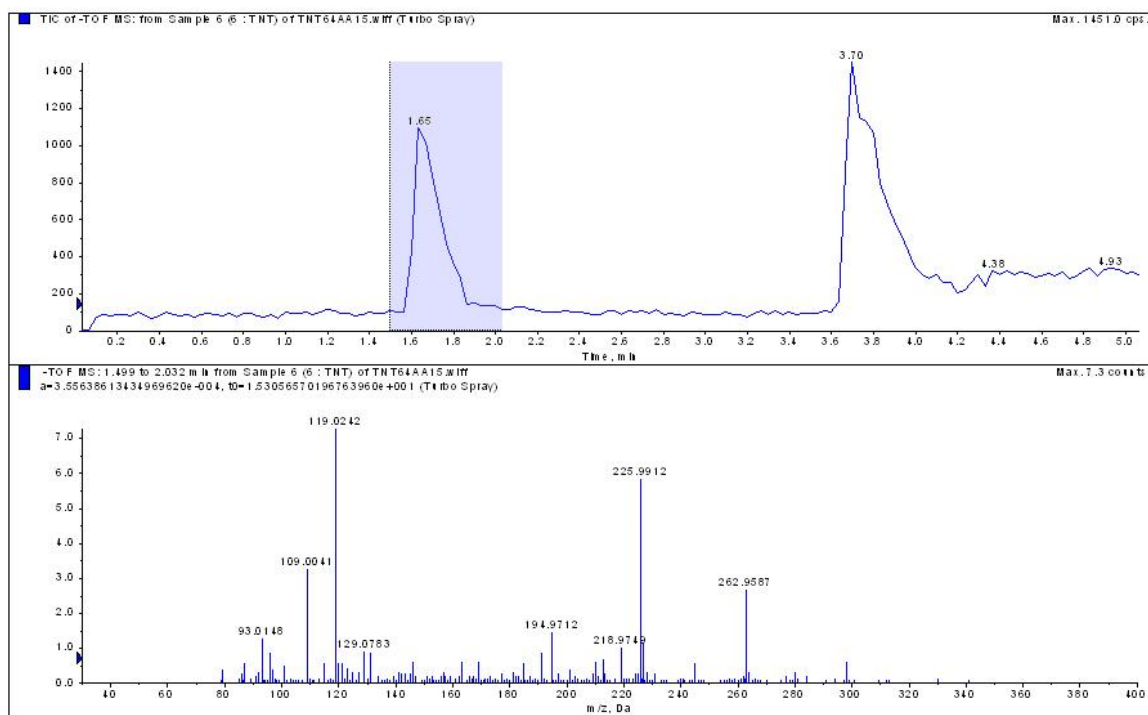


Figure 6.1. Spectrum of TNT using 30 mM ammonium acetate

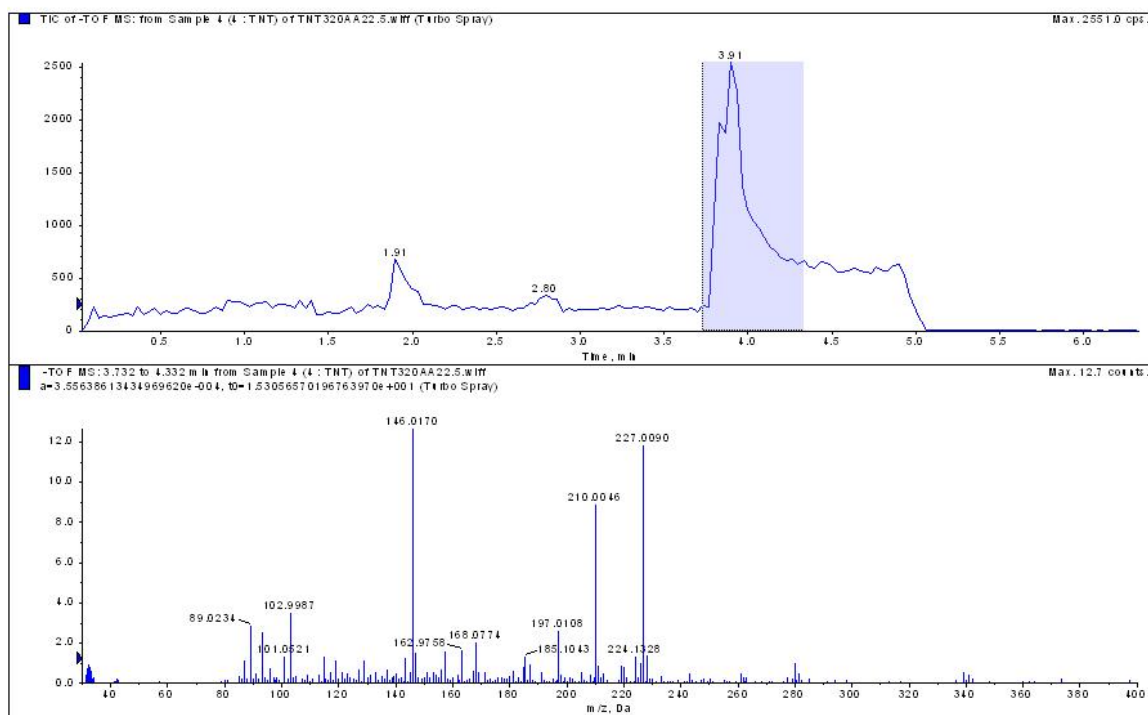


Figure 6.2. Spectrum of TNT using 23 mM ammonium acetate

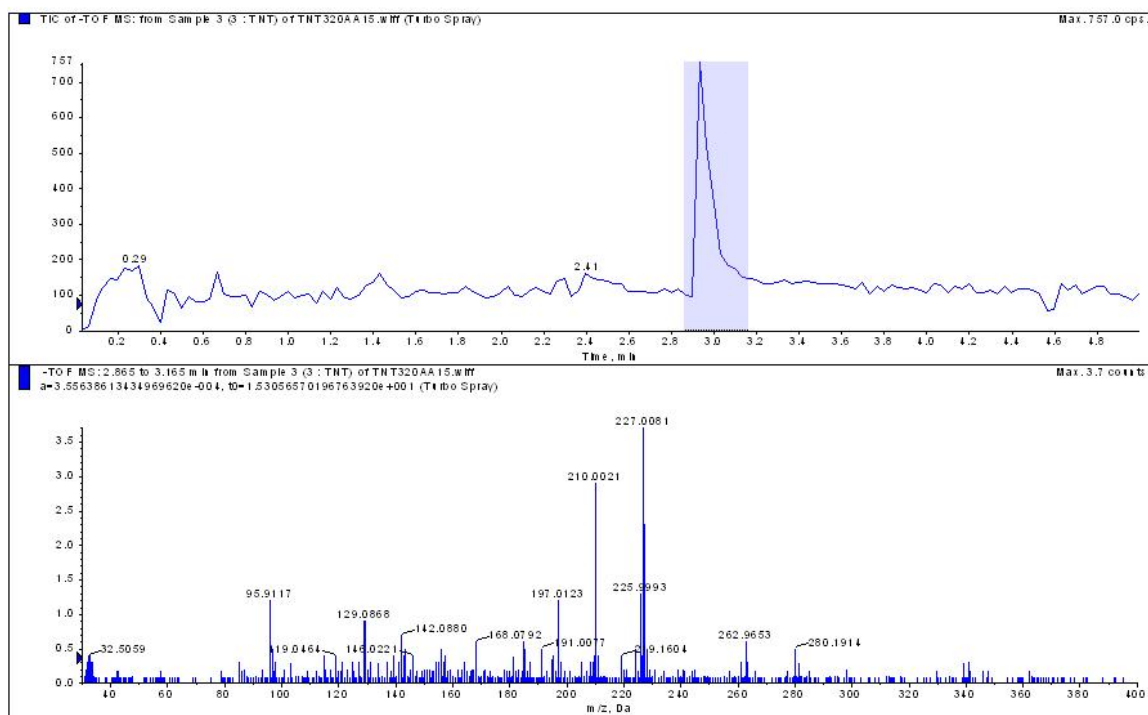


Figure 6.3. Spectrum of TNT using 15 mM ammonium acetate

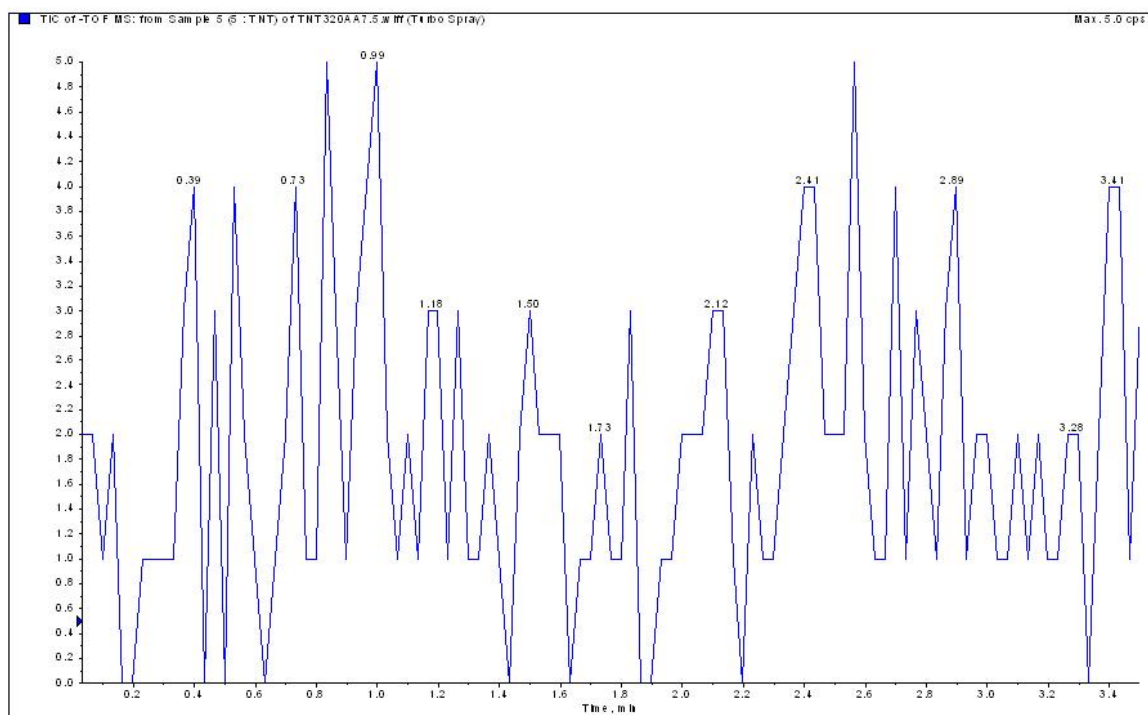


Figure 6.4. Spectrum of TNT using 8 mM ammonium acetate

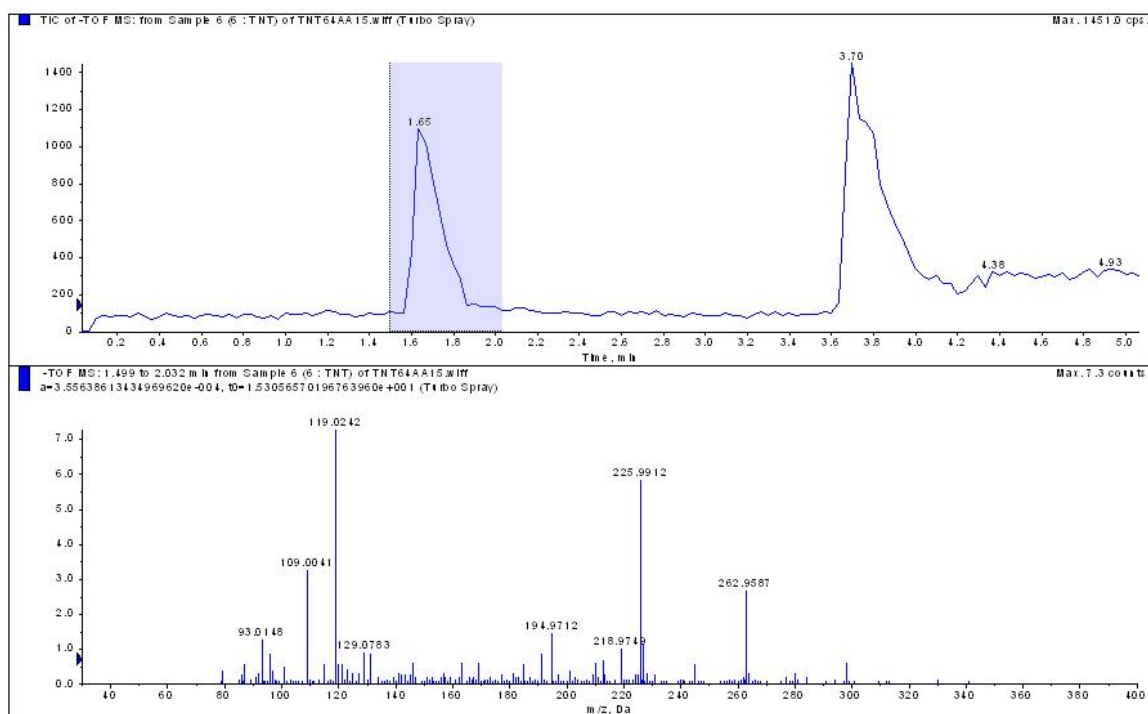


Figure 6.5. Spectrum of TNT using 64  $\mu\text{g}/\text{ml}$  of TNT

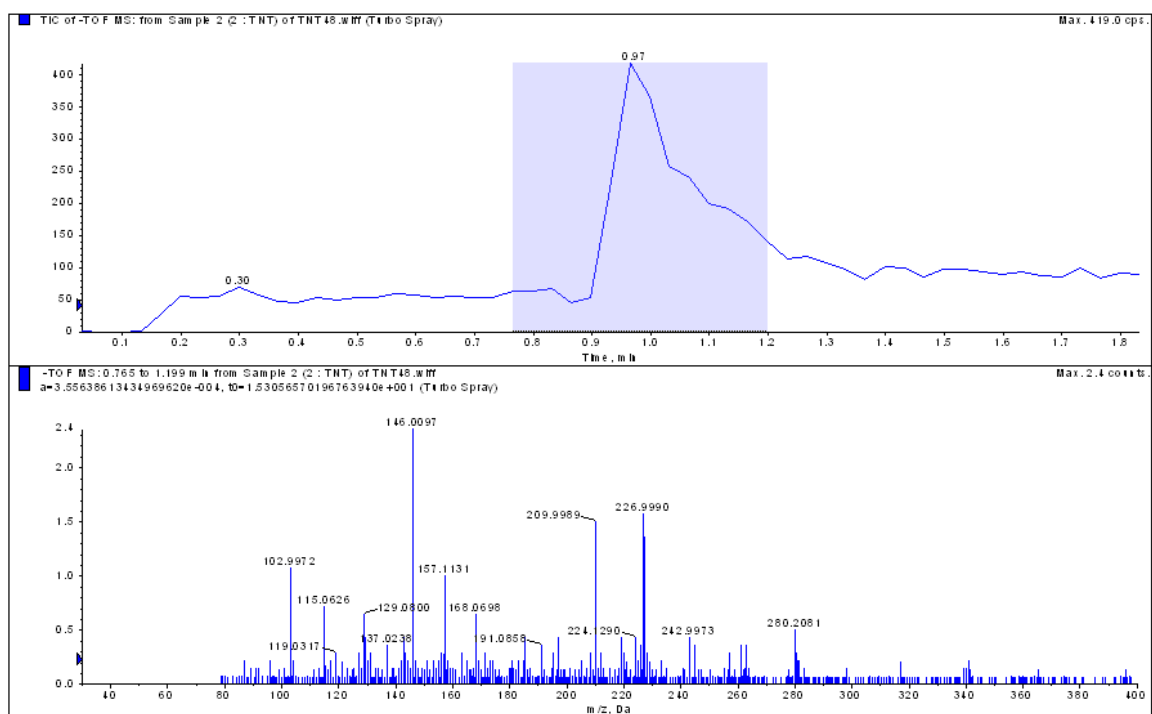


Figure 6.6. Spectrum of TNT using 48  $\mu\text{g}/\text{ml}$  of TNT

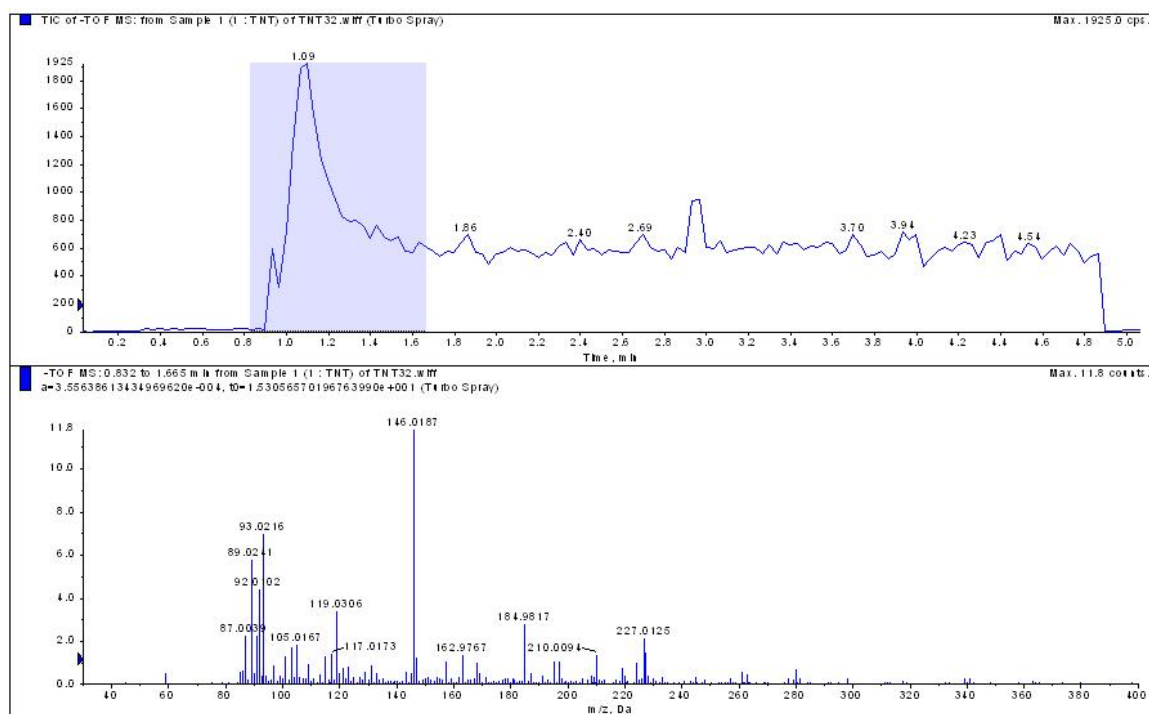


Figure 6.7. Spectrum of TNT using 32  $\mu\text{g}/\text{ml}$  of TNT

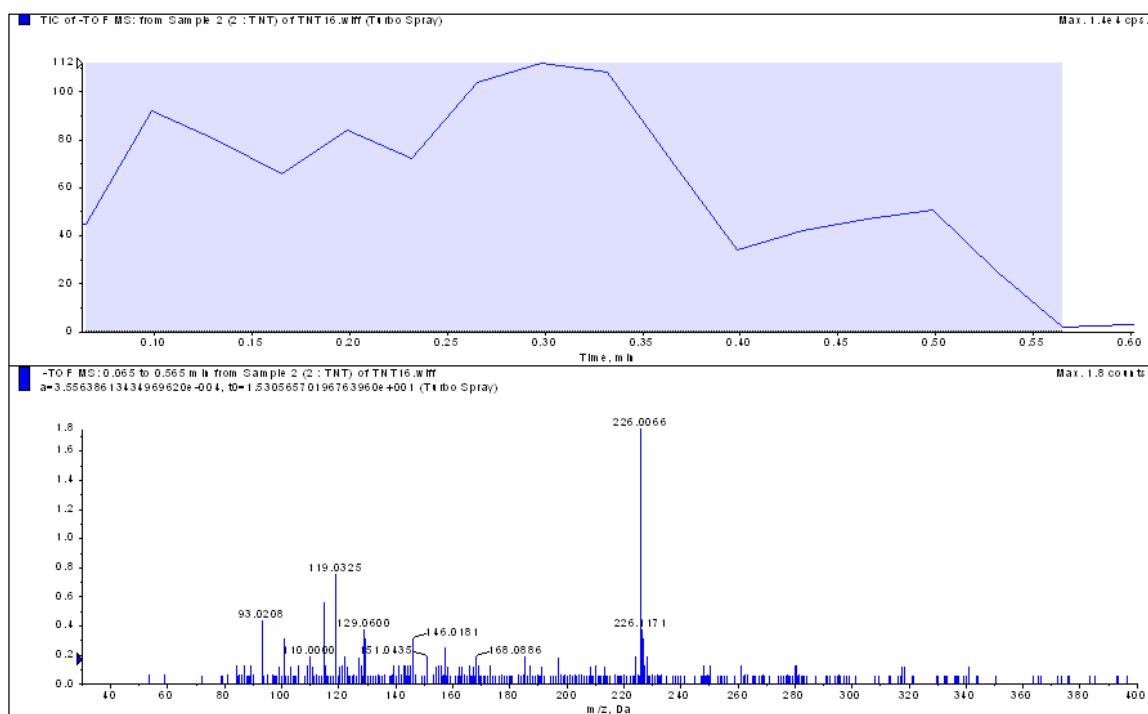


Figure 6.8. Spectrum of TNT using 16  $\mu\text{g}/\text{ml}$  of TNT

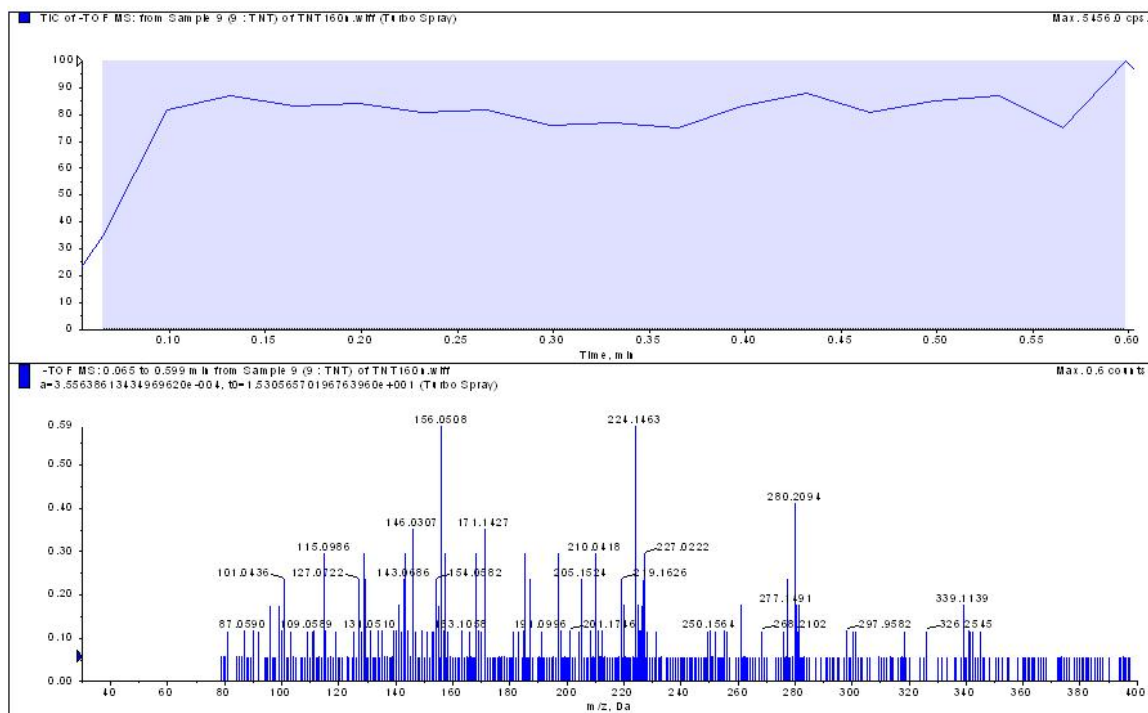


Figure 6.9. Spectrum of TNT using 160 ng/ml of TNT

When the concentration of TNT comes as low as 160 ng/ml, the signal of every substance is too weak to be considered as valuable. Thus, we can consider the limitation of this experiment is reached.

### 6.3 TNT from Enclosed Environment

All the results is showed in the following. Fig 6.10 - Fig. 6.15 show the results at 120 C, Fig. 6.16 - Fig. 6.21 show the results at 150 C, Fig. 6.22 - Fig. 6.27 show the results at 180 C. Firstly, all the spectra show various peaks of different mass-to-charge ratio. This might be caused by the complicated reactions happen within the DMA.

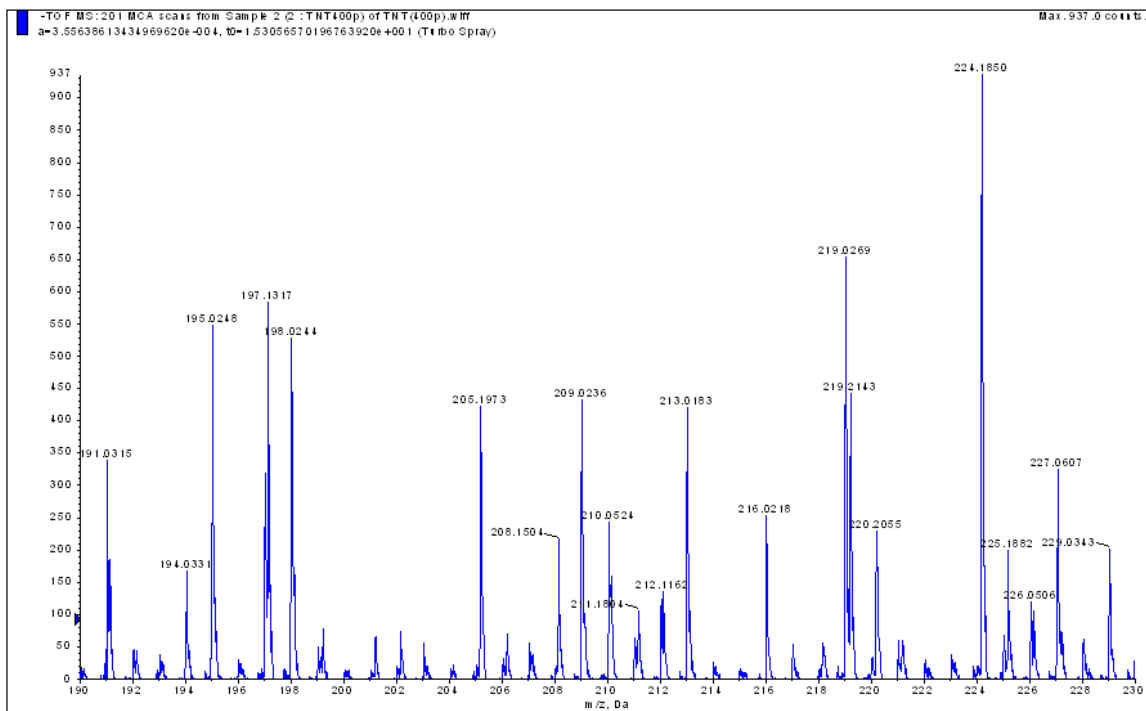


Figure 6.10. Spectrum of TNT using 400 pg/ml of TNT at 120 C

Considering the various peak obtained in the previous test, the peaks with values of 196, 197, 198, 209, 210, 211, 226, 227, 228 are collected, the values of counts are listed in Fig. 6.28, Fig. 6.29 and Fig. 6.30 for 120 C, 150 C and 180 C correspondingly. The total number of counts of 9 peaks and for major peaks (197, 210, 227) are calculated.

Under 120 C, the peaks do not have a very strong intensity. When using TNT solution of 400 pg/ml (Fig. 6.10), the top two peaks are 224 and 219. Neither of these are the targeted values. Since the quantity of TNT in the reservoir is very smaller, this phenomenon is easy to understand: other substance in the air is ionized by the ammonium acetate, and they have a larger concentration compared to the TNT input. The peak of 197 and 198 show more than 500 counts, which is already large

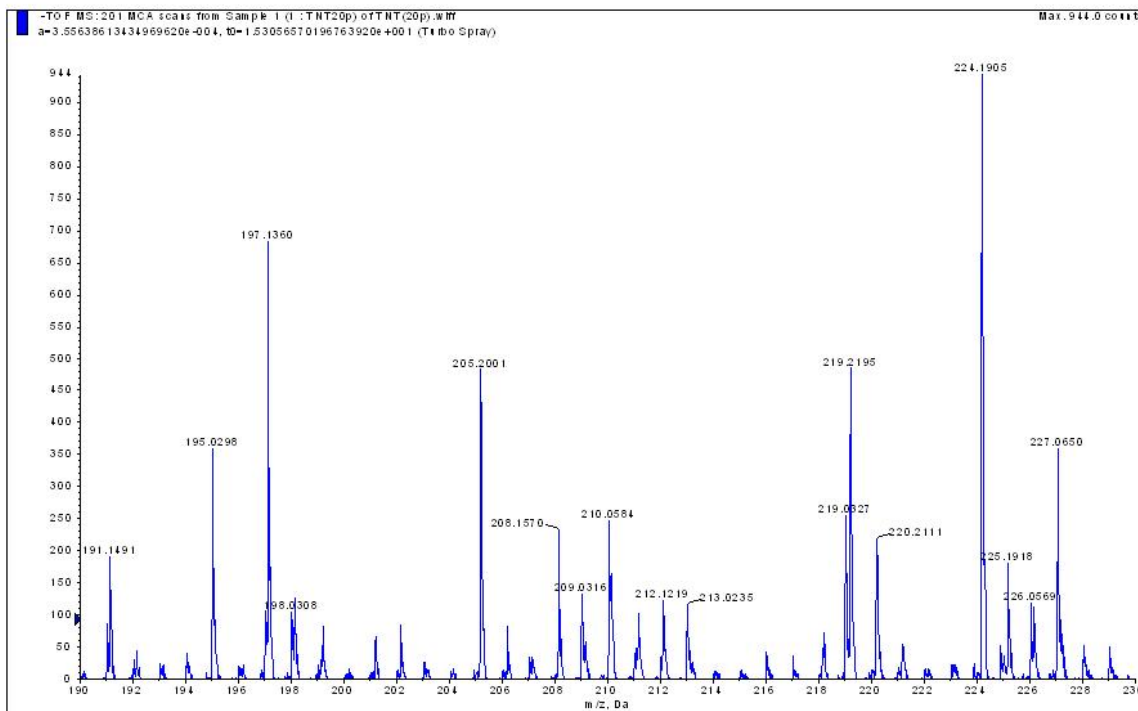


Figure 6.11. Spectrum of TNT using 20 pg/ml of TNT at 120 C

enough for a successful detection. Peak of 209 is stronger than the major targeted peak of 210, that might be caused by the ion losing one hydrogen atom due to the strong ionization.

When the concentration of TNT solution is lowered down to 20 pg/ml (Fig. 6.11), it is surprising that the intensity does not reduce a lot even the quantity of TNT put into the reservoir is only one twentieth as previous trial. The strongest peak is 224 again, and its intensity is nearly the same as the test for 400 pg/ml, which indicate the substance generates this peak is not affected by the TNT solution used. In another word, this substance comes from the environment. The intensity of peak 197 even increases, and the intensity of peak 198 decreases significantly, and the total counts

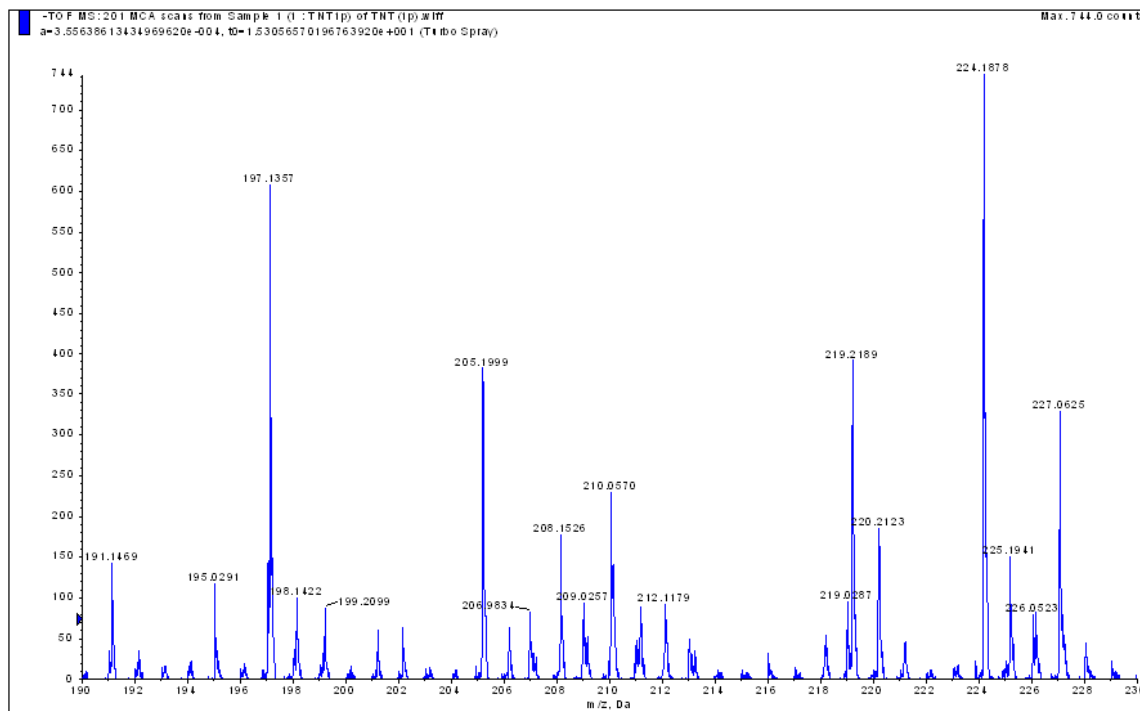


Figure 6.12. Spectrum of TNT using 1 pg/ml of TNT at 120 C

of the group of 196, 197 and 198 decreases. The total counts of all 9 selected peaks reduce to 2154 from 2563. This shows the relationship between concentration of TNT and the intensity of the signal may not be linear.

The next trial use the TNT solution of 1 pg/ml for the test (Fig. 6.12). In the mass spectrum, the strongest peak is still 224, identical as previous tests. However, the intensity of this peak reduce to less than 800 counts, which does not agree with the previous assumption. The possible reason might be that the cleaning between each test swept away the corresponding substance. The total counts of the selected 9 peaks keep reducing, from 2154 to 1668. This result agree with the previous tests: the total counts will reduce, but not linear with respect to the concentration.

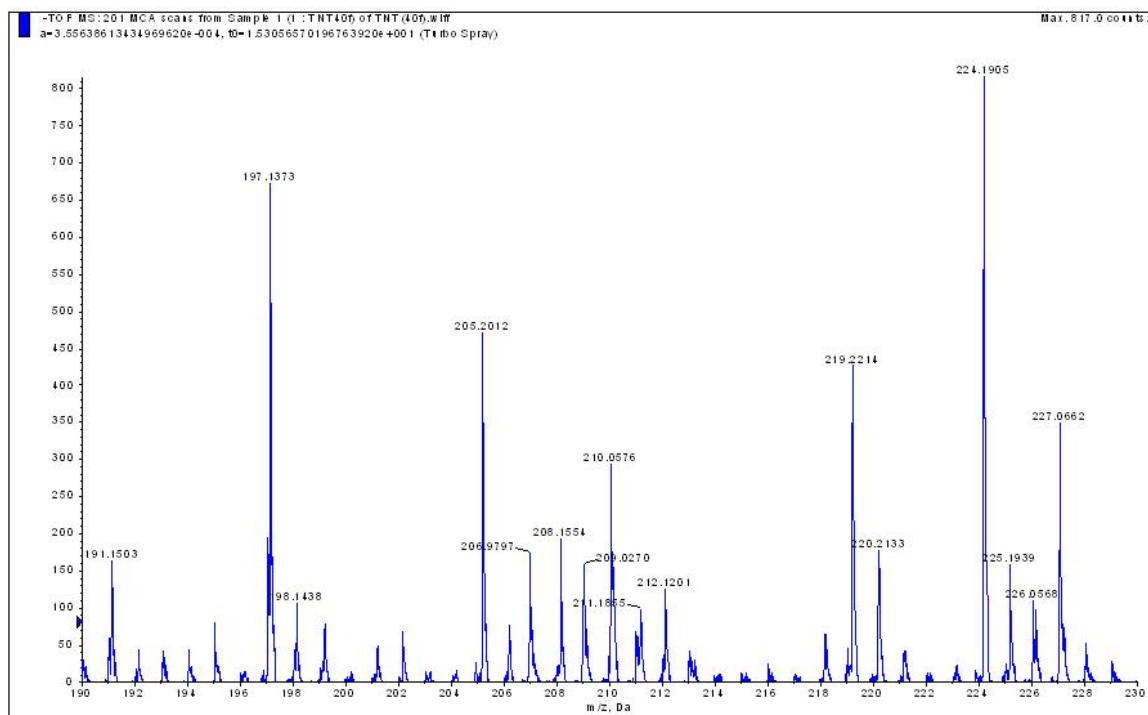


Figure 6.13. Spectrum of TNT using 40 fg/ml of TNT at 120 C

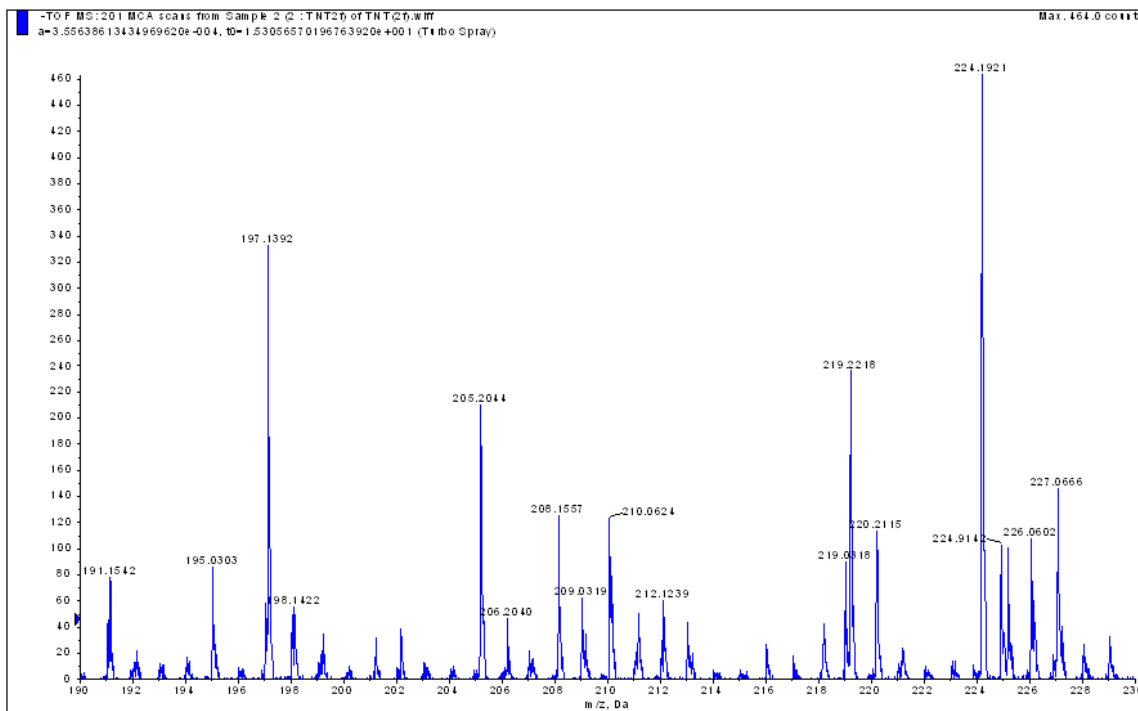


Figure 6.14. Spectrum of TNT using 2 fg/ml of TNT at 120 C

The next trial use the TNT solution of 40 fg/ml for the test (Fig. 6.13). This mass spectrum does not agree with the previous conclusion very well. The strongest peak is still 224, which is always the same. However, the intensity of the targeted peak, as well as the total counts of all the selected peaks increase. This phenomenon is abnormal. Two possible reasons may cause it: the residual TNT within the system make the signal stronger, or the solution tested is contaminated.

Then the solution with a concentration of 2fg/ml is tested (Fig. 2.14). The peak of 224 reduces significantly. However, it is still the strongest peak among the mass spectrum. The peak of 197, 198, 210, 226, 227 decrease significantly again as supposed. What is the same as previous tests is that the peaks of 196, 209 and

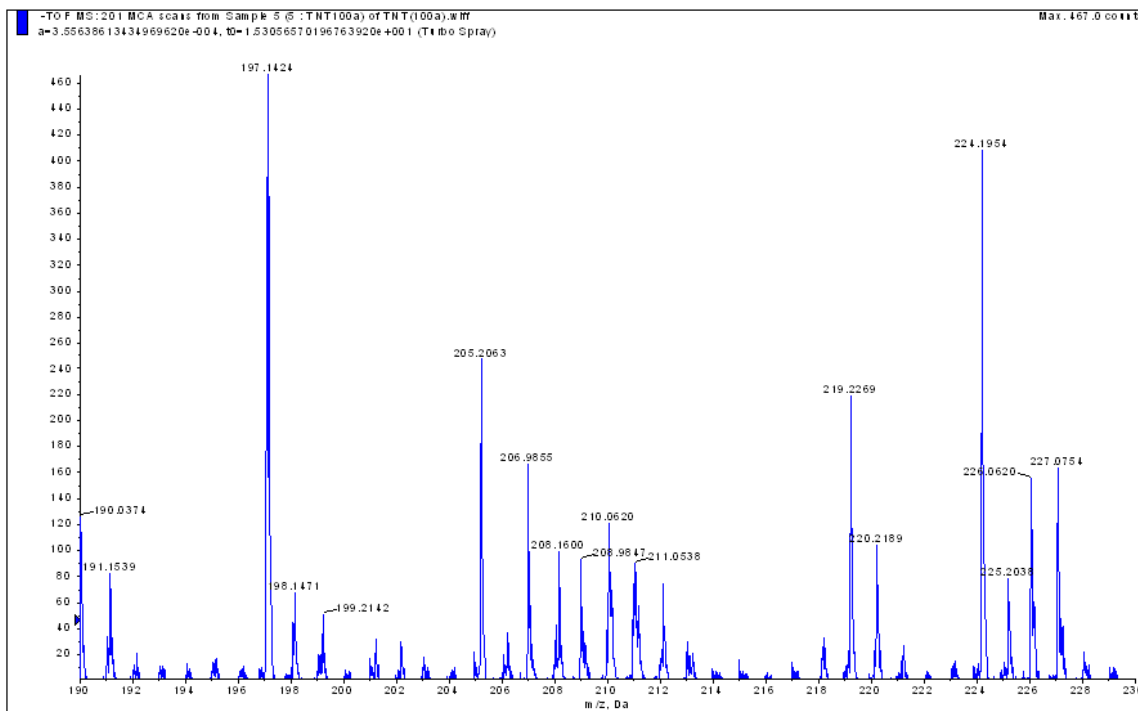


Figure 6.15. Spectrum of TNT using 100 ag/ml of TNT at 120 C

228 always have very weak influence. That might imply that these 3 peaks have no relation with TNT. However, these peaks are still decided to collect for a more comprehensive analysis. The total counts go to 1005, compared to the 500 times of concentration reduction from the test of 1 pg/ml, the reduction in counts is still small.

The last trial of tests under 120 C use the TNT solution with concentration of 100 ag/ml. The total counts reduce to 601.

Then the next group of test raise the temperature to 150 C, the results are showed in Fig. 6.16 to Fig. 6.21. All of the mass spectra shows similar rules obtained in the tests under 120 C. The intensity of the peak of 224 is still the strongest, which may make the conclusion, that this peak comes from the environment. While among

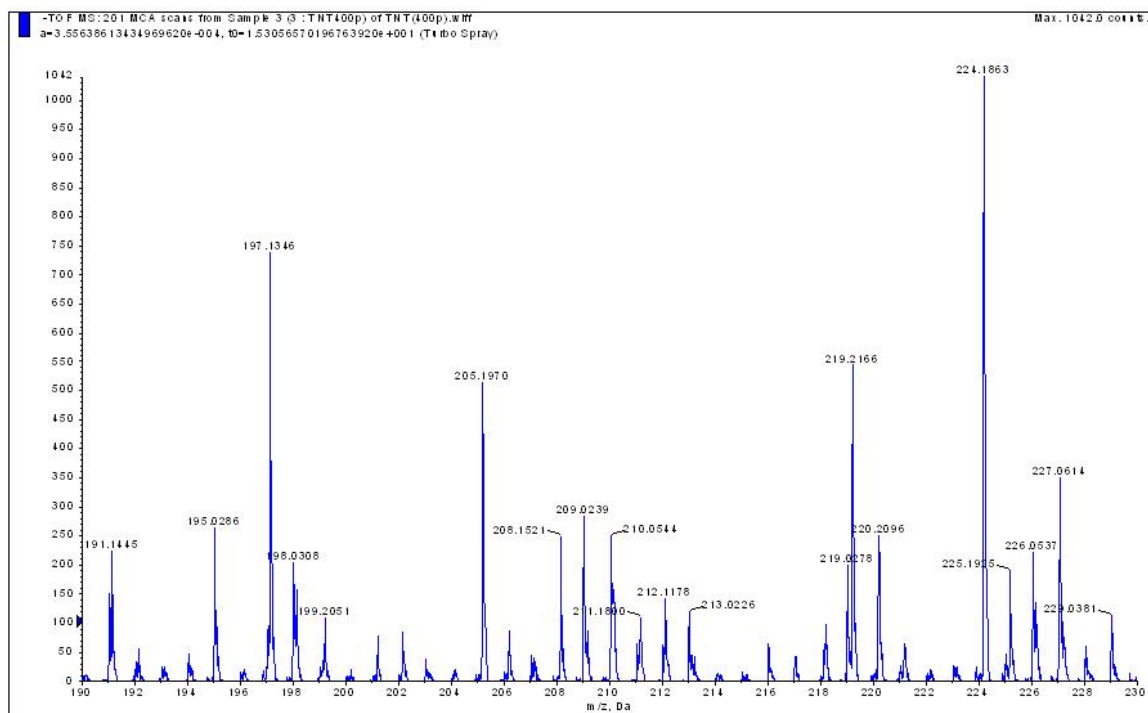


Figure 6.16. Spectrum of TNT using 400 pg/ml of TNT at 150 C

these tests the trial of 40 fg/ml agree with other trials better. Another phenomenon needs to be noticed is that almost all the number of total counts increase compared to the corresponding under 120 C. There is one exception, the trial of 40 fg/ml, which is likely caused by the abnormally strong intensity of the signal of 40 fg/ml under 120 C. The reason why more signal is collected under higher temperature might be that the acetone used to absorb TNT evaporate more when it is heated to a higher temperature. Therefore, more TNT molecules are released from the filter paper and brought to the DMA-MS system by the dry air flow.

The last group of tests is operated under 180 C (Fig. 6.22 to Fig. 6.27). Again, the intensity of peak 224 is the strongest. However, the intensity have a significant

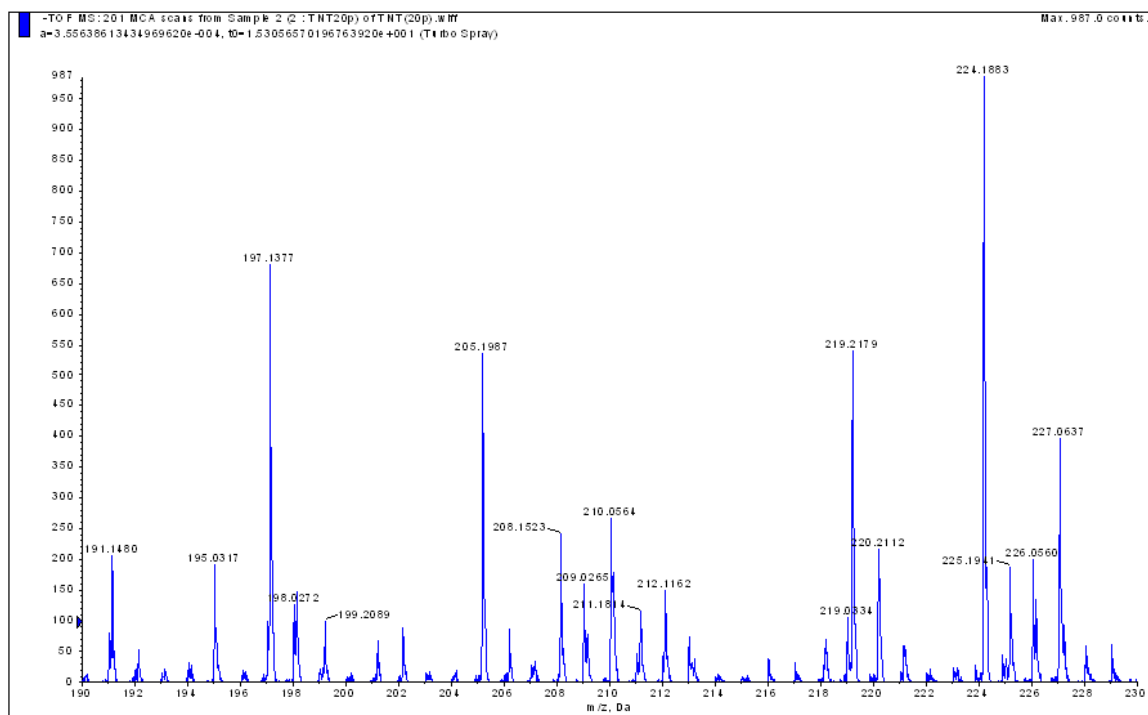


Figure 6.17. Spectrum of TNT using 20 pg/ml of TNT at 150 C

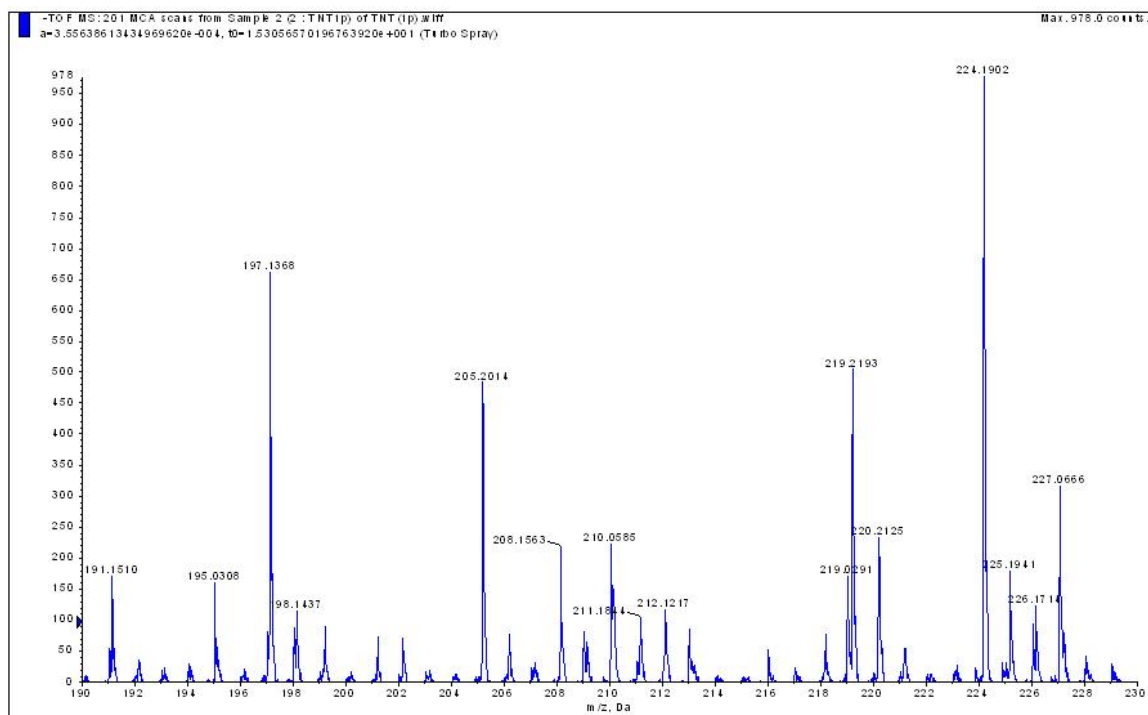


Figure 6.18. Spectrum of TNT using 1 pg/ml of TNT at 150 C

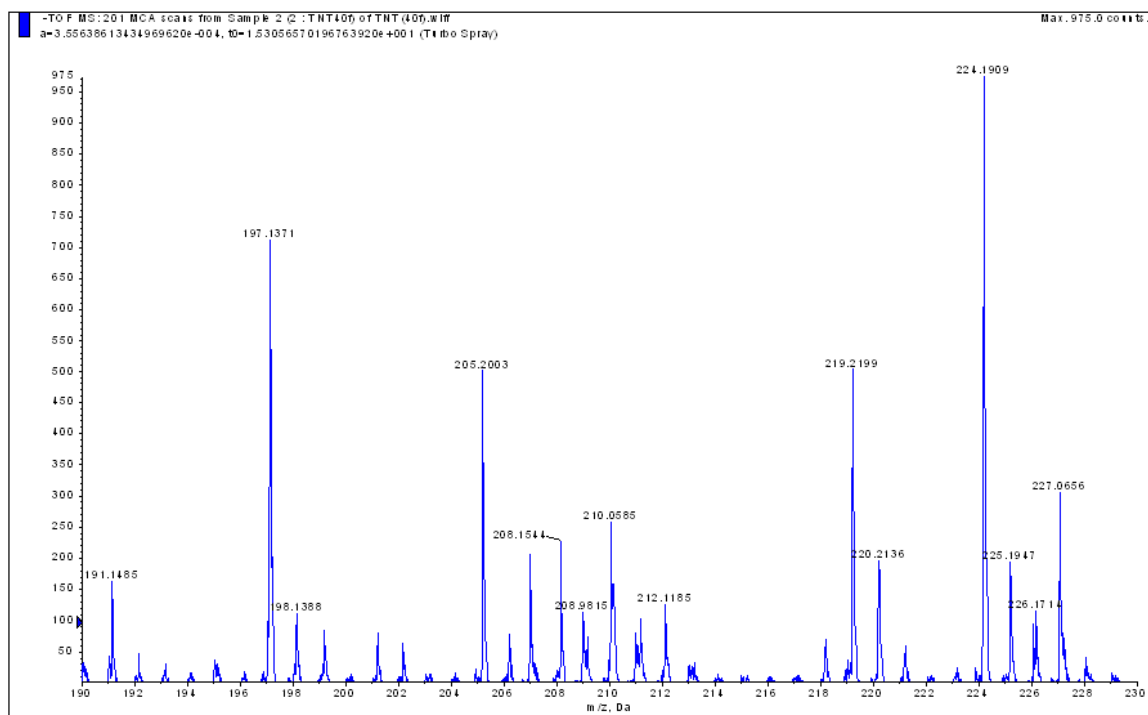


Figure 6.19. Spectrum of TNT using 40 fg/ml of TNT at 150 C

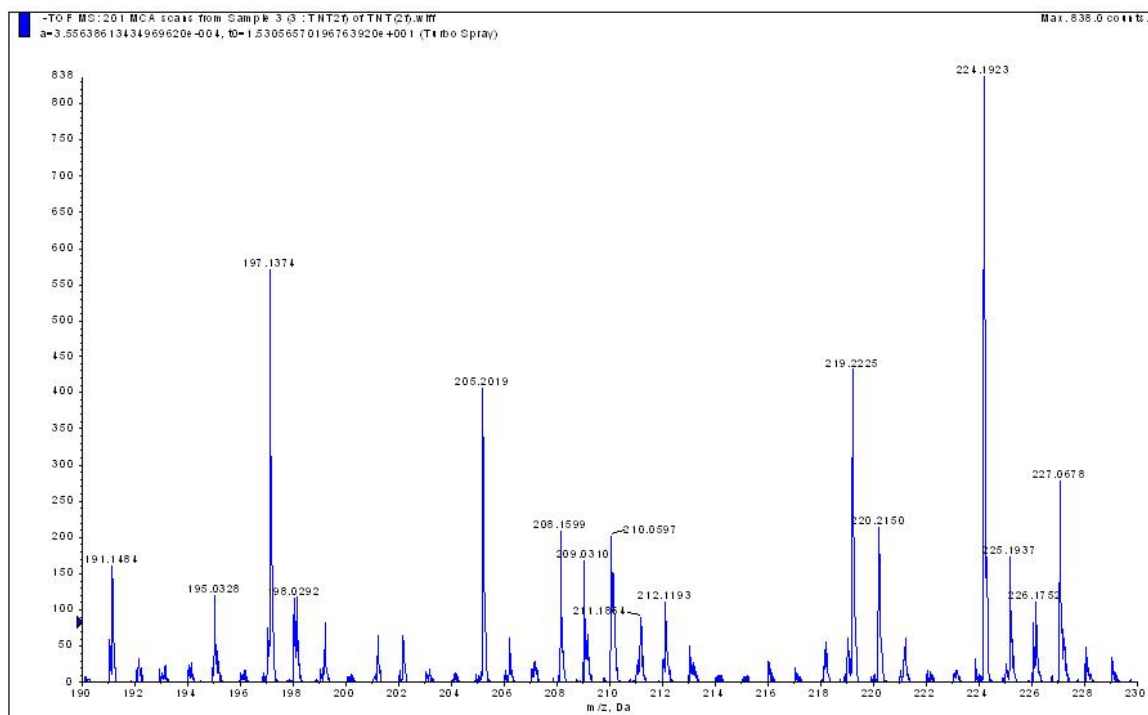


Figure 6.20. Spectrum of TNT using 2 fg/ml of TNT at 150 C

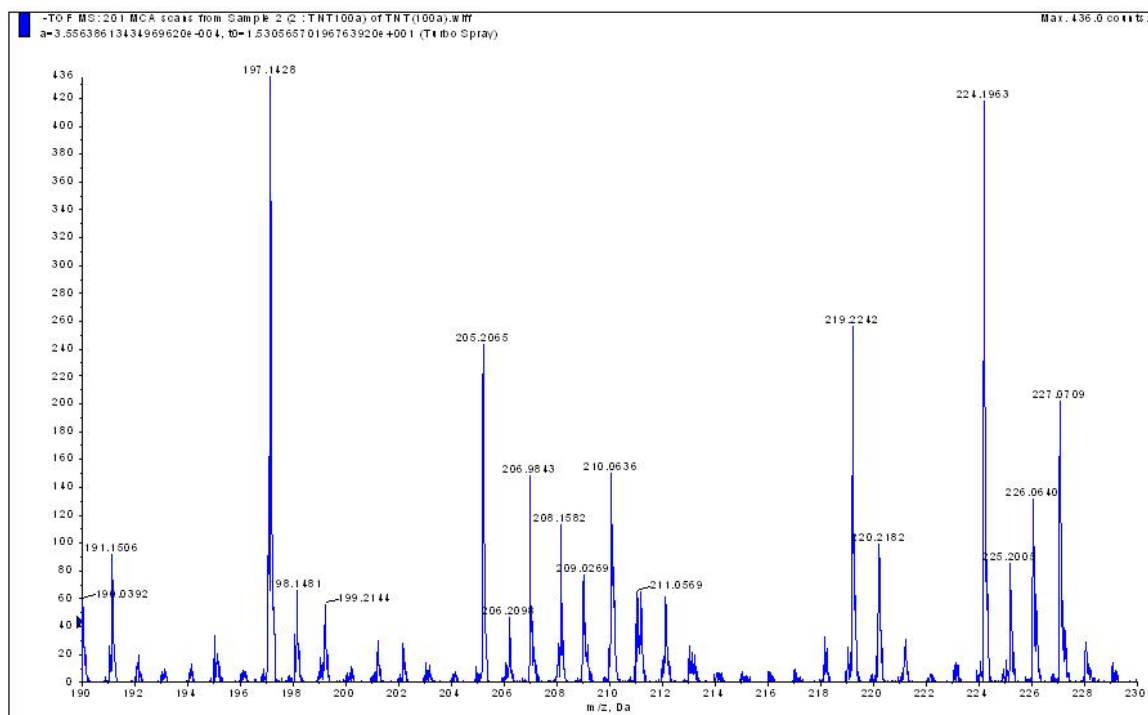


Figure 6.21. Spectrum of TNT using 100 ag/ml of TNT at 150 C

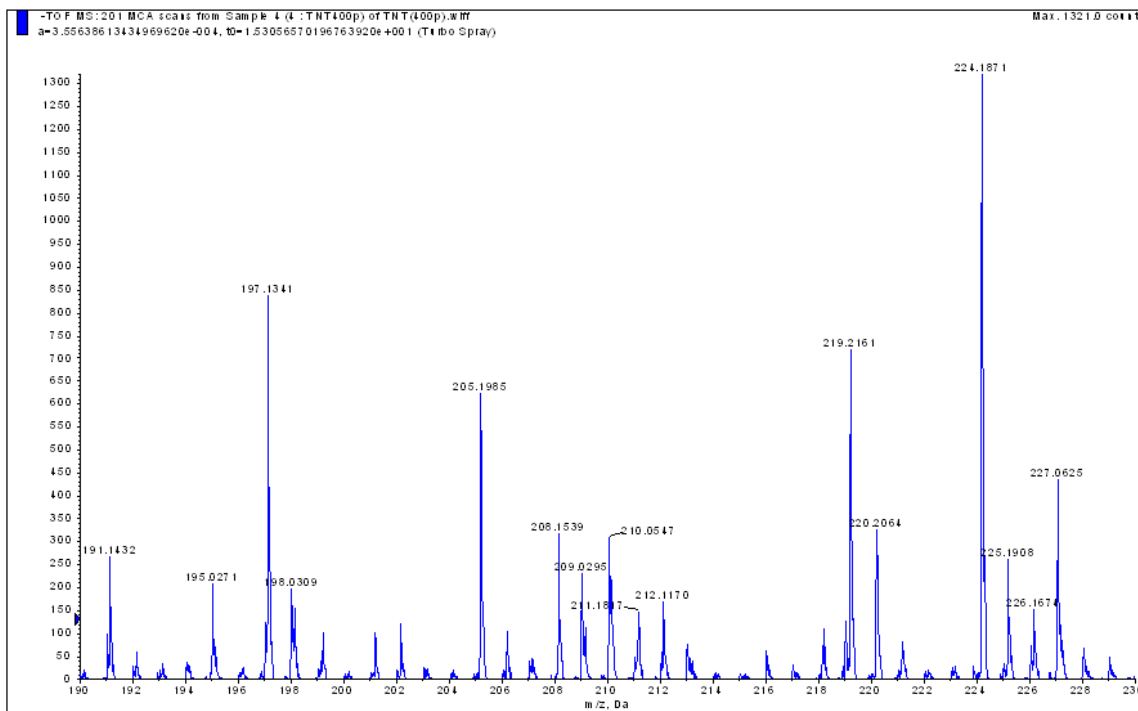


Figure 6.22. Spectrum of TNT using 400 pg/ml of TNT at 180 C

increase, from around 900 to more than 1200. The possible reason is this substance can be activated by high temperature too, and this temperature is higher than 150 C. This might be helpful to find out the disturbing substances. The total counts increase compared to the tests under 150 C, which agrees with the previous hypothesis.

If we build up the function of concentration-count, it will be hard to analyze since the differences among concentrations are huge. Therefore the concentration of TNT is taken the logarithm, and the graphs for each temperature are plotted as following. (Fig. 6.29 - Fig. 6.32)

It is surprising that the logarithm of the concentration and the total counts of all peaks can agree to a linear relation quite well. This might indicate the vapor pressure

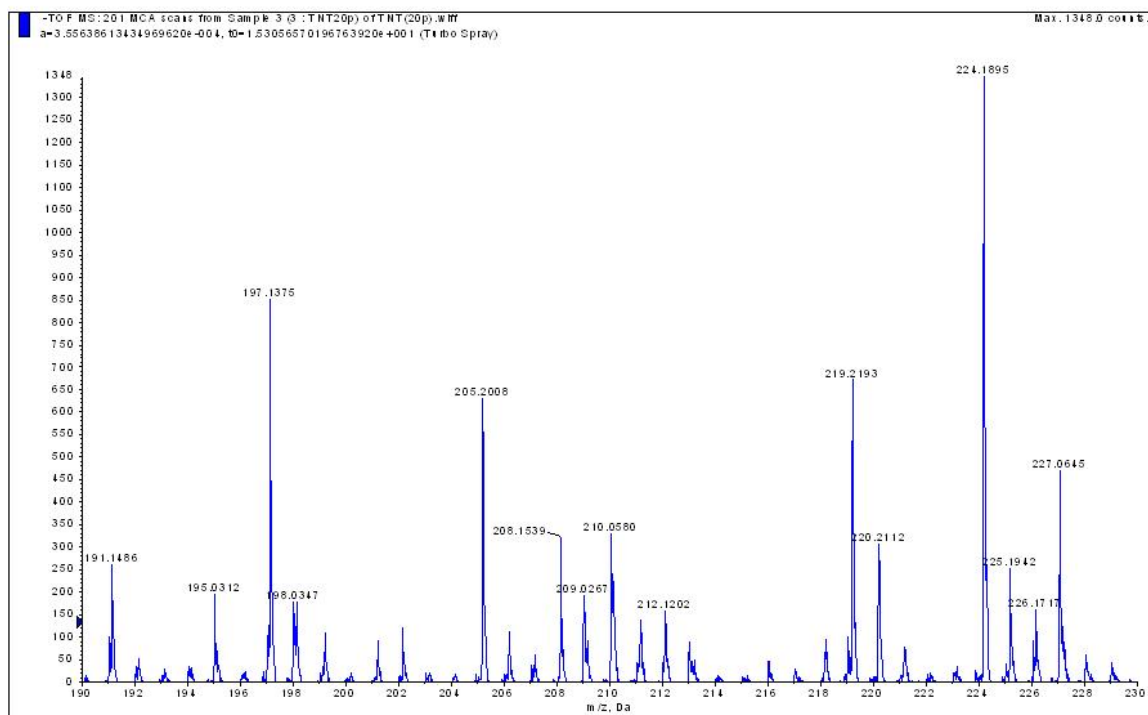


Figure 6.23. Spectrum of TNT using 20 pg/ml of TNT at 180 C

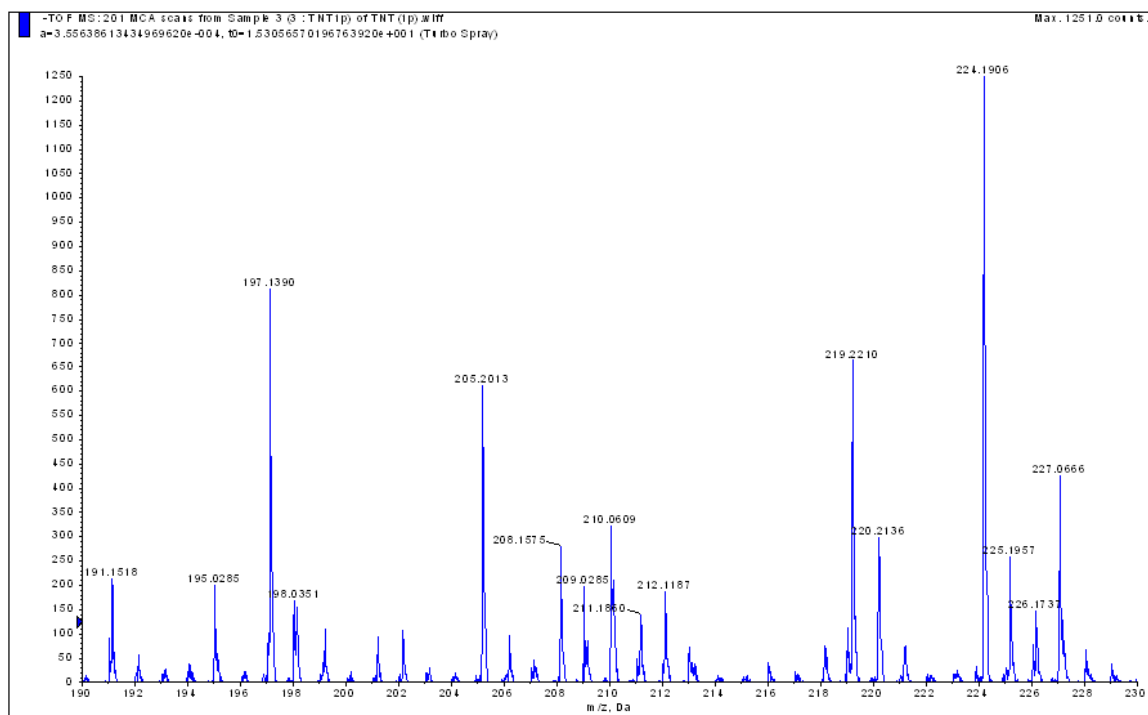


Figure 6.24. Spectrum of TNT using 1 pg/ml of TNT at 180 C

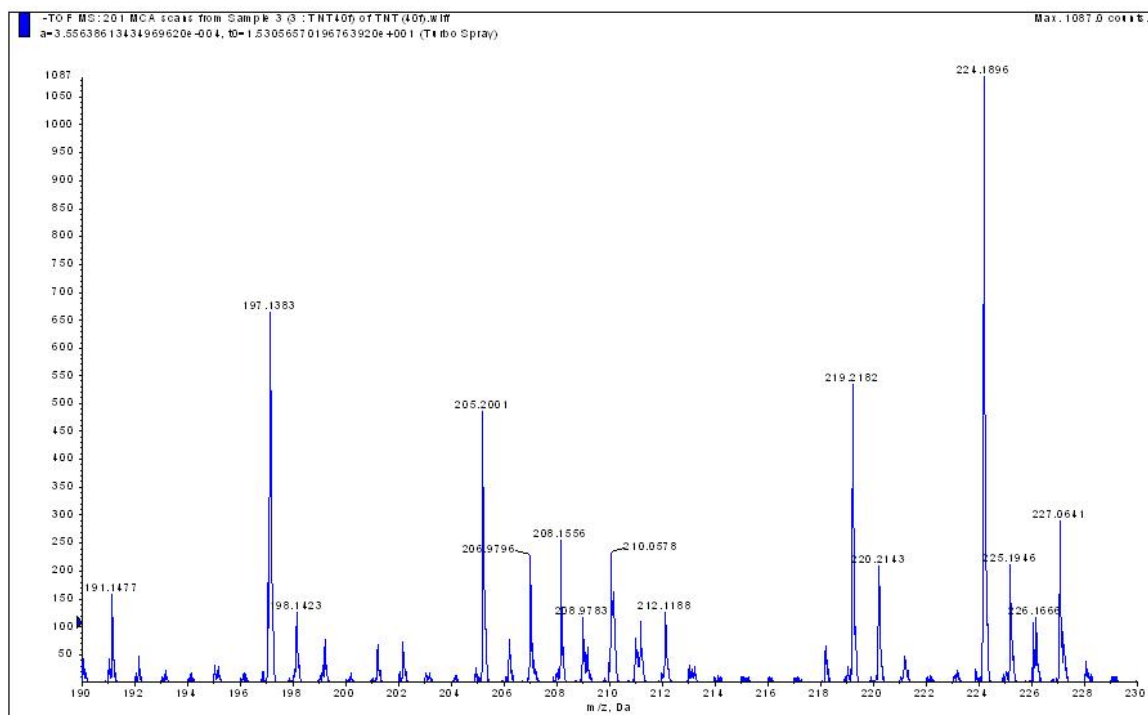


Figure 6.25. Spectrum of TNT using 40 fg/ml of TNT at 180 C

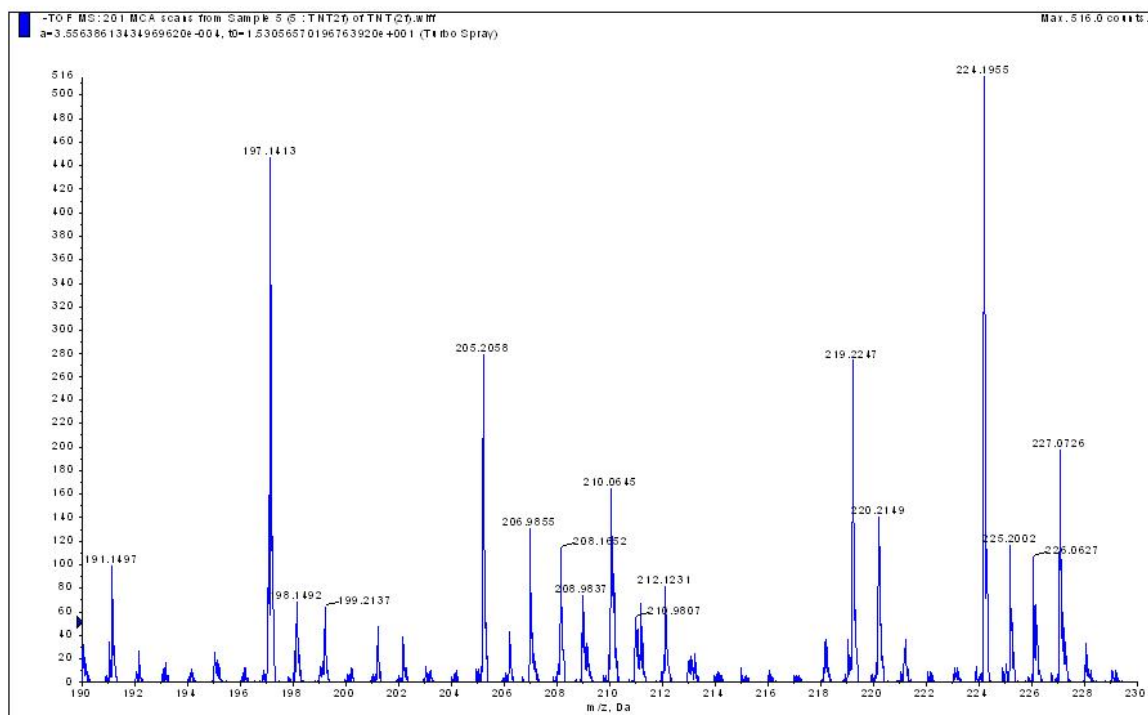


Figure 6.26. Spectrum of TNT using 2 fg/ml of TNT at 180 C

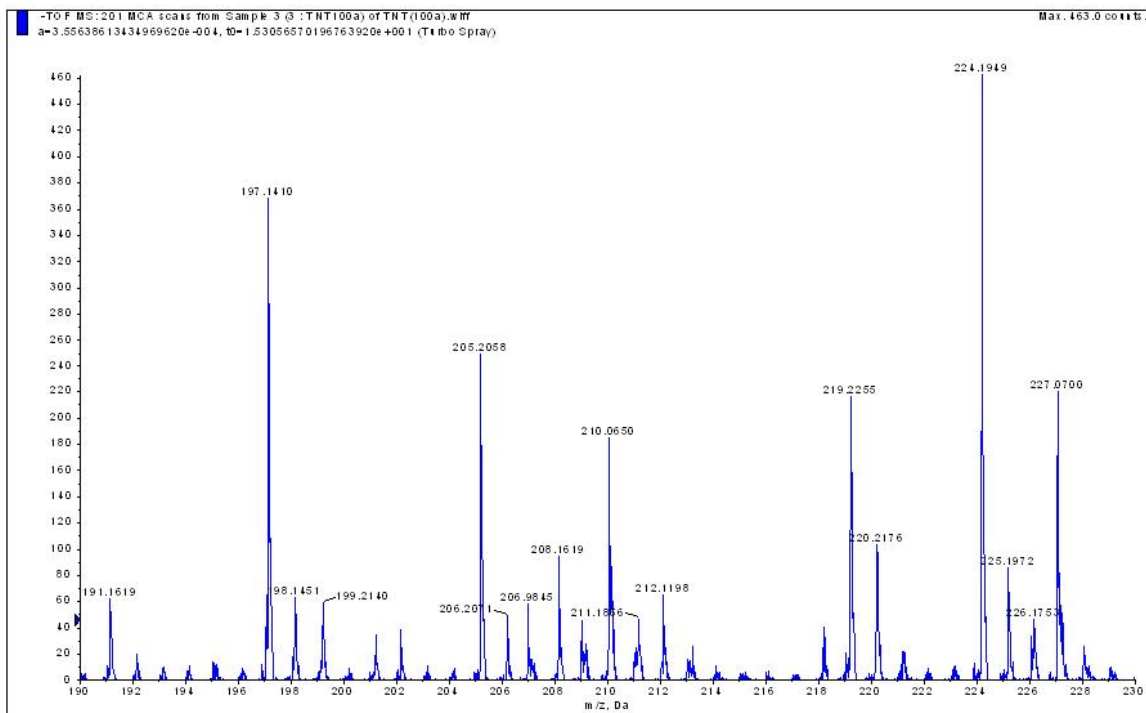


Figure 6.27. Spectrum of TNT using 100 ag/ml of TNT at 180 C

TNT CONCENTRATION (g/ml)	INTENSITY (120 C)	INTENSITY (150 C)	INTENSITY (180 C)
400p	2563	2576	2929
20p	2154	2414	2859
1p	1668	1887	2281
40f	1843	1756	1773
2f	1005	1693	1433
100a	601	833	1001

Figure 6.28. Total counts for selected peaks for different temperature

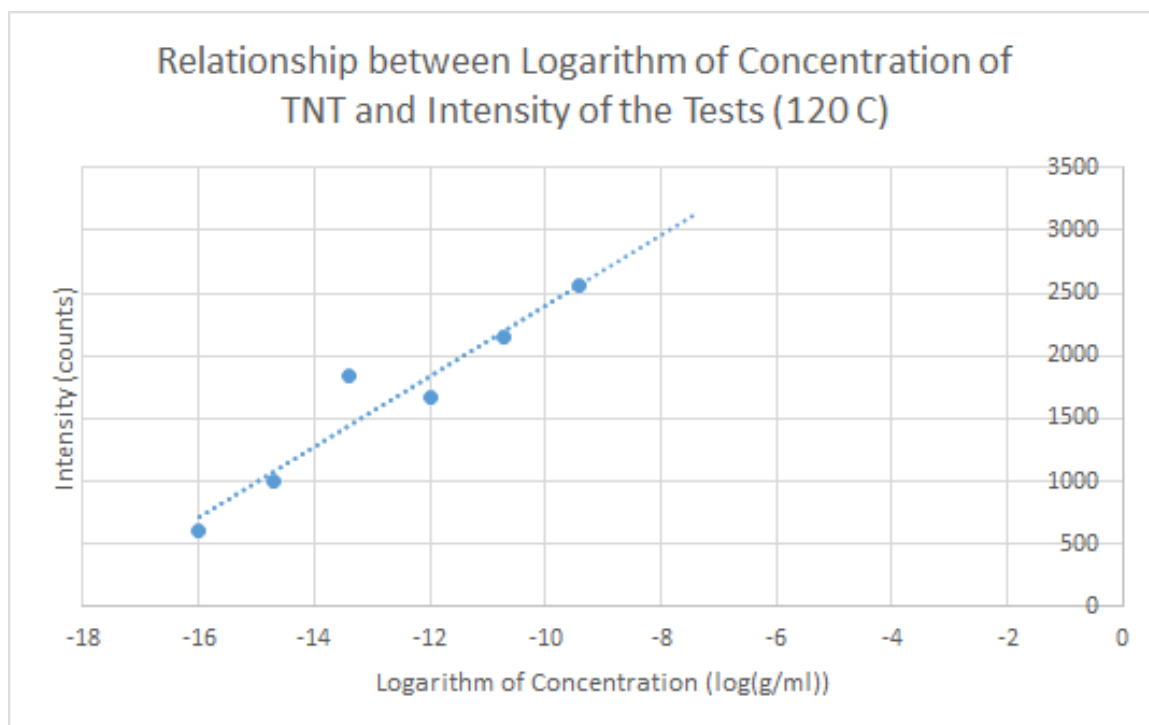


Figure 6.29. Log (concentration) - count relation at 120 C

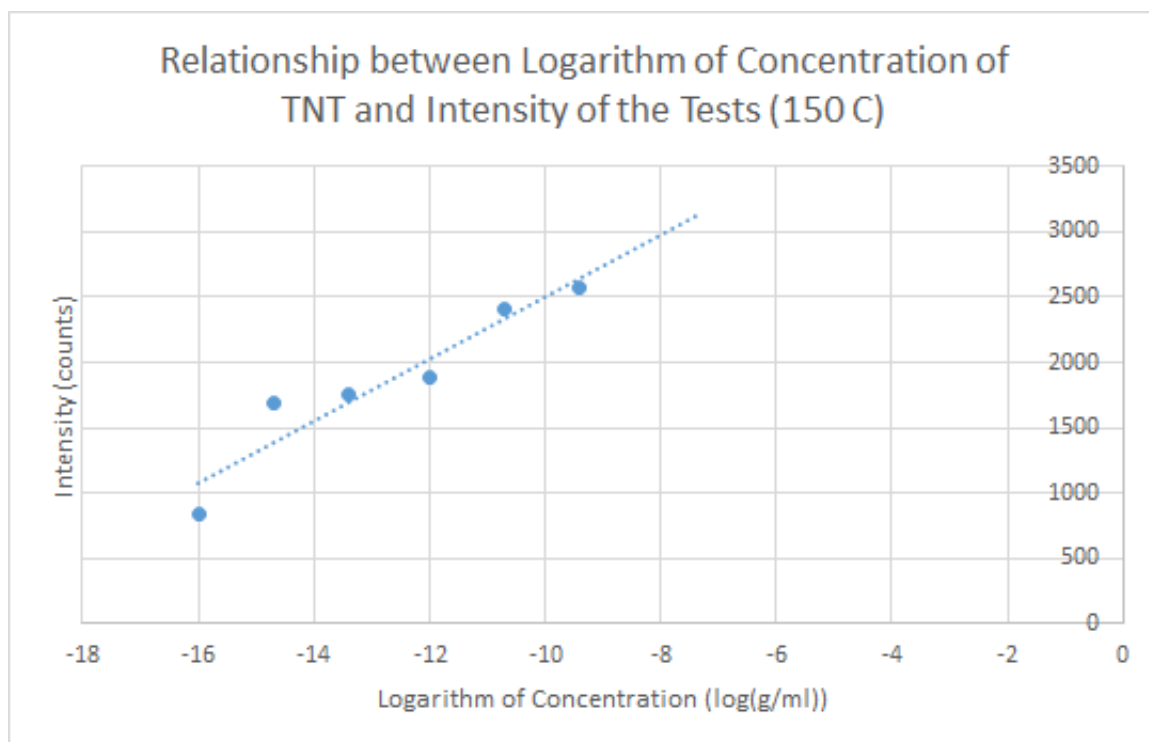


Figure 6.30. Log (concentration) - count relation at 150 C

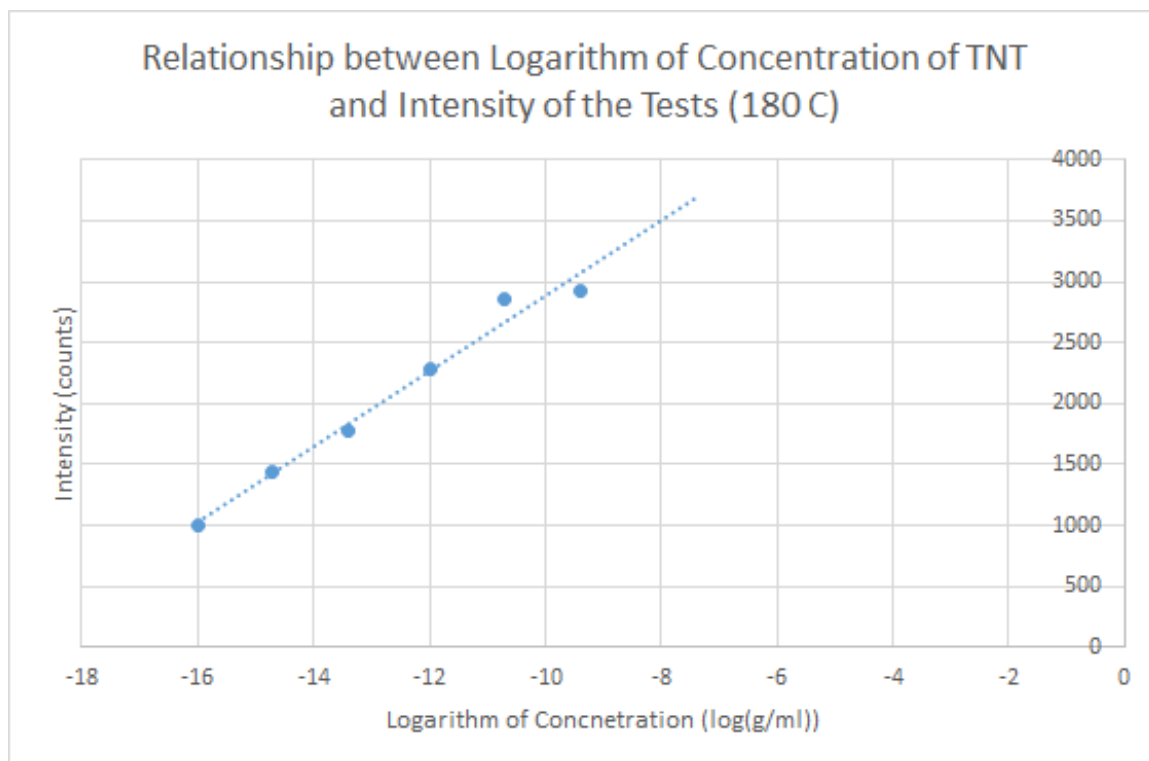


Figure 6.31. Log (concentration) - count relation at 180 C

TNT Concentration (g/ml)	Sensitivity (parts per quadrillion)
400 pico	4167
20 pico	208.3
1 pico	10.42
40 femto	0.4167
2 femto	0.02083
100 atto	0.001042

Figure 6.32. Sensitivity achieved in the tests

of TNT change linearly according to the logarithm of the quantity of the TNT exposed to the environment. Furthermore, the good agreement in total counts might also indicate all the 9 peaks selected are the products of TNT molecule. Furthermore, it can be noticed that when the test is conducted under higher temperature, the results performed better to the fitting line function. This phenomenon indicate a higher temperature will trigger to a more complete release of TNT in the filter paper, while TNT might be harder to release when the concentration is low.

## 7. FUTURE WORK

### 7.1 For Optimization

#### 7.1.1 Use Various Buffer Gas

The utilized IMS-MS system will face some problem when we are studying some isomers. Isomers will have exactly identical molecular mass, which means the MS system cannot separate them from each other. Moreover, some isomers such as leucine and isoleucine (Fig. 7.1) have very similar structure and therefore they possess very close ion mobility. This means it is still very hard to distinguish such isomers by using ion mobility spectrometry. However, when the researchers use gas molecule with high polarizability as the buffer gas, such as carbon dioxide, a separation is achieved. No explanation can be made because no enough knowledge about the parameters with the CO<sub>2</sub> as the buffer gas is available to date. If the optimization of parameters in CCS can be operated by using CO<sub>2</sub> as buffer gas, researchers can have a deeper understanding about the separation of isomers.

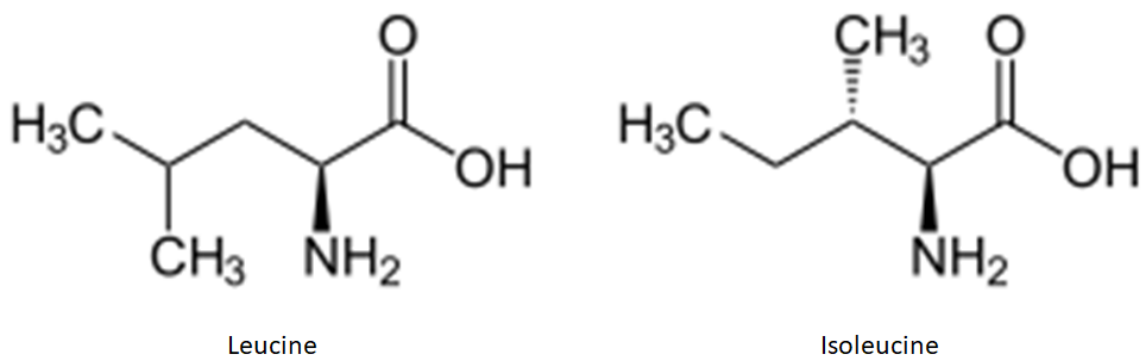


Figure 7.1. Leucine and isoleucine

### 7.1.2 Further Optimization Using CCS of Amino Acids

One of the most significant shortcomings of the previous experiments caused by the chemical compounds selected. All the 16 kinds of compounds have high percentage of carbon and hydrogen atoms, but not many oxygen, nitrogen and fluorine atoms appear. This is possibly trigger to inaccuracy of the optimization result. Although the parameters optimized for carbon and hydrogen are pretty persuasive, without sufficient samples containing the studied elements would possibly lead to unreliable conclusion. Even in the early stage of the optimization, the results of nitrogen and fluorine show different properties compared to other elements. This can be considered as the outcome of insufficient amount of targeted atoms, which make the extreme cases more likely to survive after the optimization and generalization of the parameters for all kind of molecules become impossible. In order to improve the optimization, utilizing the experimental results of the CCS for amino acids to conduct the further optimization become a reasonable choice. All the proteinogenic amino acid molecules have a considerable weight of both oxygen and nitrogen atom. The identical process of optimization were run toward the CCS of amino acids from multiple source. The experimental data from GR Asbury et. al. [75], L.W. Beegle et. al. [76], C.J. Bramwell et. al. [77] and T.W. Knapman et. al. [78] can be applied. All the above experiments use nitrogen as the buffer gas. Moreover, the experiments conducted by L.W. Beegle et. al. utilize carbon dioxide and argon as the gas flow too, which has a significant meaning for the optimization. Because the nitrogen is cheap and easily accessible, most of the relevant experiment will choose nitrogen as the neutral buffer gas. Using multiple buffer gas will be helpful to acquire more comprehensive analysis of the collision cross section calculation.

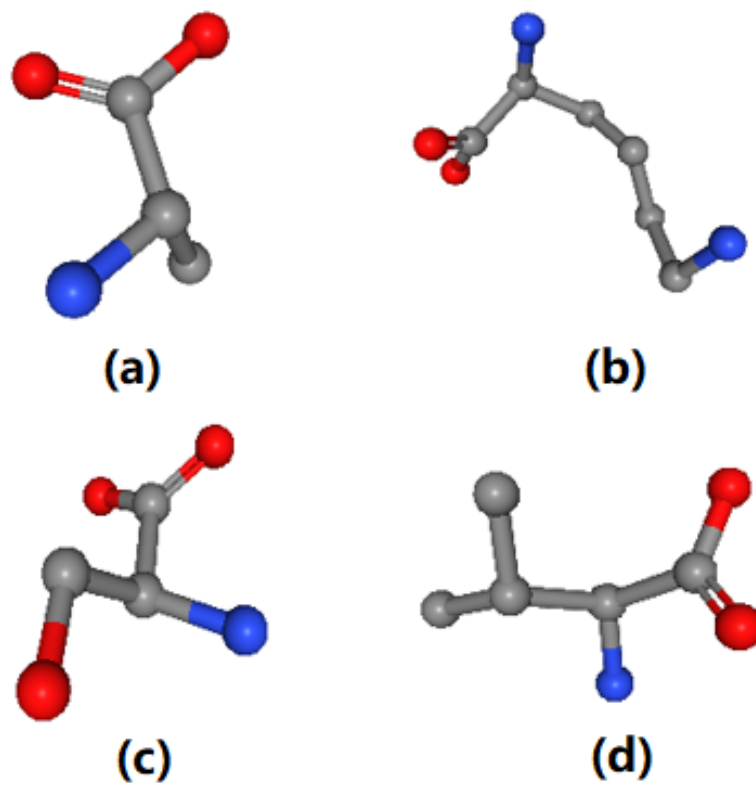


Figure 7.2. Several 3D images of the DFT structure of amino acid molecules

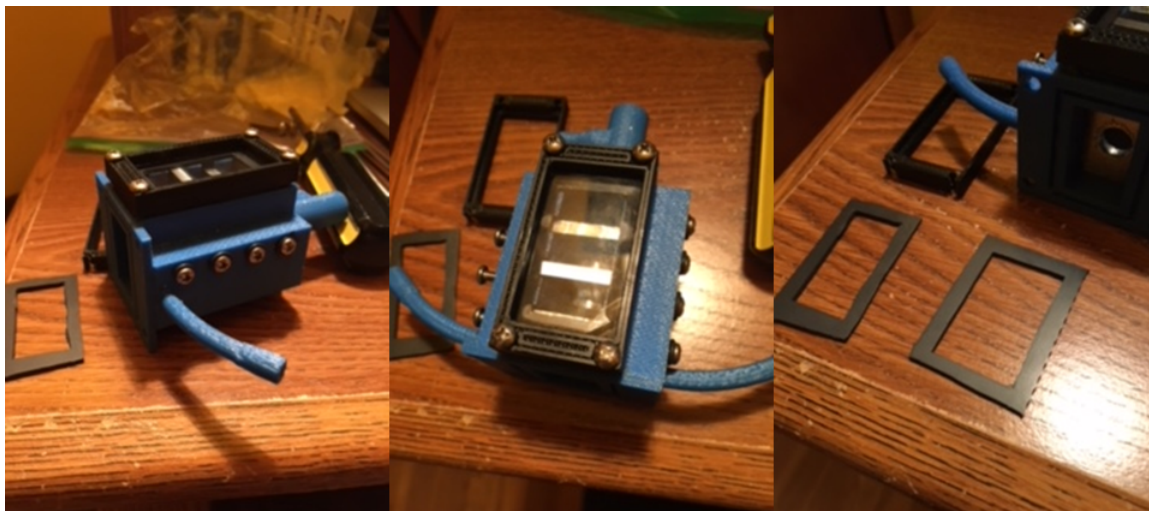


Figure 7.3. Different Perspectives of New Chamber

## 7.2 For TNT Detection

### 7.2.1 More Efficient Way to Charge Particle

Although a high sensitivity has been achieved in the previous experiment, some measures can be applied to improve the sensitivity more. One factor restrict the performance of detection is the charging rate of particles, in another word, many signals of TNT are lost since the majority of the particles brought to the system are not successfully ionized. In order to enhance the efficiency of ionization, a new design of charging chamber is put forward by Tim Poe.(Fig. 7.3) In the new chamber multiple additional electric fields are applied. Before the explosive molecules enter the DMA both the explosives and the charging solution will be accelerated by the newly applied electric field, which make the explosives have a higher chance to be charged. (Fig. 7.4)

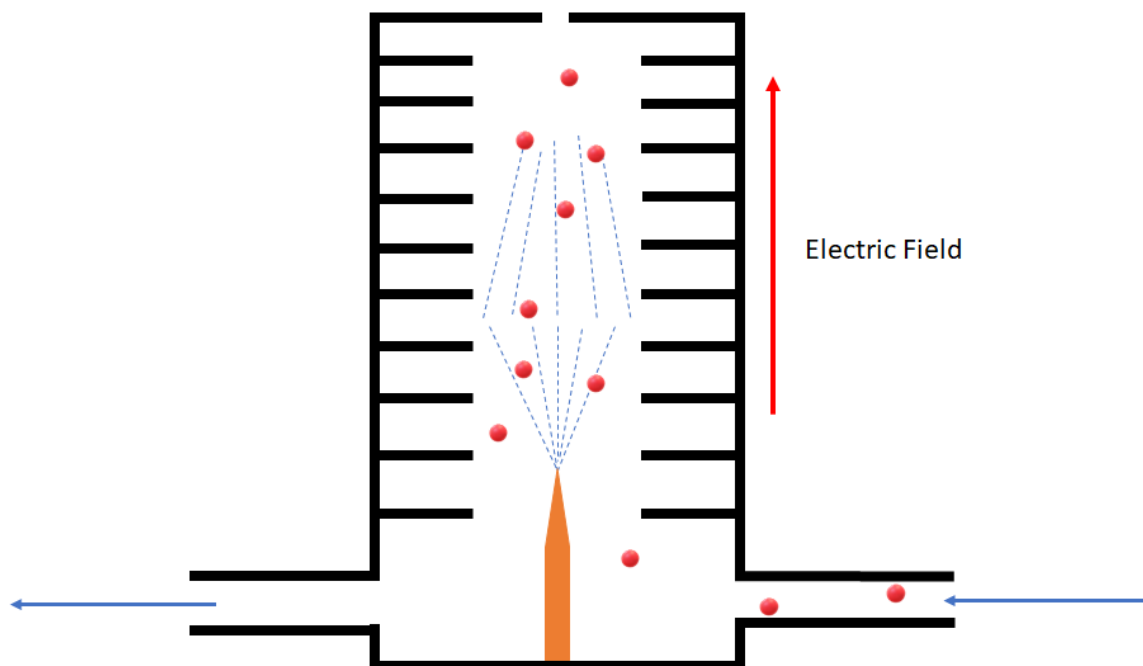


Figure 7.4. Mechanism of New Chamber

### **7.2.2 More Accurate Temperature Control**

In this work only three different temperatures are taken into consideration. One factor to restrict a more comprehensive analysis depend on various temperature is the poor control of the heating. Even with the aluminum foil, it always take long time to heat up the collection chamber to the targeted temperature. In the future study, a more specific temperature control device will be indispensable.

### **7.2.3 Universal Filter**

Currently a layer of acetone is selected to form a layer cover the filter paper, since TNT has a high solubility in acetone. However, this will only work for TNT. For other explosives have different structure compared to TNT, acetone may not be capable to perform as wonderful as testing TNT. If we want to improve the research, a universal filter will be a good direction. Activated carbon is one of the candidates.

### **7.2.4 Cleaning of Explosives**

The residual within the devices might significantly influence the outcome of the experiment. Although the collection chamber was carefully cleaned after each trial of test, the residue of TNT within the tube and even the DMA-MS system will be much harder to remove. If a more specific relation between concentration and the intensity of the signal is desired, a more efficacious approach needs to be found to clean the explosives.

## 8. SUMMARY

A brand new approach used to optimize the CCS calculation without need of the knowledge of the initial values for well-depth and intercept was established. New series of intercepts and well-depths values were generated.

- For the small and rigid molecules, the DFT calculation was selected as the method to generate their initial geometric structures. The geometry in the gas phase would be easily affected by many factors, for example, temperature and pressure. The result from the DFT calculation is anticipated to show discrepancies depending on the temperature and pressure. It would be the same of the frequency optimization numbers. Still, the DFT calculation provide a well-defined and reproducible way to generate reliable geometries. DFT calculations have been shown to yield good approximations for CCS. Be attention that the performed DFT did not take the temperature and pressure into account yet, the resulting structures should be utilized carefully.
- 16 kinds of chemical compounds with 5 elements, carbon, hydrogen, oxygen, nitrogen and fluorine were selected to conducted the numerical optimization. Those molecules are widely used in the experiments for the optimization of Lennard-Jones parameters considering the ion-quadruple potentials in the CCS calculation using nitrogen as buffer gas. Therefore they will be ideal candidates for our work.
- A quadric function  $F$  was built up in order to evaluate the optimization process. The errors between calculated and experimentally CCS are therefore shown directly. The perfect optimization will lead to a zero value for this evaluation function.

- The 4-6-12 potential was chosen as the fundamental function for the numerical calculation of CCS. IMoS was used to calculate the CCS in nitrogen gas while the effects of ion-quadruple potentials would be neglected. It is hypothesized that the effect of the ion-quadrupole potential together with the vibrations, translation and rotation of atoms can all be embedded in well optimized L-J parameters.
- Because of the difficulty of interpreting a general optimization method with multiple unknowns, a *ceteris paribus* assumption was incorporated to understand causation of each of the different parameters and each of the elements. Only one element will be conducted in the optimization at one moment. This requires the method to be iterative.
- Several thousand of CCS calculation were conducted in order to obtain the mapped surfaces of the evaluated elements. For most of the elements studied, the mapped surface will present a line of global minimum, and the mathematic expression for this line will be an exponential function between the well-depth and intercept. The physical explanation could be that the effects brought by the increase of potential well-depth can be equilibrated by the decrease of intercept. Among all the values in the line of global minimum, we need to select a pair of values for L-J parameters. To the extent that was possible, the Lorentz-Berthelot combination rule was used to establish a value for the intercept.
- To ensure different routine of optimization will not affect the final values, the orders started by carbon and hydrogen were tested alternatively.

And the following conclusions can be obtained:

- New optimized Lennard-Jones parameters have been obtained for carbon, hydrogen, oxygen, nitrogen and fluorine in N<sub>2</sub>. The resulting numerical CCS are mostly within 1 percent of their experimental counterparts.

- The numerical calculation excluded the ion-quadrupole potential. It has been demonstrated that the effects of ion-quadrupole together with other effects such as atom vibrations and diffuse collisions would be included by the optimized Lennard-Jones parameters without significantly affecting the CCS. The computational efficiency will be enhanced by a large extent by removing the calculation of those parameters. In the process of optimization, we also found that the effects of hydrogen can be embedded into the influence of heavier atoms, which means the optimization can possibly finished without the calculation of hydrogen.
- Although we have selected a final group of Lennard-Jones parameters, other sets with largely different values could have been selected while providing accurate CCS.
- When running the process for rigid and semi-rigid small molecule, the geometric structure obtained by DFT calculation will be very reliable. However, the L-J parameters gained by this approach are not suggested to be used in conjunction with Molecular Dynamics calculations. Furthermore, for molecules which have large flexibility in the geometric structure, the approach of DFT will no longer be suitable. These L-J parameters should also not be used in conjunction with ion-quadrupole potential methods in N2.
- Under this designed mechanism, in order to obtain more reliable parameters, the studied elements should have a strong weight in the tested molecules. Selecting appropriate molecules for the CCS calculation is important for the optimization.

Furthermore, a detection of TNT with high sensitivity was operated, two different strategies were applied. The detection of TNT from the vaporized solution can demonstrate the reliability of DMA-MS system in the issue of explosives detection:

- The regular MS test for the TNT was operated at the beginning. High concentration of TNT solution with charging substance is tested to make the electro-spray and introduced into the DMA-MS system. Ammonium acetate is selected

as the substance to ionize TNT molecule to prevent unpredictable chemical reaction. The purpose of this trial is confirming the potential the DMA should apply. When the corresponding DMA potential is obtained, the following experiments will maintain this constant potential.

- The most appropriate concentration of the charging solution is determined in the next step. A high concentration of ammonium acetate can ionize unwanted substances at the same time it charge TNT, which will generate disturbance to the analysis of the TNT signal in the mass spectra. After determine the most appropriate concentration, all the test in the following will keep the charging solution the same concentration.
- Detection of the TNT from the vaporized solution was conducted from relatively high concentration to low concentration. The DMA-MS system is settled in constant potential mode. An impulse of dry air flow is offered during the trial and generate an obvious jump of signal in the mass spectrum. A signal shows the typical mass-to-charge ratio of TNT molecule or fragments with a high intensity indicate the detection of TNT.
- The peak of typical TNT  $m/z$  value should have a strong intensity outweigh most of the rest peak in the mass spectrum for a successful detection. If the peak of the TNT  $m/z$  value does not exert compared to other peaks, even it has a strong intensity, it cannot be considered as a detection since the signal can come from the residual.
- TNT solution with concentration of 160 ng/ml seems to be the limit of these method. The spectrum shows plenty of non-targeted substance while the targeted TNT molecule or fragments have a weak signal compare to other peaks.

In order to achieve a detection with higher sensitivity, the system containing functions of absorption, release and detection is designed. TNT solution is put inside

an enclosed reservoir to simulate the environment. Lower concentration of TNT solutions are tested using this system, and the following conclusions can be obtained:

- The new system designed to detect the TNT has a much more sensitive performance compared to the system used for detecting TNT from the vaporized solution. The filter paper used to absorb and release the TNT is the major reason to guarantee a better performance.
- Experiments using different heating temperatures of the collection chamber are conducted for each concentration of TNT solution selected. The data of the mass spectra shows that with higher temperature, the signals for TNT become stronger. This can be explained as the higher temperature makes more acetone used to trap the TNT evaporate. Therefore, more TNT molecules are free and can be brought to the DMA-MS system.
- The major peaks targeted have the mass-to-charge ratio of 197, 210 and 227. In order to obtain a comprehensive analysis, peaks with mass-to-charge ratios of 196, 198, 209, 211, 226, 228 are collected too. Not every single peak will become smaller strictly corresponding to the reduction of the concentration of the TNT solution used in the enclosed reservoir, but the summation of the intensity of all the peaks collected will always decrease when the quantity of TNT inputted in the reservoir decreases.
- Plot a graph of the counts collected with respect to the logarithm of the concentrations operated will trigger to a linear function. This result can be translated to the vapor pressure of TNT will change linearly as the quantity of the TNT exists in the environment. These results agree with the fact that the TNT vapor pressure is low even in the severely polluted area.
- The sensitivity achieved by the system is 1 part per quintillion so far. Nevertheless, this might not be exactly correct due to the potentially existing residue within the system. With improved cleaning methods and better efficiency of ionization,

a better performance can be anticipated. Moreover, using more specific control of the temperature and the filter suitable for different types of explosives, a deeper understanding of explosives behaviors can be acquired.

## REFERENCES

## REFERENCES

- [1] Abu B Kanu, Prabha Dwivedi, Maggie Tam, Laura Matz, and Herbert H Hill. Ion mobility–mass spectrometry. *Journal of mass spectrometry*, 43(1):1–22, 2008.
- [2] Cris Laphorn, Frank Pullen, and Babur Z Chowdhry. Ion mobility spectrometry–mass spectrometry (ims–ms) of small molecules: separating and assigning structures to ions. *Mass spectrometry reviews*, 32(1):43–71, 2013.
- [3] D Isailovic, RT Kurulugama, MD Plasencia, ST Stokes, Z Kyselova, R Goldman, Y Mechref, MV Novotny, and DE Clemmer. Profiling of human serum glycans associated with liver cancer and cirrhosis by ims–ms. *Journal of proteome research*, 7(3):1109–1117, 2008.
- [4] Manolo D Plasencia, Dragan Isailovic, Samuel I Merenbloom, Yehia Mechref, and David E Clemmer. Resolving and assigning n-linked glycan structural isomers from ovalbumin by ims–ms. *Journal of the American Society for Mass Spectrometry*, 19(11):1706–1715, 2008.
- [5] Francisco A Fernandez-Lima, Christopher Becker, Amy M McKenna, Ryan P Rodgers, Alan G Marshall, and David H Russell. Petroleum crude oil characterization by ims–ms and fticr ms. *Analytical chemistry*, 81(24):9941–9947, 2009.
- [6] Sarah Trimpin, Manolo Plasencia, Dragan Isailovic, and David E Clemmer. Resolving oligomers from fully grown polymers with ims–ms. *Analytical chemistry*, 79(21):7965–7974, 2007.
- [7] Giuseppe Paglia, Michal Kliman, Emmanuelle Claude, Scott Geromanos, and Giuseppe Astarita. Applications of ion-mobility mass spectrometry for lipid analysis. *Analytical and bioanalytical chemistry*, 407(17):4995–5007, 2015.
- [8] Jacek P Dworzanski, William H McClellenn, Paul A Cole, Sidney N Thornton, Henk LC Meuzelaar, Neil S Arnold, and A Peter Snyder. Field-portable, automated pyrolysis-gc/ims system for rapid biomarker detection in aerosols: A feasibility study. *Field Analytical Chemistry & Technology*, 1(5):295–305, 1997.
- [9] JW Leonhardt. A new ppb-gas analyzer by means of gc-ion mobility spectrometry (gc-ims). *Journal of Radioanalytical and Nuclear Chemistry*, 257(1):133–139, 2003.
- [10] Lawrence V Haley and Govindanunny Thekkadath. Hand-held detection system using gc/ims, November 19 2002. US Patent 6,481,263.
- [11] Wolfgang Vautz, Bertram Bödeker, Sabine Bader, and Jörg Ingo Baumbach. Recommendation of a standard format for data sets from gc/ims with sensor-controlled sampling. *International Journal for Ion mobility spectrometry*, 11(1-4):71–76, 2008.

- [12] Xiaoyun Liu, Stephen J Valentine, Manolo D Plasencia, Sarah Trimpin, Stephen Naylor, and David E Clemmer. Mapping the human plasma proteome by scx-lc-ims-ms. *Journal of the American Society for Mass Spectrometry*, 18(7):1249–1264, 2007.
- [13] Sunnie Myung, Young Jin Lee, Myeong Hee Moon, John Taraszka, Rena Sowell, Stormy Koeniger, Amy E Hilderbrand, Stephen J Valentine, Lucy Cherbas, Peter Cherbas, et al. Development of high-sensitivity ion trap ion mobility spectrometry time-of-flight techniques: a high-throughput nano-lc-ims-tof separation of peptides arising from a drosophila protein extract. *Analytical chemistry*, 75(19):5137–5145, 2003.
- [14] Erin Shammel Baker, Eric A Livesay, Daniel J Orton, Ronald J Moore, William F Danielson III, David C Prior, Yehia M Ibrahim, Brian L LaMarche, Anoop M Mayampurath, Athena A Schepmoes, et al. An lc-ims-ms platform providing increased dynamic range for high-throughput proteomic studies. *Journal of proteome research*, 9(2):997–1006, 2010.
- [15] John A Taraszka, Ruwan Kurulugama, Rena A Sowell, Stephen J Valentine, Stormy L Koeniger, Randy J Arnold, David F Miller, Thomas C Kaufman, and David E Clemmer. Mapping the proteome of drosophila melanogaster: Analysis of embryos and adult heads by lc-ims-ms methods. *Journal of proteome research*, 4(4):1223–1237, 2005.
- [16] Rena A Sowell, Stormy L Koeniger, Stephen J Valentine, Myeong Hee Moon, and David E Clemmer. Nanoflow lc/ims-ms and lc/ims-cid/ms of protein mixtures. *Journal of the American Society for Mass Spectrometry*, 15(9):1341–1353, 2004.
- [17] Michael A Ewing, Matthew S Glover, and David E Clemmer. Hybrid ion mobility and mass spectrometry as a separation tool. *Journal of Chromatography A*, 1439:3–25, 2016.
- [18] ThermoFisher Scientific. Overview of mass spectrometry for protein analysis, 2016.
- [19] John B Fenn, Matthias Mann, Chin Kai Meng, Shek Fu Wong, and Craig M Whitehouse. Electrospray ionization for mass spectrometry of large biomolecules. *Science*, 246(4926):64–71, 1989.
- [20] Koichi Tanaka, Hiroaki Waki, Yutaka Ido, Satoshi Akita, Yoshikazu Yoshida, Tamio Yoshida, and T Matsuo. Protein and polymer analyses up to m/z 100 000 by laser ionization time-of-flight mass spectrometry. *Rapid communications in mass spectrometry*, 2(8):151–153, 1988.
- [21] Michael Karas, Doris Bachmann, Ute Bahr, and Franz Hillenkamp. Matrix-assisted ultraviolet laser desorption of non-volatile compounds. *International journal of mass spectrometry and ion processes*, 78:53–68, 1987.
- [22] Michael Barber, Robert S Bordoli, R Donald Sedgwick, and Andrew N Tyler. Fast atom bombardment of solids (fab): A new ion source for mass spectrometry. *Journal of the Chemical Society, Chemical Communications*, (7):325–327, 1981.
- [23] Milam SB Munson and F-H. Field. Chemical ionization mass spectrometry. i. general introduction. *Journal of the American Chemical Society*, 88(12):2621–2630, 1966.

- [24] Ellen C Hopmans, Stefan Schouten, Richard D Pancost, Marcel T J van der Meer, and Jaap S Sinninghe Damste. Analysis of intact tetraether lipids in archaeal cell material and sediments by high performance liquid chromatography/atmospheric pressure chemical ionization mass spectrometry. *Rapid Communications in Mass Spectrometry*, 14(7):585–589, 2000.
- [25] AP Bruins. Mass spectrometry with ion sources operating at atmospheric pressure. *Mass Spectrometry Reviews*, 10(1):53–77, 1991.
- [26] Robert H Bateman, Jeff Brown, Marc Lefevre, Robert Flammang, and Yves Van Haverbeke. Applications in gaseous ion and neutral chemistry using a six-sector mass spectrometer. *International journal of mass spectrometry and ion processes*, 115(2-3):205–218, 1992.
- [27] Michael Guilhaus. Special feature: Tutorial. principles and instrumentation in time-of-flight mass spectrometry. physical and instrumental concepts. *Journal of mass spectrometry*, 30(11):1519–1532, 1995.
- [28] Philip E Miller and M Bonner Denton. The quadrupole mass filter: basic operating concepts. *Journal of chemical education*, 63(7):617, 1986.
- [29] John Edward Fulford, Duong Nhu-Hoa, Richard James Hughes, Raymond Evans March, Ronald Francis Bonner, and Gordon John Wong. Radio-frequency mass selective excitation and resonant ejection of ions in a three-dimensional quadrupole ion trap. *Journal of Vacuum Science and Technology*, 17(4):829–835, 1980.
- [30] Garth E Patterson, Andrew J Guymon, Leah S Riter, Mike Everly, Jens Griep-Raming, Brian C Laughlin, Zheng Ouyang, and R Graham Cooks. Miniature cylindrical ion trap mass spectrometer. *Analytical chemistry*, 74(24):6145–6153, 2002.
- [31] John EP Syka, Jarrod A Marto, Dina L Bai, Stevan Horning, Michael W Senko, Jae C Schwartz, Beatrix Ueberheide, Benjamin Garcia, Scott Busby, Tara Muratore, et al. Novel linear quadrupole ion trap/ft mass spectrometer: performance characterization and use in the comparative analysis of histone h3 post-translational modifications. *Journal of proteome research*, 3(3):621–626, 2004.
- [32] Jesper V Olsen, Lyris MF de Godoy, Guoqing Li, Boris Macek, Peter Mortensen, Reinhold Pesch, Alexander Makarov, Oliver Lange, Stevan Horning, and Matthias Mann. Parts per million mass accuracy on an orbitrap mass spectrometer via lock mass injection into a c-trap. *Molecular & Cellular Proteomics*, 4(12):2010–2021, 2005.
- [33] Melvin B Comisarow and Alan G Marshall. Fourier transform ion cyclotron resonance spectroscopy. *Chemical physics letters*, 25(2):282–283, 1974.
- [34] Joseph Ladislav Wiza et al. Microchannel plate detectors. *Nucl. Instrum. Methods*, 162(1-3):587–601, 1979.
- [35] Carlos Larriba and Christopher J Hogan Jr. Free molecular collision cross section calculation methods for nanoparticles and complex ions with energy accommodation. *Journal of Computational Physics*, 251:344–363, 2013.

- [36] Alexandre A Shvartsburg and Martin F Jarrold. An exact hard-spheres scattering model for the mobilities of polyatomic ions. *Chemical physics letters*, 261(1-2):86–91, 1996.
- [37] Carlos Larriba and Christopher J Hogan Jr. Ion mobilities in diatomic gases: measurement versus prediction with non-specular scattering models. *The Journal of Physical Chemistry A*, 117(19):3887–3901, 2013.
- [38] Susan K Meyers, Shiping Deng, Nick T Basta, William W Clarkson, and Gregory G Wilber. Long-term explosive contamination in soil: effects on soil microbial community and bioremediation. *Soil & Sediment Contamination*, 16(1):61–77, 2007.
- [39] N Pon Saravanan, S Venugopalan, N Senthilkumar, P Santhosh, B Kavita, and H Gurumallesh Prabu. Voltammetric determination of nitroaromatic and nitramine explosives contamination in soil. *Talanta*, 69(3):656–662, 2006.
- [40] Jim C Spain. Biodegradation of nitroaromatic compounds. *Annual Reviews in Microbiology*, 49(1):523–555, 1995.
- [41] Koffi Badjagbo and Sébastien Sauvé. Mass spectrometry for trace analysis of explosives in water. *Critical Reviews in Analytical Chemistry*, 42(3):257–271, 2012.
- [42] DL Kaplan and AM Kaplan. Thermophilic biotransformations of 2, 4, 6-trinitrotoluene under simulated composting conditions. *Applied and Environmental Microbiology*, 44(3):757–760, 1982.
- [43] Jeffrey I Steinfeld and Jody Wormhoudt. Explosives detection: a challenge for physical chemistry. *Annual review of physical chemistry*, 49(1):203–232, 1998.
- [44] BC Dionne, DP Rounbehler, EK Achter, JR Hobbs, and DH Fine. Vapor pressure of explosives. *Journal of Energetic Materials*, 4(1-4):447–472, 1986.
- [45] Carsten Steuckart, Edith Berger-Preiss, and Karsten Levsen. Determination of explosives and their biodegradation products in contaminated soil and water from former ammunition plants by automated multiple development high-performance thin-layer chromatography. *Analytical Chemistry*, 66(15):2570–2577, 1994.
- [46] Dudley Williams and George Pappas. Ultra-rapid soil screening with the use of gc-saw technology for tnt/dnt and related nitroaromatic contaminants. *Field Analytical Chemistry & Technology*, 2(5):299–308, 1998.
- [47] Abdelkader Hilmi, John HT Luong, and An-Lac Nguyen. Development of electrokinetic capillary electrophoresis equipped with amperometric detection for analysis of explosive compounds. *Analytical chemistry*, 71(4):873–878, 1999.
- [48] Abdelkader Hilmi, John HT Luong, and An-Lac Nguyen. Determination of explosives in soil and ground water by liquid chromatography–amperometric detection. *Journal of chromatography A*, 844(1-2):97–110, 1999.
- [49] Abdelkader Hilmi and John HT Luong. In-line coupling capillary electrochromatography with amperometric detection for analysis of explosive compounds. *ELECTROPHORESIS: An International Journal*, 21(7):1395–1404, 2000.

- [50] Stacy-Ann Barshick and Wayne H Griest. Trace analysis of explosives in seawater using solid-phase microextraction and gas chromatography/ion trap mass spectrometry. *Analytical Chemistry*, 70(14):3015–3020, 1998.
- [51] Carl A Groom, Sylvie Beaudet, Annamaria Halasz, Louise Paquet, and Jalal Hawari. Detection of the cyclic nitramine explosives hexahydro-1, 3, 5-trinitro-1, 3, 5-triazine (rdx) and octahydro-1, 3, 5, 7-tetranitro-1, 3, 5, 7-tetrazine (hmx) and their degradation products in soil environments. *Journal of Chromatography A*, 909(1):53–60, 2001.
- [52] Edward A Mason and Earl W McDaniel. Transport properties of ions in gases. *NASA STI/Recon Technical Report A*, 89, 1988.
- [53] MF Mesleh, JM Hunter, AA Shvartsburg, George C Schatz, and MF Jarrold. Structural information from ion mobility measurements: effects of the long-range potential. *The Journal of Physical Chemistry*, 100(40):16082–16086, 1996.
- [54] Zhigang Li and Hai Wang. Drag force, diffusion coefficient, and electric mobility of small particles. i. theory applicable to the free-molecule regime. *Physical Review E*, 68(6):061206, 2003.
- [55] Christian Bleiholder, Nicholas R Johnson, Stephanie Contreras, Thomas Wyttenbach, and Michael T Bowers. Molecular structures and ion mobility cross sections: Analysis of the effects of he and n2 buffer gas. *Analytical chemistry*, 87(14):7196–7203, 2015.
- [56] Ruwan T Kurulugama, Ed Darland, Frank Kuhlmann, George Stafford, and John Fjeldsted. Evaluation of drift gas selection in complex sample analyses using a high performance drift tube ion mobility-qt of mass spectrometer. *Analyst*, 140(20):6834–6844, 2015.
- [57] J Fernández de la Mora. Free-molecule mobility of polyhedra and other convex hard-bodies. *Journal of aerosol science*, 33(3):477–489, 2002.
- [58] Paul S Epstein. On the resistance experienced by spheres in their motion through gases. *Physical Review*, 23(6):710, 1924.
- [59] Hyungjun Kim, Hugh I Kim, Paul V Johnson, Luther W Beegle, JL Beauchamp, William A Goddard, and Isik Kanik. Experimental and theoretical investigation into the correlation between mass and ion mobility for choline and other ammonium cations in n2. *Analytical chemistry*, 80(6):1928–1936, 2008.
- [60] Hugh I Kim, Hyungjun Kim, Eric S Pang, Ernest K Ryu, Luther W Beegle, Joseph A Loo, William A Goddard, and Isik Kanik. Structural characterization of unsaturated phosphatidylcholines using traveling wave ion mobility spectrometry. *Analytical chemistry*, 81(20):8289–8297, 2009.
- [61] Juan Fernández-García and Juan Fernández de la Mora. Measuring the effect of ion-induced drift-gas polarization on the electrical mobilities of multiply-charged ionic liquid nanodrops in air. *Journal of the American Society for Mass Spectrometry*, 24(12):1872–1889, 2013.
- [62] Carlos Larriba and Juan Fernandez de la Mora. The gas phase structure of coulombically stretched polyethylene glycol ions. *The Journal of Physical Chemistry B*, 116(1):593–598, 2011.

- [63] Pedro Garcia-Ybarra and Daniel E Rosner. Thermophoretic properties of non-spherical particles and large molecules. *AIChE Journal*, 35(1):139–147, 1989.
- [64] Daniel W Mackowski. Monte carlo simulation of hydrodynamic drag and thermophoresis of fractal aggregates of spheres in the free-molecule flow regime. *Journal of aerosol science*, 37(3):242–259, 2006.
- [65] Carlos Larriba-Andaluz, Juan Fernández-García, Michael A Ewing, Christopher J Hogan, and David E Clemmer. Gas molecule scattering & ion mobility measurements for organic macro-ions in he versus n 2 environments. *Physical Chemistry Chemical Physics*, 17(22):15019–15029, 2015.
- [66] Jasper Boschmans, Sam Jacobs, Jonathan P Williams, Martin Palmer, Keith Richardson, Kevin Giles, Cris Laphorn, Wouter A Herrebout, Filip Lemièrè, and Frank Sobott. Combining density functional theory (dft) and collision cross-section (ccs) calculations to analyze the gas-phase behaviour of small molecules and their protonation site isomers. *Analyst*, 141(13):4044–4054, 2016.
- [67] Cris Laphorn, Trevor J Dines, Babur Z Chowdhry, George L Perkins, and Frank S Pullen. Can ion mobility mass spectrometry and density functional theory help elucidate protonation sites in ‘small’ molecules? *Rapid Communications in Mass Spectrometry*, 27(21):2399–2410, 2013.
- [68] Filipp Furche, Reinhart Ahlrichs, Patrick Weis, Christoph Jacob, Stefan Gilb, Thomas Bierweiler, and Manfred M Kappes. The structures of small gold cluster anions as determined by a combination of ion mobility measurements and density functional calculations. *The Journal of chemical physics*, 117(15):6982–6990, 2002.
- [69] Stefan Gilb, Patrick Weis, Filip Furche, Reinhart Ahlrichs, and Manfred M Kappes. Structures of small gold cluster cations (au n+, n<sub>i</sub> 14): Ion mobility measurements versus density functional calculations. *The Journal of chemical physics*, 116(10):4094–4101, 2002.
- [70] Kyoko Kojima, Minoru Sakairi, Yasuaki Takada, and Jun NAKAMURA. Vapor detection of tnt and rdx using atmospheric pressure chemical ionization mass spectrometry with counter-flow introduction (cfi). *Journal of the Mass Spectrometry Society of Japan*, 48(5):360–362, 2000.
- [71] Sehwan Park, Jihyeon Lee, Soo Gyeong Cho, Eun Mee Goh, Sungman Lee, Sung-Suk Koh, and Jeongkwon Kim. Mass spectrometric analysis of eight common chemical explosives using ion trap mass spectrometer. *Bulletin of the Korean Chemical Society*, 34(12):3659–3664, 2013.
- [72] Daniel Berthelot. Sur le mélange des gaz. *Compt. Rendus*, 126:1703–1706, 1898.
- [73] HA Lorentz. Ueber die anwendung des satzes vom virial in der kinetischen theorie der gase. *Annalen der physik*, 248(1):127–136, 1881.
- [74] Iain Campuzano, Matthew F Bush, Carol V Robinson, Claire Beaumont, Keith Richardson, Hyungjun Kim, and Hugh I Kim. Structural characterization of drug-like compounds by ion mobility mass spectrometry: comparison of theoretical and experimentally derived nitrogen collision cross sections. *Analytical chemistry*, 84(2):1026–1033, 2011.

- [75] G Reid Asbury and Herbert H Hill Jr. Separation of amino acids by ion mobility spectrometry. *Journal of Chromatography A*, 902(2):433–437, 2000.
- [76] Luther W Beegle, Isik Kanik, Laura Matz, and Herbert H Hill. Electrospray ionization high-resolution ion mobility spectrometry for the detection of organic compounds, 1. amino acids. *Analytical chemistry*, 73(13):3028–3034, 2001.
- [77] Claire J Bramwell, Michelle L Colgrave, Colin S Creaser, and Richard Dennis. Development and evaluation of a nano-electrospray ionisation source for atmospheric pressure ion mobility spectrometry. *Analyst*, 127(11):1467–1470, 2002.
- [78] Tom W Knapman, Joshua T Berryman, Iain Campuzano, Sarah A Harris, and Alison E Ashcroft. Considerations in experimental and theoretical collision cross-section measurements of small molecules using travelling wave ion mobility spectrometry-mass spectrometry. *International journal of mass spectrometry*, 298(1-3):17–23, 2010.